

Optimization of Novel Aluminum Welding Fillers Reinforced with NbB₂ Nanoparticles

By
Andrés Felipe Calle Hoyos

A thesis submitted in partial fulfillment of the requirements for the degree of

MASTER OF SCIENCE
IN
INDUSTRIAL ENGINEERING
UNIVERSITY OF PUERTO RICO
MAYAGÜEZ CAMPUS
2018

Approved by:

Oscar Marcelo Suárez, PhD.
President, Graduate Committee

Date

Wandaliz Torres Garcia, PhD.
Member, Graduate Committee

Date

Lourdes A. Medina, PhD.
Member, Graduate Committee

Date

Viviana I. Cesaní, PhD.
Member, Graduate Committee

Date

Viviana I. Cesaní, PhD.
Department Director

Date

Pedro Torres, PhD.
Representative of Graduate Studies

Date

ABSTRACT

Accordingly, the present research sought a cost-effective alternative to repair structures and rescue equipment with better quality welding, for rapid restoration of areas affected by disasters. This study focuses on the development of a new aluminum-based filler reinforced with a stable diboride nanodispersoid that provides the weld with higher service temperature and strength. A response surface methodology allowed assessing the effect of stir casting factors, namely the melt stirrer speed and the stirring time, while estimating a second-degree polynomial model, which enabled the optimization the manufacturing process of the filler with those niobium diboride (NbB_2) nanoparticles. The addition of NbB_2 nanoparticles upon stir casting of the filler alloy can raise its hardness 11% compared to the unreinforced filler. One important operational benefit is that no new TIG welding methods need to be developed, as the fillers are designed to be interchangeable with competing commercial ones.

RESUMEN

Por consiguiente, la presente investigación buscó una alternativa rentable para reparar estructuras y equipos de rescate con soldadura de mejor calidad, para la restauración rápida de áreas afectadas por desastres. Este estudio se centra en el desarrollo de un nuevo material de relleno a base de aluminio reforzado con un nanodispersoide de diboruro de niobio estable que ofrece la soldadura con una mayor temperatura de servicio y fuerza. La implementación de la técnica de fundición por agitación es un método relativamente simple y de bajo costo para la fabricación. Una metodología de superficie de respuesta permitió evaluar el efecto de los factores de fundición por agitación, concretamente la velocidad del agitador de fusión y el tiempo de agitación, mientras se estimaba un modelo de polinomio de segundo grado, lo que permitió la optimización el proceso de manufactura del material de relleno con nanopartículas de diboruro de niobio (NbB_2). La adición de nanopartículas de NbB_2 en fundición de agitación de la aleación de relleno puede aumentar su dureza en un 11% en comparación con el material de aporte no reforzada. Un beneficio operacional importante es que no es necesario desarrollar nuevos métodos de soldadura TIG, ya que los rellenos están diseñados para ser intercambiables con los materiales de aporte comerciales.

ACKNOWLEDGEMENTS

I blame my family and my friends because writing this thesis were several years of sustained suffering, but there is no more beautiful word to my ears to hear that they are proud of me.

I'm sincerely grateful to the University of Puerto Rico at Mayaguez, especially Industrial Engineering program to give me the opportunity to expand my knowledge and develop my personal skills.

I am particularly grateful to the Nanotechnology Center (National Science Foundation grant HRD 0833112 and 1345156) for providing funding my graduate studies and the development of this thesis.

At last, but the most Important I would like to thank Dr. O. M. Suarez's research group for prolonging my agonies with your encouragement and support throughout the project, and UPRM Nanotechnology Center technicians: Boris Renteria and Carlos Rivera UPRM Mechanical Engineering Laboratory.

Table of Contents

1. Introduction	1
1.1 Justification	1
1.2 Literature review.....	3
1.2.1 Aluminum Welding Optimization	3
1.2.2 Welding filler quality tests	5
1.2.3 Reinforcements of Aluminum Matrices in Composites	6
1.2.4 Casting Process for Fillers of Aluminum Alloys	8
1.3 Scope and Outline of the Research	9
1.4 Objective	10
1.4.1 General Objective	10
1.4.2 Specific Objectives	10
2. Theoretical Background	12
2.1 Welding	12
2.1.1 Aluminum Welding.....	12
2.1.2 Filler material	17
2.2 Composite Materials	18
2.2.1 Metal Matrix Composites (MMCs)	18
2.2.2 Metal Matrix Nanocomposites	19
2.3 Mechanical Alloying by Ball Milling.....	19
2.3.1 Type of Mill	19
2.3.2 Milling Container.....	21
2.3.3 Milling Energy and Speed.....	21
2.3.4 Milling Time	22
2.4 Casting.....	22
2.4.1 Stir Casting	24

2.5	Cold Rolling.....	25
3.	Exploratory Experiments of Aluminum Filler Treated with NbB ₂ Nanoparticles	27
3.1	Evaluating Welding for New Aluminum Filler	27
3.1.1	Methodology	28
3.1.2	Results and Discussion	36
3.1.3	Conclusions	42
3.2	Techniques to Improve Uniform Distribution of NbB ₂ Nanoparticles	43
3.2.1	Methodology	44
3.2.2	Results and Discussion	51
3.2.3	Conclusions	56
4.	Optimization of Stir Casting Process of Aluminum Filler Reinforced with NbB ₂ Nanoparticles	57
4.1	Full Factorial Experiment of Stir Casting Process	58
4.1.1	Methodology	59
4.1.2	Results and Discussion	63
4.1.3	Conclusions	73
4.2	Filler Optimization: Central Composite Experiment of Stir Casting	74
4.2.1	Methodology	75
4.2.2	Results and Discussions.....	85
4.2.3	Conclusions	116
5.	Comparative Analysis of NbB ₂ -Treated Filler to Commercial 5356 Filler	117
5.1	Full Factorial Experiment to Compare the Thermal Expansion Coefficient of Both Fillers Before Welding.....	118
5.1.1	Methodology	119
5.1.2	Results and Discussion	121
5.1.3	Conclusions	130
5.2	Comparison of the experimental and commercial fillers after welding.....	131

5.2.1	Methodology	132
5.2.2	Results and Discussions.....	134
	<i>Comparison of welding Brinell hardness on the weld surface</i>	134
	<i>Comparison of heat-affected zones</i>	138
5.2.3	Some prospective applications and markets	142
5.2.4	Conclusions	143
6.	General Conclusions and Recommendations	144
6.1	Future Work	146
7.	Reference	147
8.	Appendices	154
8.1	Appendix A.....	154
	A.1 The grinding settings and result for 10hr, 1600 RPM.....	154
	A.2 The cold welding settings and result for 1hr, 1020 RPM.....	155
8.2	Appendix B.....	155
	B.1 Full factorial design matrix	155
	B.2 Central composite design matrix for Brinell hardness.....	156
	B.3 The grinding settings and result for 20hr, 1600 RPM.....	157
	B.4 Central composite design matrix for Porosity.....	158
8.3	Appendix C.....	159
	C.1 Full factorial design matrix of thermal expansion coefficient.....	159
8.4	Appendix D.....	159

LIST OF FIGURES

Figure 1.1 Weld test assembly showing the location of tensile specimen. All dimensions are in millimeters[13].	5
Figure 1.2 Outline of the objectives of this work.	11
Figure 2.1 Schematic of TIG welding.	14
Figure 2.2 Tungsten inert gas (TIG) technique.	15
Figure 2.3 Schematic of planetary ball mill. Movement in a normal and counter direction.	20
Figure 2.4 Tungsten carbide vial set consisting of a vial, lid, gasket, and milling balls. (Courtesy of SPEX CertiPrep, Metuchen, NJ.).	21
Figure 2.5 Flowchart of the basic operations to produce a casting.	23
Figure 2.6 Schematic diagram of mechanical stir casting.	25
Figure 2.7 Cold rolling process diagram.	26
Figure 3.1 Schematic depicting the ball motion inside the planetary ball mill (Courtesy of Gilson Company, Worthington, OH.).	29
Figure 3.2 Visual representation of the preparation of the ball milling process.	29
Figure 3.3 XRD pattern of NbB ₂ : as-received (without ball milling, upper spectrum), and NbB ₂ particles after 10 hours of milling (lower spectrum).	30
Figure 3.4 Nanocomposite pellets inside the jars after cold welding.	31
Figure 3.5 Schematic of the NbB ₂ nanoparticles coated with aluminum as a result of the impacts.	31
Figure 3.6 Cold rolling process of the cylindrical ingots.	33

Figure 3.7 Lincoln Electric Precision TIG 225 230V AC / DC TIG.	34
Figure 3.8 Indentation on weld with NbB ₂ nanoparticles.	37
Figure 3.9 Hardness analysis of the Al-1wt% NbB ₂ filler.	38
Figure 3.10 Porosity of the weld with 99% Al - 1% NbB ₂ filler.	39
Figure 3.11 Percent porosity of preliminary welded samples.	39
Figure 3.12 6061 plates welded with Al-1wt% NbB ₂ filler.	40
Figure 3.13 Partial fusion (PF) of welded AA 6061 plates with Al-1wt% NbB ₂ filler.	40
Figure 3.14 Preliminary UTS measurements.	41
Figure 3.15 Agglomeration breakdown process to achieve uniform dispersion in the nanocomposite.	45
Figure 3.16 Schematic of the stir casting process.	46
Figure 3.17 Drawing of the crucible used during the experiment.	47
Figure 3.18 Stirrer schematic and 3D model.	47
Figure 3.19 Schematic of the stirrer inside the graphite crucible.	48
Figure 3.20 Groove weld test assembly dimensions.	49
Figure 3.21 Test specimen welded with filler reinforced with NbB ₂ nanoparticles.	50
Figure 3.22 Polished samples for Brinell hardness and porosity tests.	50
Figure 3.23 Hardness analysis of the Al-Mg 5% filler with NbB ₂	51
Figure 3.24 Individual Value Plot of Hardness analysis of the Al-Mg 5% filler with NbB ₂ (95% CI for the Mean).	52
Figure 3.25 Test for two variances: 1% NbB ₂ Weld, 2% NbB ₂ Weld, Ratio = 1 vs Ratio ≠ 1.	53
Figure 3.26 Porosity of the sample welded with Al-Mg-NbB ₂ 2% filler.	53

Figure 3.27 Percent porosity of welded samples.....	54
Figure 3.28 Optical micrographs of the weld: (A) Al-Mg 5%; (B) Al-Mg 5% NbB ₂ 1%; and (C) Al-Mg 5% NbB ₂ 2%.	55
Figure 4.1 Full factorial design for stir casting process.....	59
Figure 4.2 Schematic and 3D model of the tensile test specimen.	61
Figure 4.3 Diagram of the manufacturing process.	62
Figure 4.4 Normal probability plot of Ultimate tensile strength (95% CI).	63
Figure 4.5 Residuals versus the fitted value of Ultimate tensile strength.	64
Figure 4.6 Normal probability plot with Box Cox transformation of Ultimate tensile strength.	65
Figure 4.7 Deleted residuals versus fitted values with Box Cox transformation of the Ultimate tensile strength.....	65
Figure 4.8 Deleted residuals versus order plot with Box Cox transformation of Ultimate tensile strength.....	66
Figure 4.9 Pareto chart of the standardized effects of stir casting (response is the Ultimate tensile strength, $\alpha = 0.05$).....	67
Figure 4.10 Normal plot of the standardized effects of stir casting (the response is the Ultimate tensile strength, $\alpha = 0.05$).....	68
Figure 4.11 Interaction plot for Ultimate tensile strength (fitted means).	69
Figure 4.12 Two-dimensional contour plot of the surface of Ultimate tensile strength. .	70
Figure 4.13 Response surface of the Ultimate tensile strength.	71
Figure 4.14 Central composite design for the stir casting components.	75
Figure 4.15 Area to be filled with the welded filler material.	79

Figure 4.16 Photos of mold with three cast ingots.....	80
Figure 4.17 Mold schematic and 3D model.	80
Figure 4.18 Pouring basin schematic and 3D model.	81
Figure 4.19 XRD pattern of NbB ₂ : as-received (without ball milling, upper spectrum), and NbB ₂ particles after 20 hours of milling (lower spectrum).	83
Figure 4.20 Steps to perform the quality test.....	84
Figure 4.21 Box-Cox of normal probability plot of the Brinell hardness (MPa), (95% CI).	85
Figure 4.22 Box-Cox of deleted residuals versus fitted values of the Brinell hardness (MPa).	86
Figure 4.23 Box Cox of deleted residuals versus order plot of the Brinell hardness (MPa).	87
Figure 4.24 Main effects plot of the Brinell hardness.	88
Figure 4.25 Individual value plot of the Brinell hardness as a function of the NbB ₂ percent using lineal regression.....	89
Figure 4.26 Individual value plot of the Brinell hardness as a function of the stirring speed with lineal regression.....	89
Figure 4.27 Individual value plot of the Brinell hardness as a function of the stirring time using lineal regression.....	90
Figure 4.28 Contour plot of the Brinell hardness as a function of the stirring speed and NbB ₂ percent.	92
Figure 4.29 Response surface of the Brinell hardness as a function of the stirring speed and NbB ₂ percent.	93

Figure 4.30 Contour plot of the Brinell hardness as a function of the stirring time and NbB ₂ percent.	94
Figure 4.31 Response surface of the Brinell hardness as a function of the stirring time and NbB ₂ percent.	95
Figure 4.32 Contour plot of the Brinell hardness as a function of the stirring time and stirring speed.....	96
Figure 4.33 Response surface of the Brinell hardness as a function of the stirring time and Stirring speed.	97
Figure 4.31 Normal probability plot of porosity (%), (95% CI).	99
Figure 4.32 Normal probability plot with Box Cox transformation of porosity (95% CI).	100
Figure 4.33 Deleted residuals versus as a function of the transformed values of porosity.	101
Figure 4.34 Deleted residuals versus order plot of porosity measurements.....	101
Figure 4.35 Main effects plot for porosity (%).	103
Figure 4.36 Individual value plot of Porosity as a function of the NbB ₂ percent using a lineal regression.	104
Figure 4.37 Individual value plot of porosity as a function of the stirring speed using a lineal regression.	104
Figure 4.38 Individual value plot of porosity as a function of the stirring time using lineal regression.	105
Figure 4.39 Interaction plot for porosity.	105
Figure 4.40 Contour plot of porosity as a function of the stirring speed and NbB ₂	108

Figure 4.41 Response surface of porosity as a function of the stirring speed and NbB ₂ .	109
Figure 4.42 Contour plot of the porosity as a function of the stirring time and NbB ₂ .	110
Figure 4.43	111
Figure 4.44 Contour plot of the porosity as a function of the stirring time and stirring speed.	112
Figure 4.45 Response surface of the porosity as a function of the stirring time and the stirring speed.	113
Figure 5.1 2 ² full factorial design for the novel filler NbB ₂ and the commercial filler 5356.	119
Figure 5.2 Schematic of the thermomechanical analysis unit.	120
Figure 5.3 Probability plot of thermal expansion coefficient (95% CI).	121
Figure 5.4 Normal probability plot with Box Cox transformation of the thermal expansion coefficient (95% CI).	122
Figure 5.5 Deleted residuals versus the fitted value of thermal expansion coefficient.	123
Figure 5.6 Residuals versus order plot of thermal expansion coefficient.	123
Figure 5.7 Pareto chart of the standardized effects of thermal expansion coefficient ($\alpha = 0.05$).	125
Figure 5.8 Normal plot of the standardized effects of thermal expansion coefficient ($\alpha = 0.05$).	125
Figure 5.9 Interaction plot for thermal expansion coefficient (fitted means).	126
Figure 5.10 Cube Plot for thermal expansion coefficient (°C ⁻¹) fitted means.	128

Figure 5.11 Individual value plot for thermal expansion coefficient ($^{\circ}\text{C}^{-1}$) as a function of the temperature with lineal regression.....	128
Figure 5.12 Individual value plot for thermal expansion coefficient ($^{\circ}\text{C}^{-1}$) as a function of the fillers.....	129
Figure 5.13 Schematic of microhardness indentations of heat-affected zone.	134
Figure 5.14 Dot plot of the hardness for experimental filler, 5356 filler and 6061 base material.	135
Figure 5.15 Boxplot of the Brinell values for NbB_2 filler, 5356 filler, and 6061 base material.	136
Figure 5.16 Individual value plot measured on the 2% NbB_2 filler and 5356 filler	136
Figure 5.17 Test for two variances: 2% NbB_2 Weld, 5356 Weld, Ratio = 1 vs Ratio \neq 1.	137
Figure 5.18 Boxplots of average HV0.2 hardness on the upper line of the weld with the experimental filler. Base metal (BM), heat affected zone (HAZ) and weld metal (WM).	139
Figure 5. 19 Boxplots of average HV0.2 hardness on the lower line of the weld with the experimental filler. Base metal (BM), heat affected zone (HAZ) and weld metal (WM).	139
Figure 5.20 Boxplots of average HV0.2 hardness on the top line of the 5356 filler, Base Metal (BM), Heat Affected Zone (HAZ) and Weld Metal (WM).....	141
Figure 5.21 Boxplots of average HV0.2 hardness on the bottom line of the 5356 filler, Base Metal (BM), Heat Affected Zone (HAZ) and Weld Metal (WM).....	141

LIST OF TABLES

Table 3.1 Chemical composition of base material and fillers material (wt.%).	33
Table 3.2 Working range of the welding process.	34
Table 3.3 Constant Lincoln Electric Precision 225 AC/DC TIG machine parameters.	35
Table 4.1 2 ² full factorial parameter for stir casting process.	59
Table 4.2 Analysis of variance for the transformed response Ultimate tensile strength	67
Table 4.3 Model Summary for Transformed Response Ultimate tensile strength.	69
Table 4.4 Coded Coefficients for Transformed Response Ultimate tensile strength.	70
Table 4.5 Parameters to calculate the optimal of Ultimate tensile strength (MPa).	72
Table 4.6 Optimal Response Prediction of Ultimate tensile strength.	72
Table 4.7 Central Composite parameter for the stir casting components.	76
Table 4.8 Stir Casting process diagram.	76
Table 4.9 Analysis of Variance for Transformed Response.	87
Table 4.10 Model Summary for Transformed Response Brinell hardness.	90
Table 4.11 Coded Coefficients for Transformed Response Brinell hardness.	91
Table 4.12 Parameters to calculate the optimal Brinell Hardness.	98
Table 4.13 Optimal Response Prediction of Brinell Hardness.	98
Table 4.14 Analysis of variance for transformed response porosity area.	102
Table 4.15 Model summary for transformed response of porosity.	106
Table 4.16 Coded coefficients for transformed response porosity.	106
Table 4.17 Parameters to calculate the optimal of porosity (%).	114
Table 4.18 Optimal response prediction of porosity (%).	114

Table 4.19 Parameters to calculate the optimal of Brinell hardness (MPa) and Porosity (%).....	114
Table 4.20 Optimal Response Prediction of Brinell hardness (MPa) and Porosity (%).	115
Table 5.1 Full factorial Parameter for the novel filler NbB ₂ and the commercial filler 5356.	120
Table 5.2 Analysis of Variance for Thermal expansion coefficient.	124
Table 5.3 Model Summary for Thermal expansion coefficient.....	127
Table 5.4 Coded Coefficients for Thermal expansion coefficient.	127
Table 5.5 Chemical composition of NbB ₂ filler, 5356 filler and 6061-base material (wt.%).	132
Table 5.6 Descriptive statistics of Brinell hardness on the fillers and th base alloy	135
Table 5.7 Mann-Whitney Test and CI: 2% NbB ₂ Welded, 5356 Welded	138

LIST OF EQUATION

Brinell Hardness eq. 01

Regression Equation of Ultimate tensile strength stress eq. 02

Regression Equation of Brinell Hardness eq. 03

Regression Equation of Porosity Area (%) eq. 04

ACRONYMS USED IN THE RESEARCH

Some terms have been coined to explain process in the present research. The following list explains the expansions of some of the most commonly used acronyms:

Aluminum Matrix Composites	AMCs
American Welding Society	AWS
Analysis of Variance	ANOVA
Ball to Power Ratio	BPR
Brinell Hardness	BH
Composite Central Design	CCD
Confidence Interval	CI
Flux-cored arc welding	FCAW
Friction-stir welding	FSW
Gas metal arc welding	GMAW
Gas tungsten arc welding	GTAW
Heat-Affected Zone	HAZ
Mechanical Alloying	MA
Metal Inert Gas	MIG
Metal Matrix Composites	MMC
Mechanical Milling	MM
Metal Matrix Composites	MMCs
Partial Fusion	PF
Revolutions per Minute	RPM

Standard Error	SE
Thermal Expansion Coefficient	CTE
Thermomechanical Analysis	TMA
Tungsten Inert Gas	TIG
Ultimate Tensile Strength	UTS
Variance Inflation Factor	VIF
Welding Procedure Specifications	WPS
X-ray Diffraction	XRD

I. CHAPTER

1. Introduction

1.1 Justification

Globalization has steered the petroleum, marine, aerospace, and automotive industries to face new challenges in a rapidly changing market where consumers are constantly demanding better filler materials for aluminum welding. As a lightweight material, aluminum has a high corrosion resistance, excellent strength, and high ductility [1]. A brief literature review reveals that aluminum welding can be attained via several techniques. In particular, tungsten inert gas (TIG) welding has been commonly employed in high quality welds [2]–[4]. During the TIG welding process, an electric arc between the piece and a tungsten electrode provides the necessary thermal energy for the base metal and filler. Advantages such as small deformations due to heat concentration, uniformity, and purity (due to the inert gas cover) ensure melting effectiveness of the joining materials [2], [4]. Therefore, TIG welding is the preferred technique for which one needs to develop a filler that meets the quality requirements and demands of the industry.

The quality of a weld is based on the absolute compatibility of the materials joined. Metallographic analyses are standard techniques to evaluate weld quality. Metallography helps reveal the resulting porosity, and weld uniformity [2]–[5]. In addition, tensile experiments, as quality tests, are commonly carried out to prove the effectiveness of the weld [6]. In that respect, experimental design and statistical modeling are pertinent tools

implemented in the research of welding processes [7]. For instance, the Taguchi method is a systematic means for the optimization of the TIG welding process with respect to mechanical properties and quality of the weld [8].

In 2014, niobium diboride (NbB_2) nanoparticles were used to strengthen a pure aluminum matrix upon wire fabrication [9]. The incorporation of such hard particles to metals, as reinforcement, has shown improvement in strength, oxidation resistance, operating temperature, stiffness, and wear resistance, as well as in controlling the coefficient of thermal expansion [4], [10], [11]. In effect, there is an increasing need of lighter, yet stronger materials applicable to new technologies. Therefore, industries such as the aerospace and automotive ones, have turned the focus of their research to nanoparticle-reinforced aluminum and aluminum alloys. The good strength-to-weight ratio makes those composite materials apt for structural applications [1], [5], [12]. Of particular interest for the present research has been a 2013 work by Fattahi, where he was able to increase the strength and hardness of a filler for aluminum welding by adding carbon nanotubes using cold pressing. A year later, similar results were obtained using graphene nanosheets [13], [14].

Accordingly, the present research sought a cost-effective alternative to repair structures and rescue equipment with better quality welding, for aerospace applications and rapid restoration of areas affected by disasters. Good weld quality is achieved by improving the mechanical properties of aluminum welding by adding NbB_2 nanoparticles to an aluminum filler, thereby improving the manufacturing process through: (1) pellet homogenization, to

ensure appropriate nanoparticle dispersion; (2) stir casting, to improve the distribution of the reinforcement NbB₂ during melting and casting; and (3) cold rolling, to obtain a filler in the proper form. A design experiment was used to identify significant factors and parameters in the stir casting process. To establish how adequate this new filler is for welding applications, we employed several characterization techniques. As a comparison baseline, we selected a commercial AA 5356 aluminum alloy filler, which is commonly used for having high temperature service characteristics.

1.2 Literature review

1.2.1 Aluminum Welding Optimization

After World War I, the academia and industry developed different methods for producing better quality aluminum welds. Since the demand grew exponentially, aluminum welding was adapted to become an industrial art. Some of the most used methods for welding are: gas tungsten arc welding (GTAW), gas metal arc welding (GMAW), flux-cored arc welding (FCAW), and friction-stir welding (FSW). The high thermal conductivity, high reactivity, and high coefficient of expansion of aluminum makes welding of aluminum alloys difficult [15]. Studying the more relevant parameters to the aluminum welding process has been, therefore, paramount to determine the best conditions for higher quality welding.

In 2012, Al-Jarrah studied the appearance and mechanical properties of friction stir welded plates with different parameters, including rotational speed and welding speed. The study concluded that “at low rotation speed of 560 rpm with higher welding speed of 2 mm/s, the flow of plasticized metal under shoulder face was not sufficient, leading to a pitting welded surface” [16]. Also, a two-level fractional factorial design helped model the TIG welding process. These works led to produce a mathematical model that can help to better define parameters for predicting the weld bead geometric descriptors and to use a genetic algorithm for the optimization of the process parameters [17].

Kumar presented works intended to optimize the parameters of TIG welding process to enhance the mechanical properties of welded parts via the Taguchi method. This method allowed analyzing the experimental parameters, both individually and independently. The welding method parameters used were peak current, base current, welding speed, and frequency. Two levels were evaluated for each parameter. The response variables were ultimate tensile strength (UTS), yield strength, percent elongation, and toughness. The Taguchi method defined the optimal parameters: peak current at level 2 (80 A), base current at level 1 (40 A), welding speed at level 2 (230 mm/min), and frequency at level 2 (4 Hz) [8]. Furthermore, Kumar measured five parameters of TIG through the Taguchi method using an orthogonal matrix L25 with four levels and four factors to study their effect on the quality of the weld. The analysis of variance (ANOVA) determined that the pulse current had a significant effect on the quality characteristics of multiple mechanical properties and the weld microstructure [18].

1.2.2 Welding filler quality tests

In 2014, Fattahi studied the effect of adding different nanosheet amounts to a 4043-aluminum matrix by mechanical alloying to produce filler wires for aluminum welding. The filler material was characterized using microhardness and tensile tests. To measure the properties of the filler, the author used a fitting following the American Welding Society (AWS) standards: A5.01M / A5.01: 2013 and A5.10 / A5.10M: 2012 (Figure 1.1) [13]. The same author also analyzed a reinforcing matrix aluminum filler material with nanotubes via similar characterization techniques for the filler [14]. These studies corroborated that, by reinforcing the filler with nanoparticles, the strength and microhardness of the material increased.

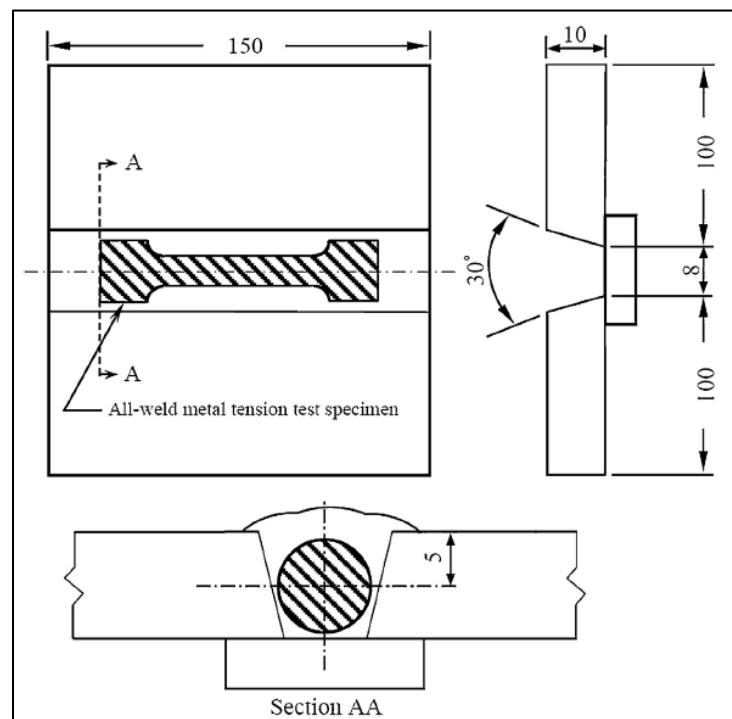


Figure 1.1 Weld test assembly showing the location of tensile specimen. All dimensions are in millimeters[13].

In another study seeking a better-quality measure of welding aluminum and to define the best parameters for welding, Bai used an orthogonal experimental design to evaluate the influence of plasma metal inert gas (MIG) welding parameters on the weld porosity, a good indicator of weld quality [19]. Microstructure analysis and tensile tests allowed establishing the best TIG welding parameters to improve the mechanical properties of a welded 5456 aluminum alloy [8]. These studies used porosity and hardness tests to assess the quality of the filler material. Therefore for the present research, we consider that these tests are very pertinent to assess the quality of a given filler material.

1.2.3 Reinforcements of Aluminum Matrices in Composites

Some aluminum alloys bear the best combination of mechanical properties, wear resistance, and low density that make them ideal for a wide variety of applications. Numerous studies have sought to reinforce light alloys with various hard materials, such as aluminum oxide (Al_2O_3) and graphite particles, to raise the tensile strength and hardness [1]. Even fly ash cenospheres, one of the residues generated by coal combustion, have been used as reinforcements. In this particular case, the ultimate composite tensile strength had an 8.5% increase for 1% of fly ash cenospheres [20].

Aluminum nitride particles (AlN_p) are in the list of materials used for reinforcing the aluminum matrix. New casting methods sought to improve the integration of the compounds with a bottom pouring arrangement under a controlled argon atmosphere. The higher the AlN_p percentage in the matrix, the higher the resulting hardness, at the

expense of the formability of the composite [5]. Those previous examples provide evidence that the addition of different reinforcements to the aluminum matrix can strengthen it in a controlled manner.

In another work, on the fabrication of aluminum 6061-T6 alloy matrix composites reinforced with different weight percentages of boron carbide B_4C particles, a modified stir casting route allowed for improved hardness and tensile strength [19]. In some studies, different casting methods were tested to avoid agglomeration and segregation of Al_2O_3 nanoparticles in an aluminum matrix. As a result, increasing the particles' weight fraction and decreasing the particles' size improved the hardness of the composites [21].

Tahamtan studied a combination of ball milling and stir casting processes to produce master metal matrix composites (MMC). Ball milling of Al / Mg alumina powders favored the contact between the ceramic and the matrix. Reducing the size of particles to the nanoscale improved the tensile strength of the composite. Lowering the stirring speed from 1200 rpm to 400 rpm reduced the amount of pores of the MMC. [22]. Based on the analysis of the research results reported above, it is apparent that there is a need to improve the mechanical properties of aluminum by adapting and enhancing different casting techniques to improve the nanoparticles distribution in the aluminum matrix.

1.2.4 Casting Process for Fillers of Aluminum Alloys

Different casting processes were developed to fabricate filler materials for welding aluminum. These sought to improve different features, such as the wetting of reinforcement particles by the liquid matrix (upon processing), the particle's homogeneous distribution, and smaller porosity to obtain a high-quality filler. The most significant filler material parameters for improving the manufacturing process are melt temperature, feeding rate of the particles, inoculation time, and the stirring speed of the melt [5]. Synthesis and characterization of different cast aluminum composites and stirring methods have been carried out to optimize those processing techniques. For instance, compo-casting is one of the simplest alternatives to produce aluminum matrix composites (AMCs) [23], [24]. The goal is to add fine particles into a molten metal to ensure effective inclusion of the reinforcements in the alloy matrix with a more uniform distribution. Raja [23] defined the most important parameters for the stir casting process to strengthen the aluminum matrix containing fly ash (FA) and silicon carbide (SiC), which are: spindle speed, stirring time, stirring temperature, preheating temperature of reinforcements (SiC and FA), preheating time and preheating temperature of the mold, and powder feed rate. The resulting composite possessed a fine and homogeneous particle dispersion. Further, S. Sankaranarayanan studied the nanoparticles' addition to a magnesium-titanium matrix by a stir casting process, to improve the microstructure and mechanical characteristics of this MMC. The parameters were spindle speed, stirring time, and stirring temperature; a spindle rod, and a twin blade mild steel impeller helped create the vortex to obtain a homogeneous melt [25].

Taking into consideration the state-of-the-art of this technology, most of the present research hinged on finding new compounds that renovate the aluminum welding industry. In effect, the methods described thus far do not clearly identify the factors that can help develop an optimal casting process. Being able to know these factors would allow manufacturing higher quality fillers. The proposed novel methodology incorporates NbB₂ in the manufacturing of nanocomposite fillers for aluminum welding. To be truly innovative, knowing each step of the casting process is paramount. During the present study, different techniques were tested to produce a good interface between matrix and reinforcement and to attain a homogeneous distribution of the nanocomposite in the filler. Clearly, the methods developed in the literature provide us with some guidance and potential solutions to achieve these goals.

1.3 Scope and Outline of the Research

The scope of the thesis encompasses the use of different optimization strategies to analyze the factors in the manufacturing process of filler materials for TIG welding aluminum, and a statistical design of experiments to study the effect of casting factors such as stirrer speed and stirring time of the melt with nanoparticles NbB₂. In addition, several optimization criteria were used to evaluate performance measures of the various materials. Different characterization techniques were used to determine the weld porosity, the material hardness, and its ultimate tensile strength. These are essential characteristics to meet physical and mechanical specifications of the welds.

1.4 Objective

1.4.1 General Objective

The general objective of the present thesis has been to optimize a novel aluminum welding filler reinforced with NbB₂ nanoparticles for TIG aluminum welding.

1.4.2 Specific Objectives

A general outline of the objectives of this work are shown in Figure 1.2. The research work focuses on the following specific objectives:

- A. To study the behavior of aluminum wire with NbB₂ nanoparticles intended for welding applications.
- B. To define a response surface method and to estimate a second-degree polynomial model, which enabled the optimization of stir casting process.
- C. To perform a comparative analysis of Al-5% Mg filler reinforced with NbB₂ nanoparticles, and a commercial Al 5356 alloy filler.

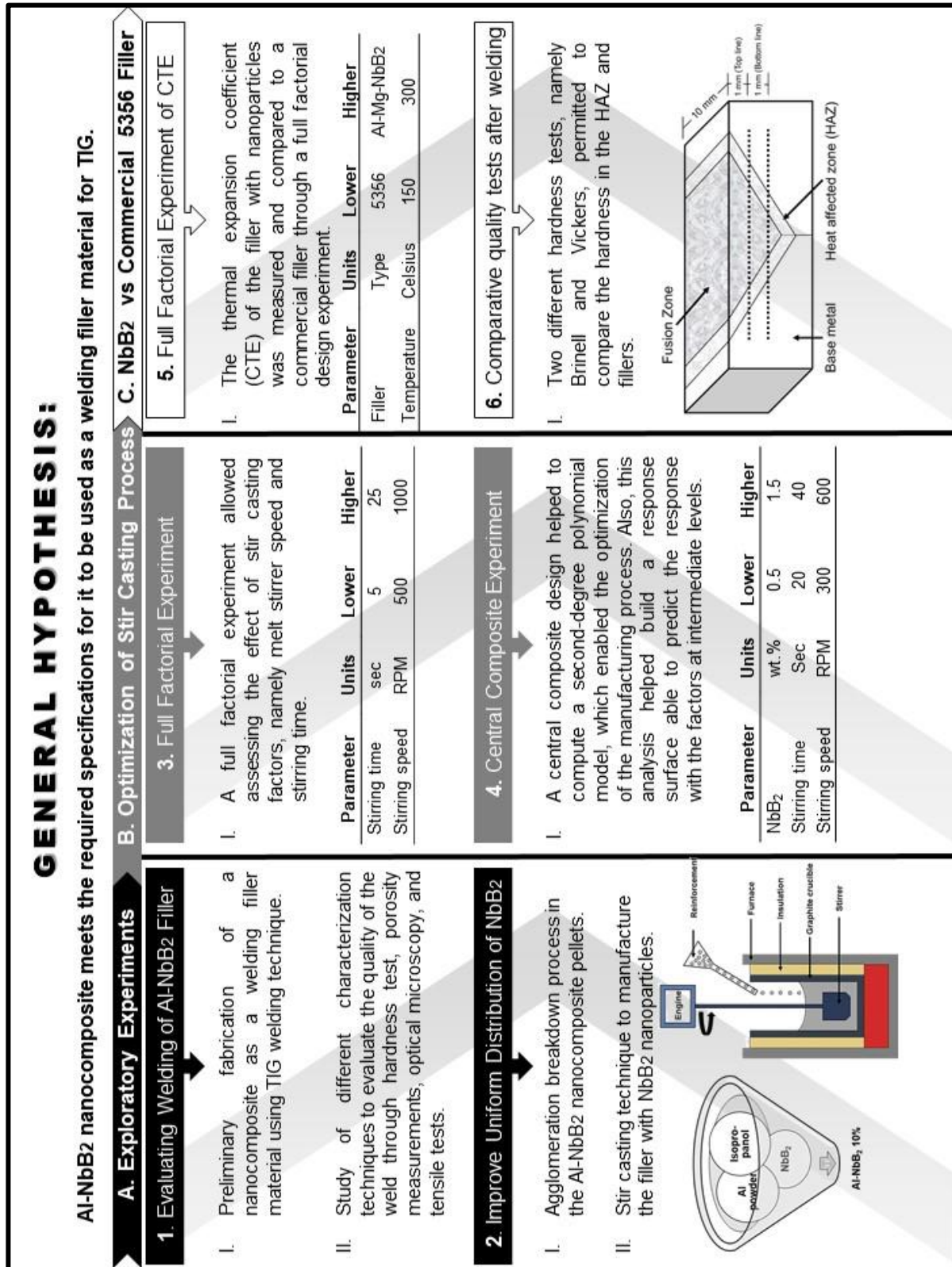


Figure 1.2 Outline of the objectives of this work.

II. CHAPTER

2. Theoretical Background

Process optimization and characterization in Materials Engineering are tasks that demand the conjunction of time and knowledge: A well-structured and scheduled experimental plan leads us to offset potential weaknesses and to effectively answer the research questions. The following topics are part of the theoretical framework that helps us to develop this research.

2.1 Welding

The welding process is critical to the manufacturing of most product parts. Sometimes, however, this process increases the product cost and can thwart the production line. Therefore, the most important functionality of welding is to form primary joints in metals or metal joints. Another function is to form more solid joints by means of interdiffusion between the materials [26]. Welding is crucial for solving problems in different types of disciplines, such as: mechanics, materials science, physics, chemistry and electronics. Since the point of highest stress in an assembled part is located at the union (weld), this union is responsible for the occurrence of a large percentage of weld failures during field work. Consequently, better welding processes must be developed to create newer and higher quality products that can benefit manufacturing companies [26].

2.1.1 Aluminum Welding

As aforementioned, aluminum welding is an essential tool in the manufacture of products requiring materials that combine strength and light weight. For example, the use of aluminum in aircraft manufacturing is limited by the lack of better joint strength. Similarly, in the automotive industry aluminum is used in many applications for the fabrication of parts, but it is not economical enough to replace the use of steel in automobile frames. For this reason, to improve the process of aluminum welding is critical. This should consider properties such as: the oxidation of aluminum; the solubility of hydrogen in molten aluminum, its thermal, electrical and magnetic characteristics; the lack of color change when heated; and its wide range of mechanical properties and melt temperatures when alloyed with other metals.

Welding of aluminum and its alloys can be achieved through more different welding methods than any other materials. Some of these are:

- 1) Gas metal arc welding (GMAW), also known as metal inert gas (MIG) welding, consists of forming an electric arc between a consumable wire electrode and the workpiece, the heat produced in the arc melts and joins the parts and consumable wire.
- 2) Friction welding (FRW) uses the mechanical friction between two solid parts and the lateral force called "upset" to melt the metals.
- 3) Laser beam welding (LBW) employs a laser that provides a concentrated heat source, allowing multiple join metal parts. The advantages provided by this technique are narrow welds and high welding rates.

- 4) Gas tungsten arc welding (GTAW) enables stronger, higher quality welds. This method is also known as tungsten inert gas (TIG) and is performed using an electric arc between a tungsten electrode (non-consumable) and planar-shaped electrode, i.e. the workpiece.

In this latter case, pure tungsten electrodes are less expensive and possibly more environmentally friendly. To protect the aluminum oxide welding area from atmospheric oxidation, an inert gas (argon or helium) is used, and the union is reinforced with a filler metal [27]. An example of the equipment and components for TIG are shown in Figure 2.1.

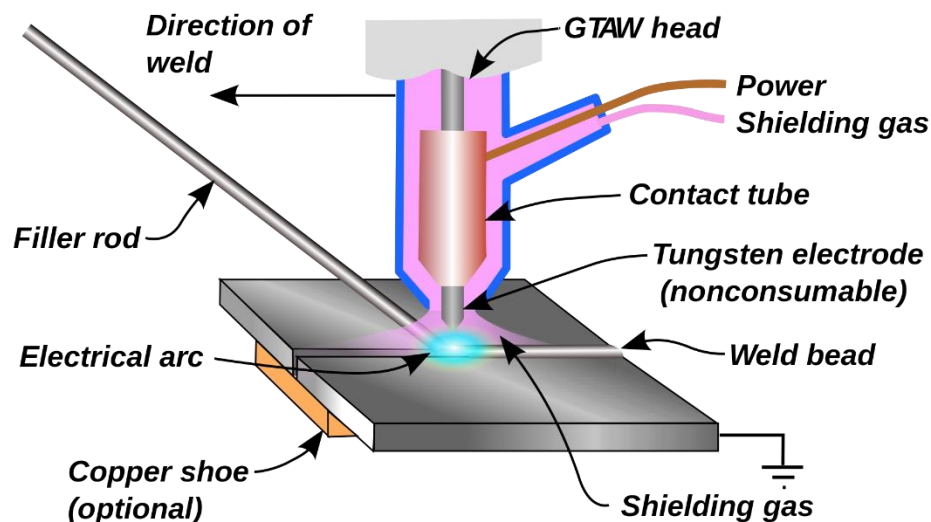


Figure 2.1 Schematic of TIG welding.

TIG welding requires a filler material to complete the welding. Figure 2.2 demonstrates how both hands of the operator work: one holds the gun while the other, the filler material. This is a limitation, because the welder's hands can hinder the viewing angle in the work

area, generating a lot of variability in the technique. On the other hand, it allows the welder to have greater control of the heat exposure and the amount of filler to be added to the weld.

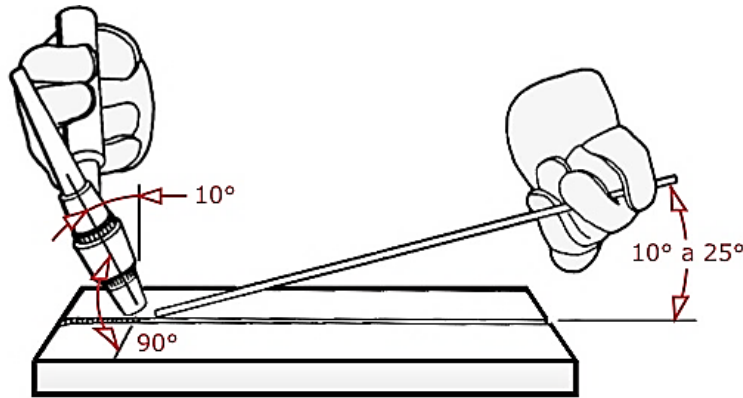


Figure 2.2 Tungsten inert gas (TIG) technique.

To overcome these challenges, the American Welding Society recommends these basic rules:

1. Preparation of base metal: The operator must clean the base material and remove the oxide or contamination of any type. Aluminum oxide on the material surface prevents good penetration in the base material because this oxide melts at 2,037 °C while aluminum can melt below 660 °C. Thus, to remove aluminum oxides, a stainless-steel bristle brush or an etching solution, such as acetone, should be used. When a stainless-steel brush is used, brushing must be done in one direction only.
2. Preheating: To prevent cracks in the welding, the aluminum piece must be preheated. It is recommended not to exceed the preheating temperature of 110 °C to prevent overheating.

3. Travel speed: Since aluminum has a high thermal conductivity, the speed must remain constant to obtain a homogeneous weld travel. We also have to keep in mind that increasing the heat requires faster movements to obtain the same thickness and height of the weld. Therefore, the size of the weld decreases if one increases the travel speed [27].
4. Shielding gas: The most efficient way to reduce the formation of aluminum oxide is to use a pure argon shield, which allows for good cleaning action and penetration of the working area.
5. Filler material: Since aluminum coefficient of thermal expansion is high, the filling material is required to compensate for shrinking upon cooling. To attain that goal, the selected filler material must have a temperature similar to the fusion temperature of the material base. The importance of the chemical composition, thickness, and different applications of filler materials will be discussed later.
6. Power source selection: The aluminum GTAW unit must provide constant voltage (CV) and constant current (CC). These machines usually perform a pulse transfer with an inverter power supply. Alternating current (AC) is commonly used to weld aluminum. This is because the arc flows from the workpiece to the positive electrode, removing the surface oxide.

2.1.2 Filler material

As mentioned, the filler material in the welding process allows joining two metallic pieces. Generally, filler metal selection takes into consideration that the base material has similar strength, toughness, and corrosion resistance. However, there is no need to select a filler metal having the same composition as the base metal. Aluminum has a variety of filler alloys, which possess equal or higher strength than the base material. The filler selection depends on the operating conditions of the welded component and the consideration of factors that may affect the welding operation [27].

2.1.4 Filler Alloy Selection Criteria

As mentioned, the optimum selection of the filler material depends on each job's specifications. Although many alloys can be joined by any type of filler material, only the specified combination can give the desired strength and other properties required by the workpiece [27]. Therefore, when selecting a welding filler alloy, the primary factors commonly considered are:

1. Ease of welding or lack of potential for cracking
2. Tensile or shear strength of the weld
3. Weld ductility
4. Service temperature
5. Corrosion resistance
6. Color match between the weld and base alloy after anodizing

2.2 Composite Materials

The combination of two or more materials, known as composites, has the objective of improving some desired properties. In a composite, the dispersed phase(s) is distributed in a continuous phase, i.e. the matrix [28].

2.2.1 Metal Matrix Composites (MMCs)

The MMCs most important features are: (1) the competitive prices and the variety of available reinforcement types; (2) reproducible processes, easy to carry out during manufacturing, while retaining the microstructure and properties; and (3) regular metalworking standard methods for manufacturing these MMCs [29]. The most common processing techniques for MMCs are powder metallurgy, spray deposition, mechanical alloying, and various casting technique [29]. The following are three types of MMCs based on the dispersed phase:

1. Particulate MMCs
2. Short fiber-reinforced MMCs
3. Continuous fiber-reinforced MMCs

Between the three types, the particulate MMCs and short-fiber-reinforced MMCs are the most used in industry because they are easier and less costly to manufacture and have isotropic properties compared to continuous fiber-reinforced MMCs. The particulate MMCs possess low density, high hardness, adequate toughness, high stiffness, and the availability of low-cost powders of suitable size [29].

2.2.2 Metal Matrix Nanocomposites

One advantage of MMCs is that one can control the size and volume of the reinforcement. When these particles are in the nanoscale and dispersed uniformly in the metal matrix, better isotropic mechanical properties are normally obtained. Another advantages of these reinforcements is that these MMCs are ease to manufacture and have low fabrication cost [30].

2.3 Mechanical Alloying by Ball Milling

Ball milling is commonly employed for mechanical alloying. The process of mechanical alloying (MA), through a high-energy ball mill, consists of mixing a desired ratio of two or more powder materials within the mill medium and the grinding balls [31]. The MA process is affected by several important variables that influence the desired product. These variables are discussed in the ensuing section.

2.3.1 Type of Mill

Shaker spex mills, attritor mills, and planetary ball mills are different types of mills for powder processing. The planetary ball mill is the method used in this research and will be described in a following section.

Planetary Ball Mills:

The planetary ball mill is the most popular type of grinding device for conducting MA experiments. The one used in the present research was manufactured by Fritsch, Germany. It offers different sizes of jars for grinding a few grams to hundreds of grams at the same time. These jars are arranged in a main rotating disk support and a mechanism that spins around its own axis. The centrifugal force produced makes the vials rotate around their own axes and the force produced by the main disk acting on the contents of the jars, which contain the material to be milled and the grinding balls, pulverizes the particles [31]. The vials rotate in the opposite direction to the main disk, as shown in Figure 2.3.

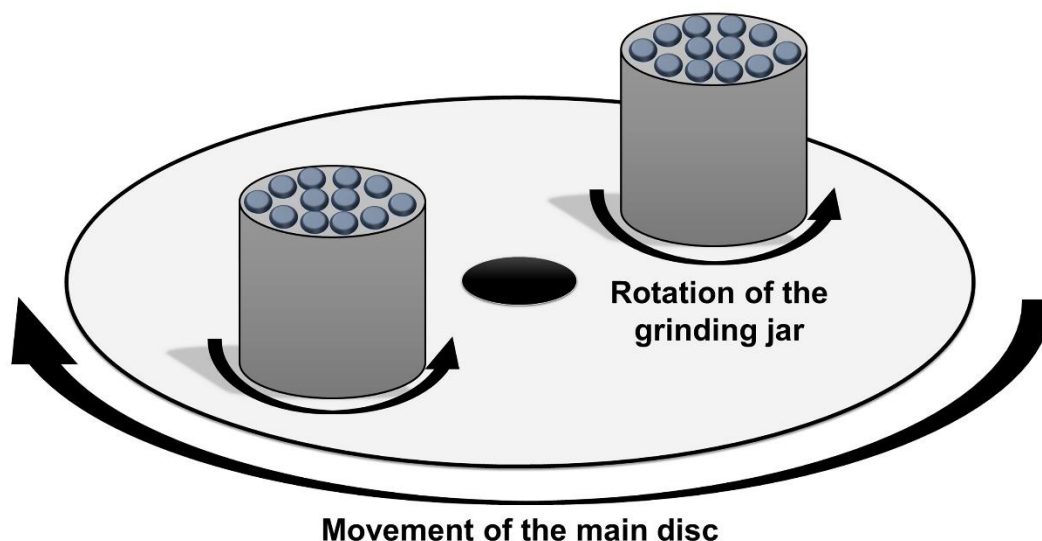


Figure 2.3 Schematic of planetary ball mill. Movement in a normal and counter direction.

2.3.2 Milling Container

These jars are usually made of different materials like agate, silicon nitride, sintered corundum, zirconium oxide, stainless steel, tempered steel, and tungsten carbide. For this research, and due to the characteristics of the reinforcing material (NbB_2), tungsten carbide jars and grinding balls were used, since these jars have greater resistance to abrasion and oxidation [31]. Figure 2.4 shows the grinding medium and jar employed in the present research.



Figure 2.4 Tungsten carbide vial set consisting of a vial, lid, gasket, and milling balls.

(Courtesy of SPEX CertiPrep, Metuchen, NJ.).

2.3.3 Milling Energy and Speed

The grinding speed defines the energy that will be imparted to the powder. If the kinetic energy is not enough, the material will not be milled, but if the speed is too high, the resulting kinetic energy will induce a temperature increase inside the jars, causing

contamination of the material. It is, therefore, very important to understand that the speed should be adequate to achieve good, uncontaminated grinding [31].

2.3.4 Milling Time

Milling time is a factor that depends on the speed of milling. In general, times are short for high speeds and longer for lower speeds. The milling time also depends on other factors, such as the intensity of grinding, the manufacturer's specifications, and grinding temperature. All these factors should have a balance to achieve efficient fracture or cold welding of two materials [31].

2.4 Casting

Normally, the casting processes are divided into two categories: fungible molding processes (mold in green and dry sand) and casting processes in a continuous production line with extended life molds (permanent mold made of metal). Figure 2.5 shows a flowchart of the basic operations to produce a casting. Cast alloys are also divided into two groups: alloys that are less viscous, which are suitable for casting by gravity, and the second group, with higher viscosity, requiring the use of die casting [32].

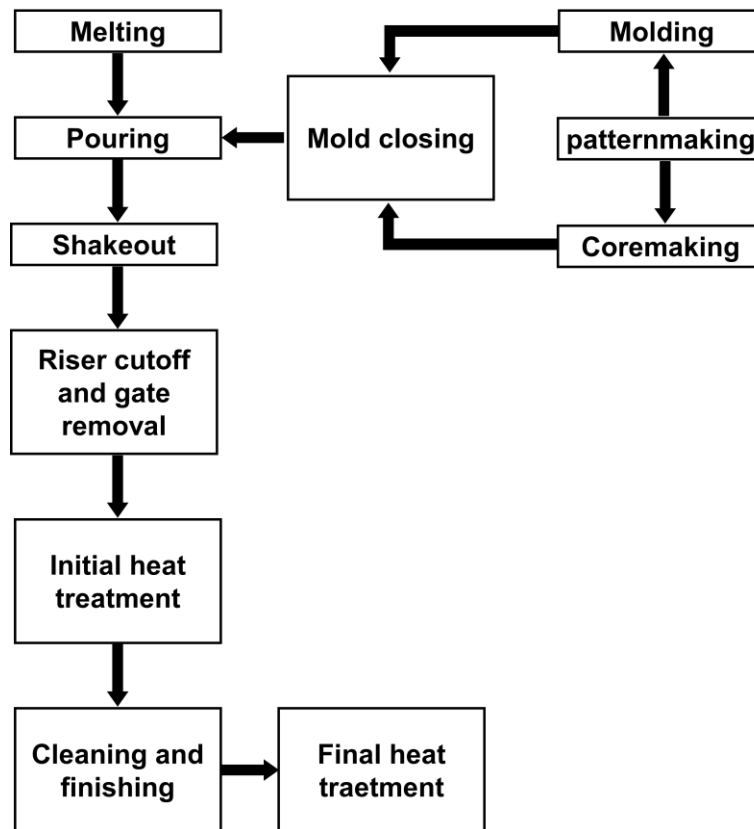


Figure 2.5 Flowchart of the basic operations to produce a casting.

The development of new aluminum alloys and the study of their physical and mechanical properties have made way for the creation of new products. Consequently, new smelting processes and technologies are available to help the smelter to produce economical and reliable parts that meet the specific requirements of the product. The aluminum smelting process demands high levels of fluidity, hot strength, and hot tear resistance [32]

2.4.1 Stir Casting

In MMCs, reinforcing particles increase wear resistance and strengthen the matrix. In the manufacture of aluminum matrix composites (AMCs), different methods are used, such as powder metallurgy, spray deposition, liquid infiltration, squeeze casting, and stir casting. The selected method depends on the size and morphology of the particle, and the type of reinforcement. For instance, stir casting is an economical method, widely used in industries for its simplicity and flexibility. It further improves the bonding of the reinforcing particles due to melt agitation [19].

Choosing appropriate process parameters, such as casting temperature, uniform feed rate of reinforcement particles, mixing time and stirring speed, allows for uniform distribution and wettability of the reinforcing particles by the liquid alloy matrix. It also minimizes the porosity without affecting the chemical stability of the material [5]. Figure 2.6 presents a schematic of the stir casting process depicting elements affecting the process.

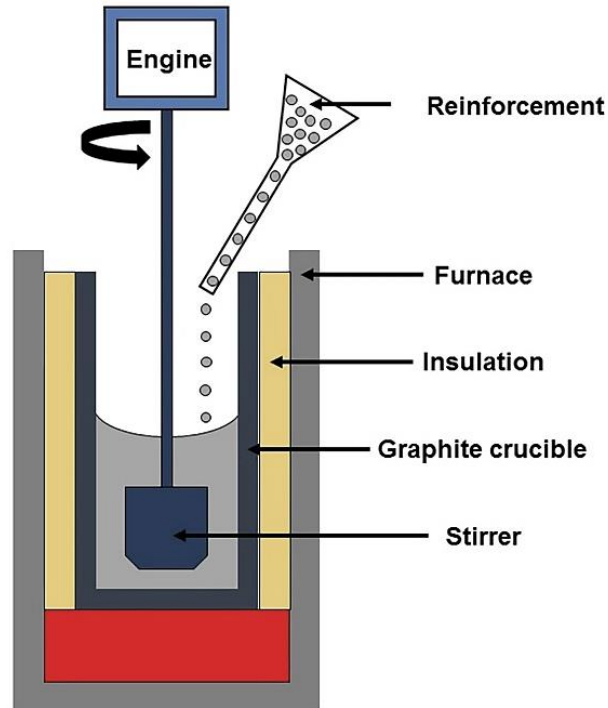


Figure 2.6 Schematic diagram of mechanical stir casting.

2.5 Cold Rolling

Some products require small thicknesses, tight tolerances, and high-quality requirements. These conditions are very difficult to achieve through casting process; instead, cold rolling is used to manufacture such products. This process improves the re-organization of the microstructure and mechanical properties of the cold-formed pieces. Historically, steel has been the dominant material in the production of metals via rolling. Nonetheless, during the 20th century, the availability of aluminum presented new alternatives and challenges to the manufacturing industry. Basic rolling technologies for steel and aluminum are nowadays based on the same general mechanical principles.

Rolling thin aluminum sheets is difficult and represents only half of similar products produced with steel [33]. For wire fabrication, Figure 2.7 shows how the desired diameter can be obtained through the cold rolling process.

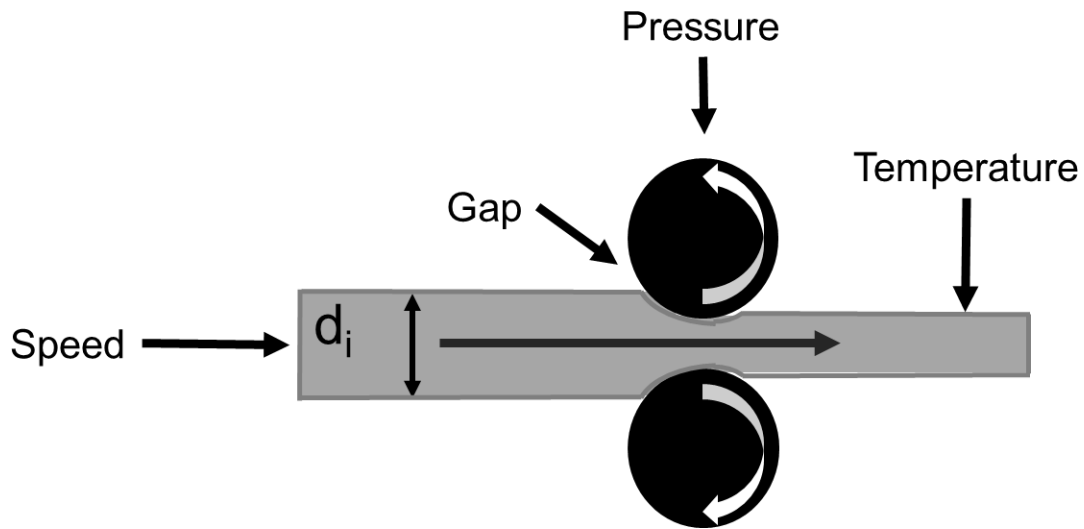


Figure 2.7 Cold rolling process diagram.

III. CHAPTER

3. Exploratory Experiments of Aluminum Filler Treated with NbB₂ Nanoparticles

This section of the chapter discusses some preliminary experiments conducted in order to better define the parameters and factors that affect the manufacture of an NbB₂ nanoparticle-reinforced aluminum welding filler. Such filler material must help achieve quality joining of two parts made of aluminum alloys. Industrial filler materials contain different types of strengthening alloying elements such as magnesium, manganese, silicon, and copper that improve melting upon welding.

3.1 Evaluating Welding for New Aluminum Filler

In this research segment, a new filler material containing nanometer size particles was explored. Its mechanical properties and weld quality were studied. However, one cannot achieve proper reinforcement by simply adding the nanoparticles into the liquid aluminum due to lack of wettability between the diboride and the liquid metal. Previous research demonstrated the effectiveness of using planetary ball mill to reduce the particle size of nanometric NbB₂ by fragmentation; using the same planetary ball mill, the authors were able to embed the nanoparticles in the aluminum matrix by cold welding [9]. In the following section, the methodology for manufacturing the nanoparticle-containing filler is discussed, along with the pertinent quality tests to measure hardness, porosity, and ultimate tensile strength (UTS).

3.1.1 Methodology

The methodology employed upon this preliminary part encompassed two stages. In the first stage, the synthesis of Al-NbB₂ nanocomposite was developed in a prior study by Florian [9]. The second stage was designed to study the material in terms of the required specifications as a welding filler material. Hence, the following steps were implemented: a) the fabrication of rods with the NbB₂ nanocomposite as filler has been achieved; b) welding tests has been completed using TIG welding technique; and c) different characterization techniques have been carried out to assess the quality of the weld through hardness, porosity level, resulting microstructure, and tensile strength.

Synthesis of NbB₂ Nanoparticles

This procedure was performed in a vario-planetary high-energy ball mill (Pulverisette 4, manufactured by Fritsch GmbH, Idar- Oberstein, Germany). The high-energy ball mill was operated at 1,600 rpm for 10 hours to fragment the NbB₂ (Alfa Aesar, Ward Hill, Massachusetts, USA) particles to the nanoscale, as demonstrated in a prior research on diboride particles [34]. The particle fragmentation occurred via energy imparted by the grinding media and the milling balls to the material samples during consecutive impacts [35]. Two vessels of 45 ml containing 10 mm diameter tungsten carbide grinding balls allowed for appropriate fragmentation of the NbB₂ particles. Figure 3.1 illustrates the process within each vessel. The grinding settings for 10hr and results are presented in Appendix A.1. We used 1:10 ball to power ratio (BPR), as it is most scholarly common,

yet not the highest available BPR. A representation of the preparation for the ball milling process is shown in Figure 3.2.

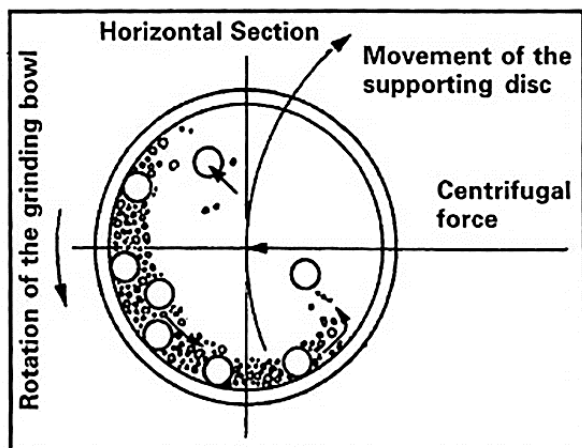


Figure 3.1 Schematic depicting the ball motion inside the planetary ball mill (Courtesy of Gilson Company, Worthington, OH.).

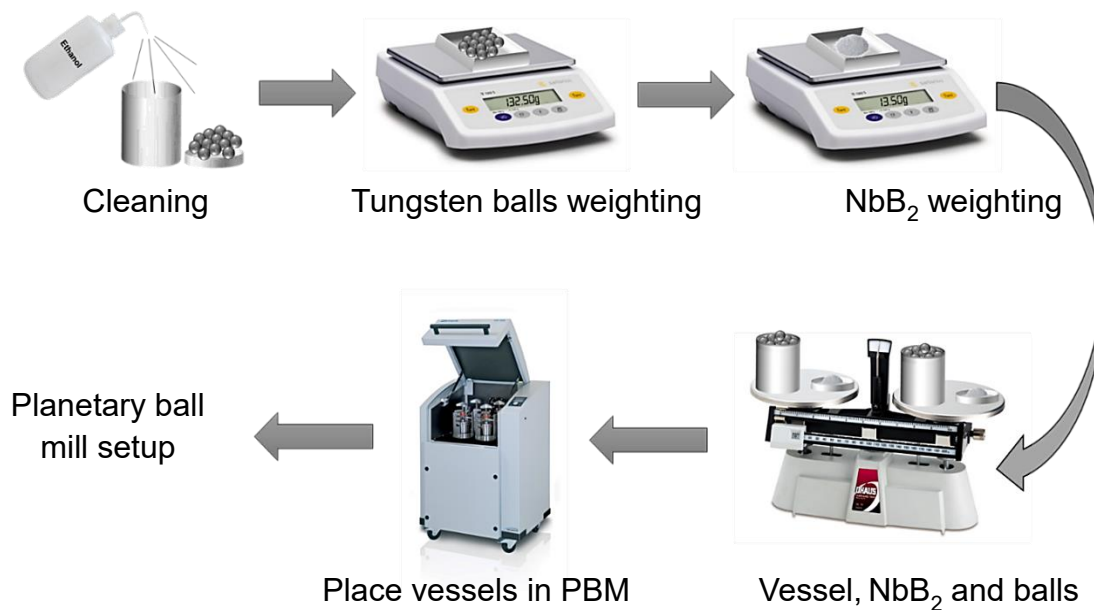


Figure 3.2 Visual representation of the preparation of the ball milling process.

In order to measure the average crystallite size of the particles, a Siemens® (Princeton, NJ, USA) D500 x-ray diffractometer was used with a $15-75^\circ$ 2θ range with Cu K α radiation ($\lambda = 0.154178$ nm). This procedure helped estimate the nanoparticle size using Scherrer's equation [36]. The calculated crystallite size of the NbB₂ nanoparticles was found to be 14 nm. Figure 3.3 shows the x-ray diffractogram of the powder before and after ball milling. The XRD pattern helps determine the crystalline phases, as well as how much of each crystalline phase is found in a compound.

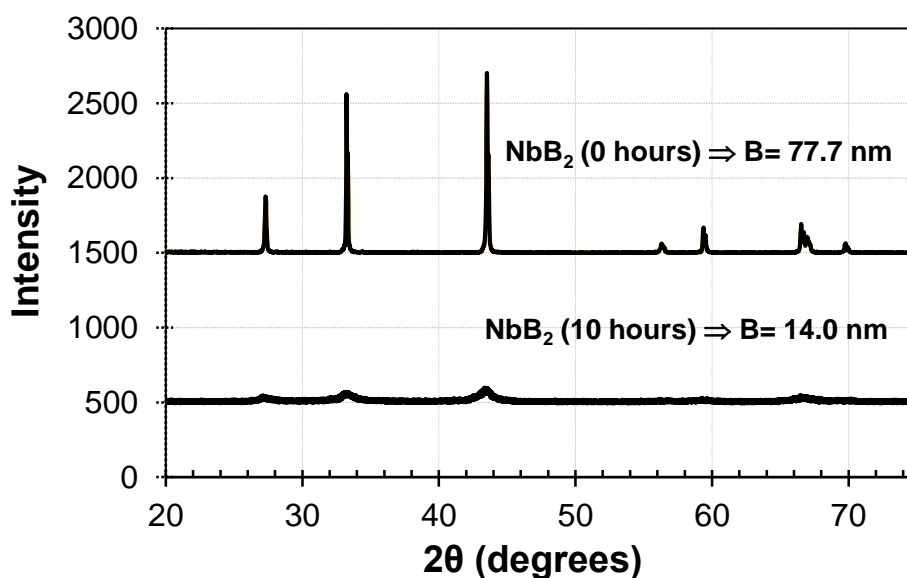


Figure 3.3 XRD pattern of NbB₂: as-received (without ball milling, upper spectrum), and NbB₂ particles after 10 hours of milling (lower spectrum).

Fabrication of the Al-NbB₂ Nanocomposite Pellets

To prepare the Al-NbB₂ pellets by mechanical alloying, we refurbished our PBM with two-grinding bowls and a support disk working independently of each other. Then, the resulting diboride powder was milled along with pure aluminum powder (Acros Organics,

Morris Plains, NJ, USA) for 1 h to form niobium diboride/Al nanocomposite pellets. Upon processing, the jar's inner walls and the mill balls hitting on the Al-NbB₂ mix induced cold welding. The pellets inside the jars can be seen in Figure 3.4. To understand this mechanical alloying process, Figure 3.5 shows the NbB₂ nanoparticle coated with aluminum due to the impacts. The rotational speed was set at 1020 rpm for 1h, with a BPR of 10: 1 following settings established in prior successful experimentations [37]. The cold welding settings and results are presented in Appendix A.2.



Figure 3.4 Nanocomposite pellets inside the jars after cold welding.

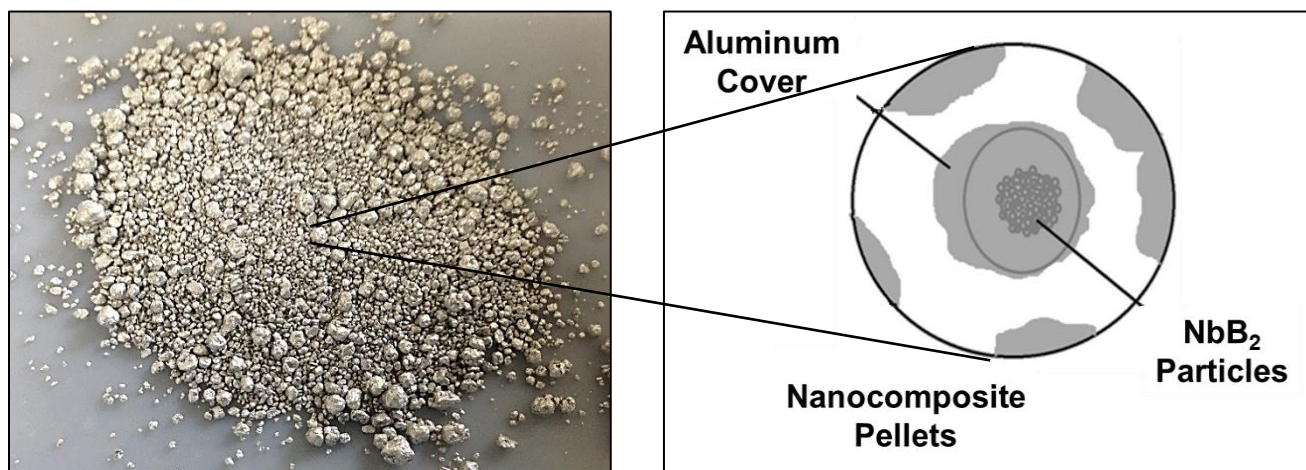


Figure 3.5 Schematic of the NbB₂ nanoparticles coated with aluminum as a result of the impacts.

After ball milling and to enhance the aluminum/diboride interface in the pellets, we sintered them. The process not only sought to improve the Al-NbB₂ pellets interface, but also to reduce the porosity inside the composite pellets [9]. The 200°C heat treatment lasted for 30 minutes in a reduced vacuum atmosphere (4 KPa). This heat treatment also enhanced the aluminum/diboride interface by removing residual stresses in the Al-NbB₂ composite produced during the intense plastic deformation caused by ball milling.

Filler Manufacture through Casting

Pure aluminum (99.5%) was melted at 780°C in a graphite crucible. We added the Al - NbB₂ pellets to the melt and manually stirred it for 15 seconds. We then poured the molten material into a cylindrical mold to produce 5 mm diameter ingots.

Cold Rolling

The ingots were cleaned and cold rolled in a manual rolling machine. The final fillers were obtained when the rods reached a diameter of about 2.4mm and 12 inches long. Figure 3.6 shows the cold rolling process of the ingots. These dimensions were necessary for the thickness of the AA6061 base plate, i.e. 6.35 mm. In effect, AWS recommends using a 2.4 mm diameter filler to achieve a better joint between the metals and filler.



Figure 3.6 Cold rolling process of the cylindrical ingots.

Welding

The samples were welded using TIG welding. Two types of filler materials were used for the tests. The first filler was the experimental 99% Al - 1% NbB₂, and the second was an AA 5356 (PowerWeld, Grand Prairie, TX, USA) commercial filler. The base material was an AA 6061 aluminum alloy since it has low cost, excellent toughness, and versatility for structural applications. The chemical composition of the samples, filler materials, and the base material are shown in Table 3.1.

Table 3.1 Chemical composition of base material and fillers material (wt.%).

	Mg	Mn	Cr	Cu	Fe	Si	Ti	Zn	Be	NbB ₂	Al
AA 6061 Aluminum alloy (base material)	≤1.2	≤0.15	≤0.35	≤0.4	≤0.7	≤0.5	≤0.1 5	≤0.2 5	-	-	Balance
5356 (filler material)	≤5.0	0.2	0.2	0.1	0.4	0.25	0.2	0.1	3E-04	-	Balance
Al-NbB ₂ Alloy (filler material)	-	-	-	-	-	-	-	-	-	≤ 1.0	Balance

To remove the oxide layer before welding, the samples were cleaned with a steel wire brush and completely washed with acetone. As indicated previously, based on the literature, one can conclude that influential parameters concerning the geometry of the weld and the fusion zone are peak current, base current, and pulse rate [22]. The welding parameters were controlled by the TIG welding unit presented in Figure 3.7, a Lincoln Electric Precision TIG 225 230V AC / DC TIG machine. The range of parameters and constant settings used are provided in Tables 3.2 and 3.3, respectively.



Figure 3.7 Lincoln Electric Precision TIG 225 230V AC / DC TIG.

Table 3.2 Working range of the welding process.

Process parameter	Units	Lower level	Higher level
Peak current	Amps	70	170
Welding speed	mm/min	200	230

Table 3.3 Constant Lincoln Electric Precision 225 AC/DC TIG machine parameters.

Process parameter	Units	Constant value
Pulse frequency	Hz	Automatic
Shielding gas flow rate	Psi	18
Post flow of shielding gas	Seg	15
Cleaning action	%	50
Weld penetration action	%	50
Electrode material	%	100 W
Electrode diameter	mm	2.4
Filler rod diameter	mm	2.4
Current	Voltage	Ac

Quality Tests

Since the manufacturing process was manual, it was difficult to produce a high number of samples. For this reason, we manufactured enough material to test only two samples of each filler. For the Brinell test the samples were indented seven times per sample, and for the tension tests were two samples. Four quality tests were performed on the welded samples: Brinell hardness tests, porosity measurements, optical microscopy, and tensile tests.

3.1.2 Results and Discussion

Brinell Hardness

The Brinell test measures the hardness of a material by penetrating an object into the material to be studied; therefore, to some extent, hardness is the material's resistance to plastic deformation on and near the surface. To perform the test, an LCR-500, manufactured by LECO durometer in Michigan, USA, was used, following the ASTM E10 - 17 (Standard Test Method for Brinell Hardness of Metallic Materials) and the ASTM B647 - 10 (Standard Test Method for Indentation Hardness of Aluminum Alloys by Means of a Webster Hardness Gage) standards. A 3.175 mm diameter steel ball allowed applying a 15 kgf force to indent the material. The indentation on the sample can be observed in Figure 3.8. Then, the Brinell hardness can be calculated using equation 01. The final result is in Megapascal.

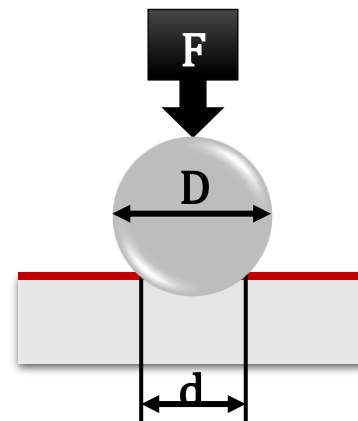
BHN = Brinell Hardness Number (kgf/mm²)

$$BHN = \frac{2F}{\pi D * (D - \sqrt{D^2 - d^2})} \quad (eq. 01)$$

F = applied load in kgf

D = diameter of indenter (mm)

d = diameter of indentation (mm)



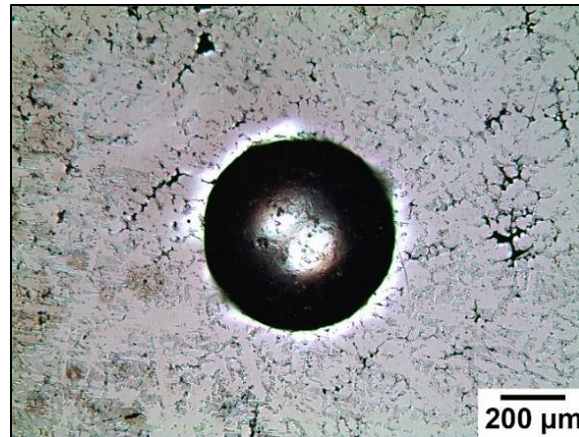


Figure 3.8 Indentation on weld with NbB₂ nanoparticles.

The purpose of this chapter was to evaluate the quality of the nanocomposite as a welding filler material. In order to measure the quality of the weld, we used a characterization technique to measure the physical properties of the material and also to provide information on the reinforcement distribution in the weld. This type of characterization is commonly used to develop materials because of its low cost and the option of performing multiple tests on the same sample.

A total of seven indentations were run per sample. The resulting low-quality welds could be due to a non-uniform distribution of the nanoparticles in the filler. Our hardness analysis helped conclude that there existed such lack of distribution of NbB₂ reinforcement in the filler (Figure 3.9). Also, the difference between means is probably significant because the interval bars do not overlap. Therefore, the casting procedure needed to be adjusted to improve the distribution of the nanoparticles in the filler.

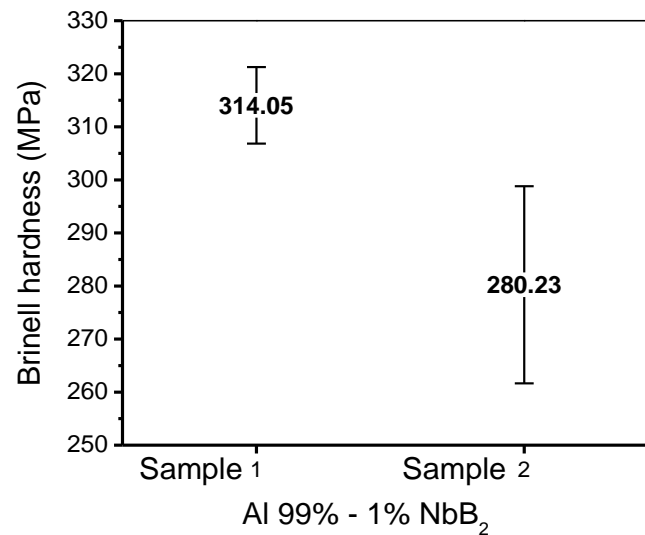


Figure 3.9 Hardness analysis of the Al-1wt% NbB₂ filler.

Porosity Test

As mentioned before, the porosity test is an excellent indicator of weld quality. To this purpose, the welded sample was cut transversely (to the weld direction) and polished; the porosity was observed in an optical microscope. ImageJ, an open source image processing package, was used for particle counting and analysis. The said porosity of these preliminary welded samples is apparent in Figure 3.10 and is 4% high for welding quality requirements. The resulting measured porosity is presented in Figure 3.11.

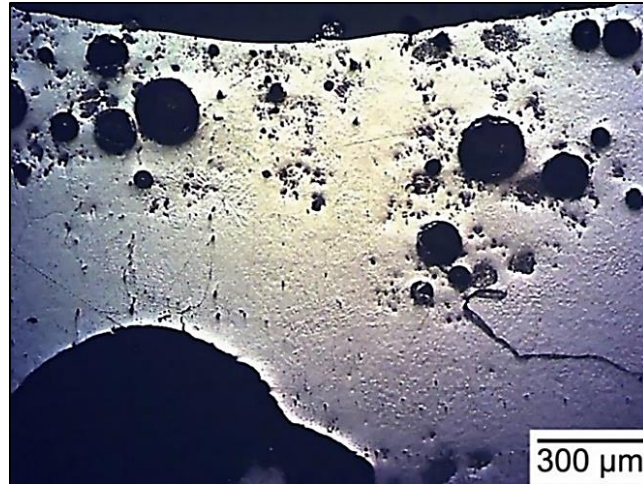


Figure 3.10 Porosity of the weld with 99% Al - 1% NbB₂ filler.

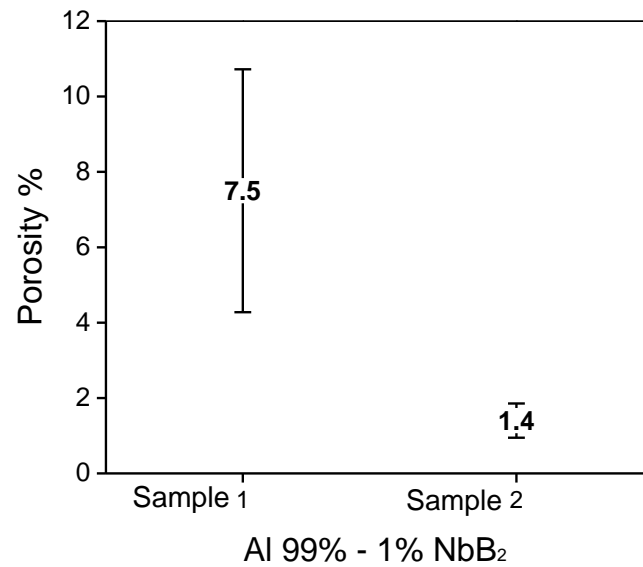


Figure 3.11 Percent porosity of preliminary welded samples.

Optical Microscopy

After these series of experiments, one can conclude that welding using the experimental fillers is feasible although with a low quality, as some cracks and pores of large size were present. Some partial fusion (PF) is also apparent. This PF occurred because of the failure of the welding process to melt the filler and base metal at the same time (Figures 3.12 and 3.13).

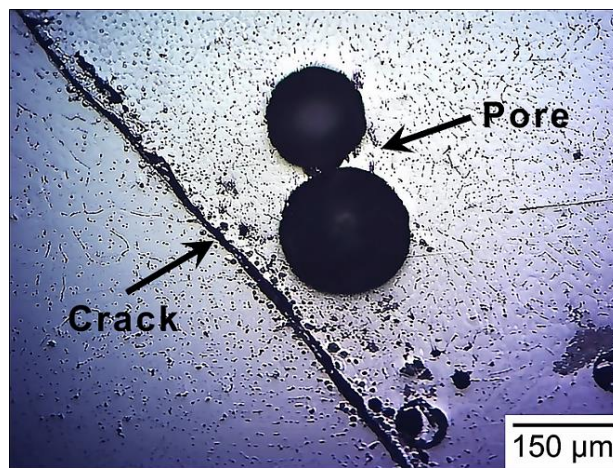


Figure 3.12 6061 plates welded with Al-1wt% NbB₂ filler.

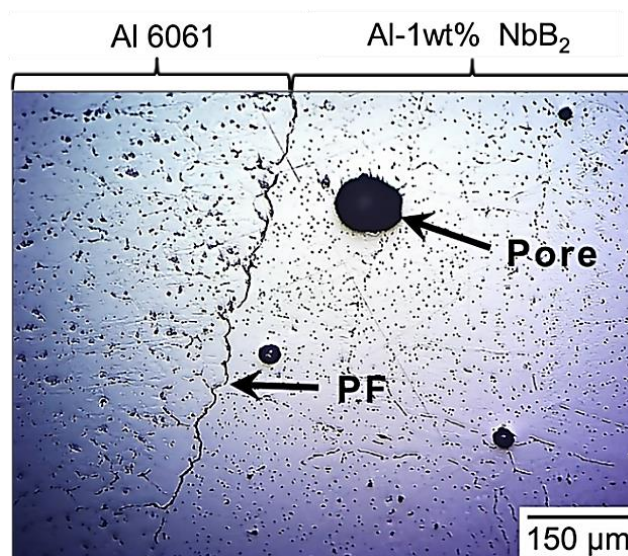


Figure 3.13 Partial fusion (PF) of welded AA 6061 plates with Al-1wt% NbB₂ filler.

Tensile Tests

Tensile tests allowed for further comparison of the nanocomposite with the commercial filler material, i.e. AA 5356. This filler is the most widely used in the aerospace and maritime industry. Two AA 6061 plates were welded with the two competing fillers as samples to perform the test. The sample welded with the 5356 filler had a Ultimate tensile strength of 142 MPa, whereas the one with the nanoparticle filler (Al-1wt% NbB₂) had a 48 MPa UTS and the unwelded 6061 plate had a UTS of 134 MPa, as presented in Figure 3.14. This analysis was carried out to compare the weld efficiency between the different filler materials and the base material. These preliminary experiments helped set parameters such as the mold temperature, stirring temperature, and amount of material to melt required for the manufacturing of a better-quality filler. The experiments were also helpful in finding the factors (stirring time and stirring speed) that would make up the full factorial design in order to optimize the production of the filler by stir casting.

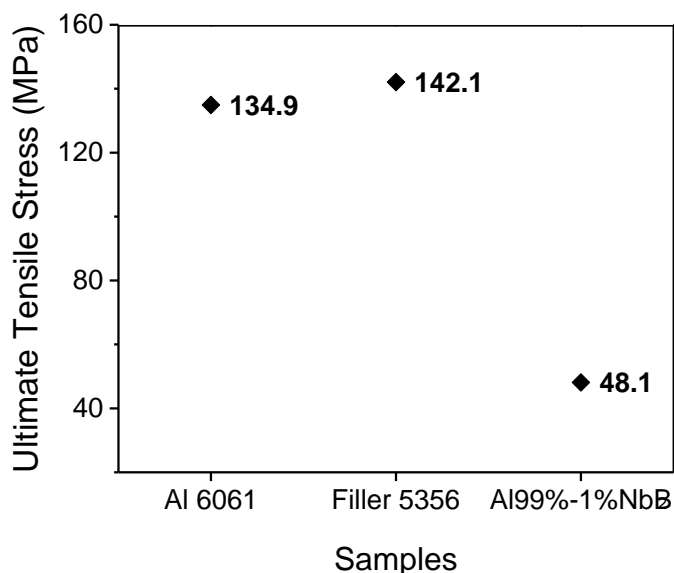


Figure 3.14 Preliminary UTS measurements.

3.1.3 Conclusions

- ♦ The preliminary experiments conducted provided evidence that welding was possible, although with a lower quality than expected, and that proper joining was not achieved between the materials with the casting parameters used for the filler.
- ♦ The weld presented very low UTS compared to the base material and the AA 5356 filler. Porosity percentages were too high for welding quality requirements, and directly affected the weld strength. To overcome these problems, new experiments were required, incorporating techniques that could warrant a homogenous distribution of the reinforcement.
- ♦ We also deemed important to add alloying elements to the experimental filler, enabling a better comparison with the commercial material. This experiment is detailed in the next section, where we discuss the methods we used to improve uniform distribution in the reinforcement. The section also discusses the analysis and methodology employed to find the main factors that affect the reinforcement distribution. These parameters can be measured through an experimental design that would help predict the overall effectiveness of the manufacturing process.

3.2 Techniques to Improve Uniform Distribution of NbB₂ Nanoparticles

As discussed in the literature review, researchers have employed ceramic materials to reinforce the aluminum matrix and improve its physical properties. Different methods allowed achieving a uniform distribution of reinforcement and providing good adhesion of the particles to the aluminum matrix. However, these methods are costly and sometimes difficult to produce in an industrial scale. In this respect, stir casting is a relatively simple and inexpensive method to produce metal matrix composite materials with proper reinforcement dispersion. During this process, the effect of casting factors, melt stirrer speed, and stirring time in the Al-Mg alloy have been studied. In effect, the first section of this chapter showed that it was possible to use casting to produce our nanocomposite as filler material for welding aluminum. Unfortunately, the hardness results showed poor reinforcement distribution, and less tensile strength than the AA 5356 filler. In order to increase the resistance of our filler material, the same amount of magnesium (was added to make it comparable as the AA 5356, i.e. 5 wt.%. This section describes the implementation of the agglomeration breakdown process to achieve uniform dispersion in the Al-NbB₂ nanocomposite pellets, as well as the implementation of the stir casting technique for manufacturing the filler with those NbB₂ nanoparticles. In previous studies, this method achieved a homogeneous distribution of reinforcements in the metal matrix composite. In addition, the welding procedure specifications (WPS) followed the AWS 5-10 standard of the America Welding Society. To measure the distribution of the reinforcement, Brinell hardness testing was performed, as well as a porosity test to measure weld quality.

3.2.1 Methodology

Fabrication of the Al-NbB₂ Nanocomposite Pellets Using Agglomeration

Breakdown Process

A uniform mix of Al powder and NbB₂ nanoparticles is mandatory to prepare homogeneous Al-NbB₂ nanocomposite pellets. These pellets are necessary for two reasons. First, a homogeneous particle distribution, after the NbB₂ milling, is necessary since some agglomeration could have occurred. Second, upon melt inoculation, the nanocomposite pellets favor the incorporation of the aluminum-bearing nanoparticles into the melt, offsetting the lack of NbB₂ wetting by the molten alloy.

As aforementioned, to improve particle dispersion, we used a hot plate stirrer to mix an isopropanol solution with the NbB₂ and Al powders, with an Al-NbB₂ proportion of 90:10. The solution was stirred at 250 rpm for approximately 72h, at 60°C, inside a fume hood. Homogenization continued as the liquid evaporated, leaving the homogenized NbB₂ and Al particles mixture dry and uncontaminated. Figure 3.15 presents the process of breaking down the agglomeration and achieving uniform dispersion in the nanocomposite. The cold-welding process and the heat treatment were performed with the same parameters previously used. The manufacturing process of the filler material by stir casting is explained below.

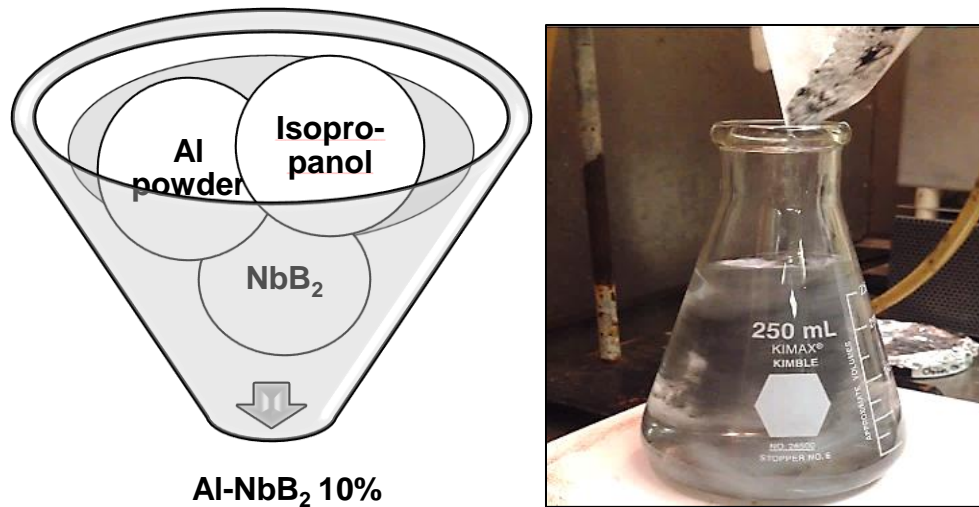


Figure 3.15 Agglomeration breakdown process to achieve uniform dispersion in the nanocomposite.

Filler Manufacture through Stir Casting

For the fabrication of our filler material a casting process is required, but this method was not sufficient to achieve the required welding quality. To improve such quality, we had to enhance the distribution of reinforcement upon casting and reduce the porosity. In our research, to further the quality of the reinforcement, we must take several factors into account, for example, material type, reinforcement, equipment, the number of castings to be produced, dimensional accuracy, size and shape of the piece, and the mold material. The coordination of all these factors is necessary to achieve the specified requirements for quality. In addition, the most important factors associated with the distribution of the reinforcement are the melt speed stirrer and the stirring time. To perform this experiment, the mixing speed was set at 600 rpm and the time was set at 15 seconds. Our objective was to study the effect of the stir casting on the filler with NbB_2 nanoparticles. Further,

levels of 1 and 2 wt% NbB₂ nanoparticles were studied to measure the variation of the physical properties of the filler, and to the control sample used. A diagram of the stir casting process is shown in Figure 3.16.

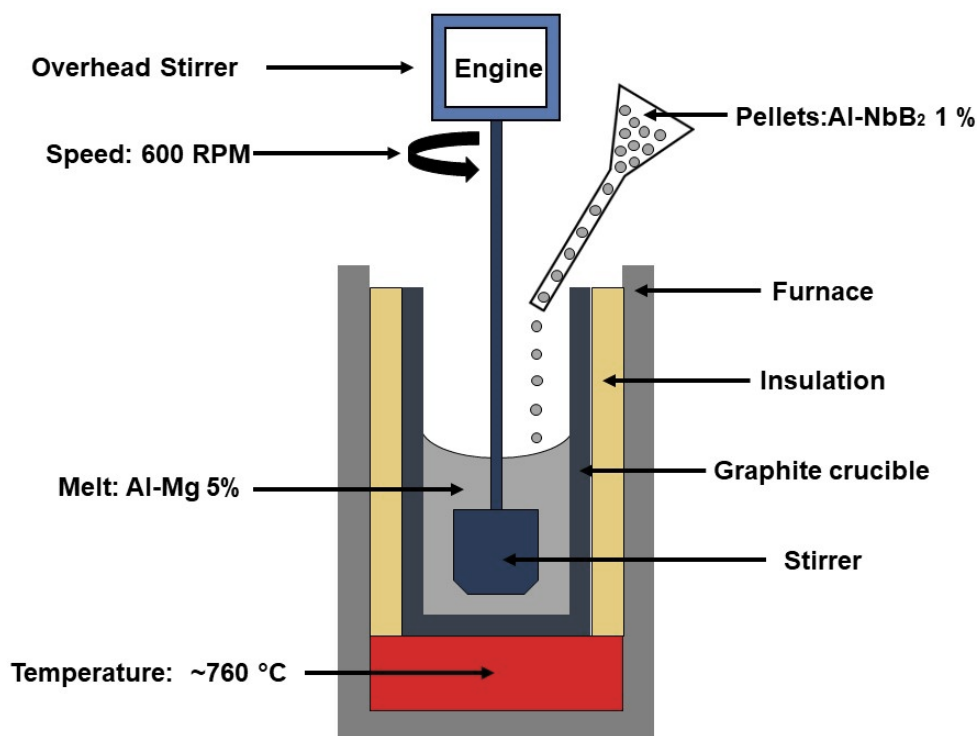


Figure 3.16 Schematic of the stir casting process.

Another important aspect of the experimental methodology was to make sure the stirrer was able to mix the melt components (charge material) at 700 °C and at speeds of 1000 RPM. Thus, the stirrer must meet two requirements. The first requirement is to be sufficiently strong and resistant to friction. Second, to avoid contamination with the stirrer materials, this stirrer must have a small enough diameter to prevent wear of the graphite crucible walls through friction while mixing the melt. The crucible had an internal diameter of 38 mm and a height of 110 mm. Figure 3.17 shows the crucible used during the experiment.

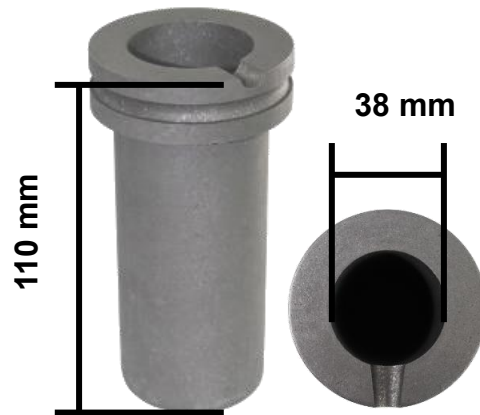


Figure 3.17 Drawing of the crucible used during the experiment.

A steel hex shank wood flat drill bit was adapted to function as a stirrer. After machining and finishing, the final dimensions were 20 mm x 3 mm x 24 mm. Figure 3.18 shows the modified drill bit used as stirrer to help attain a uniform distribution of the reinforcing NbB_2 particles in the Al-Mg alloy. Figure 3.19 depicts the stirrer design inside the graphite crucible.

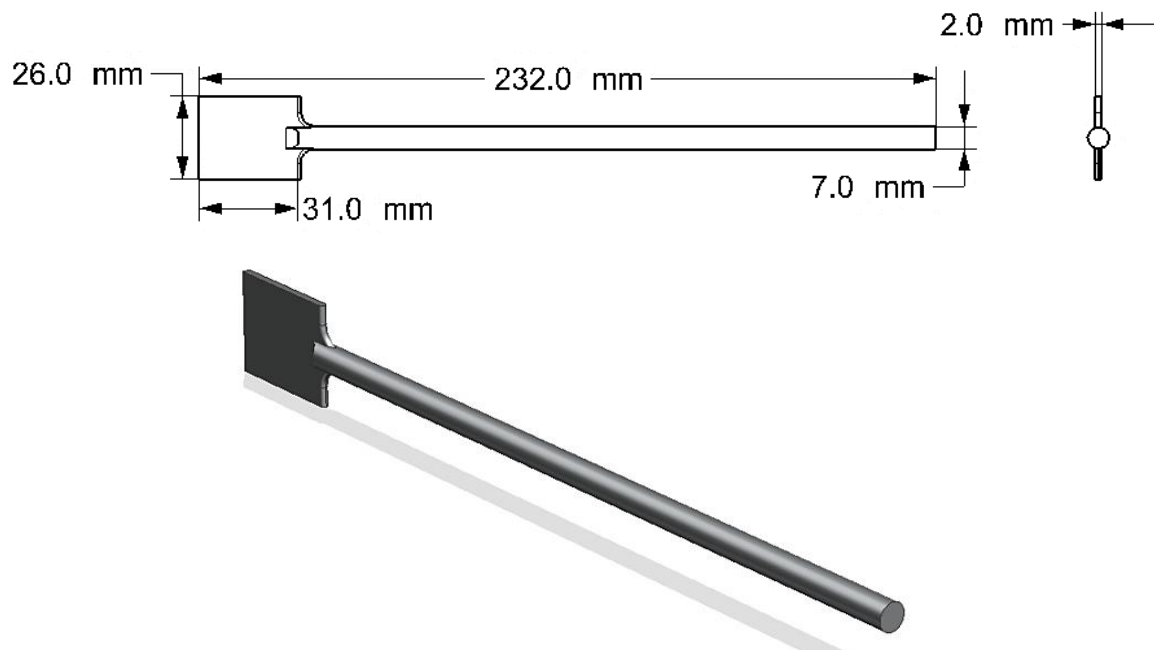


Figure 3.18 Stirrer schematic and 3D model.

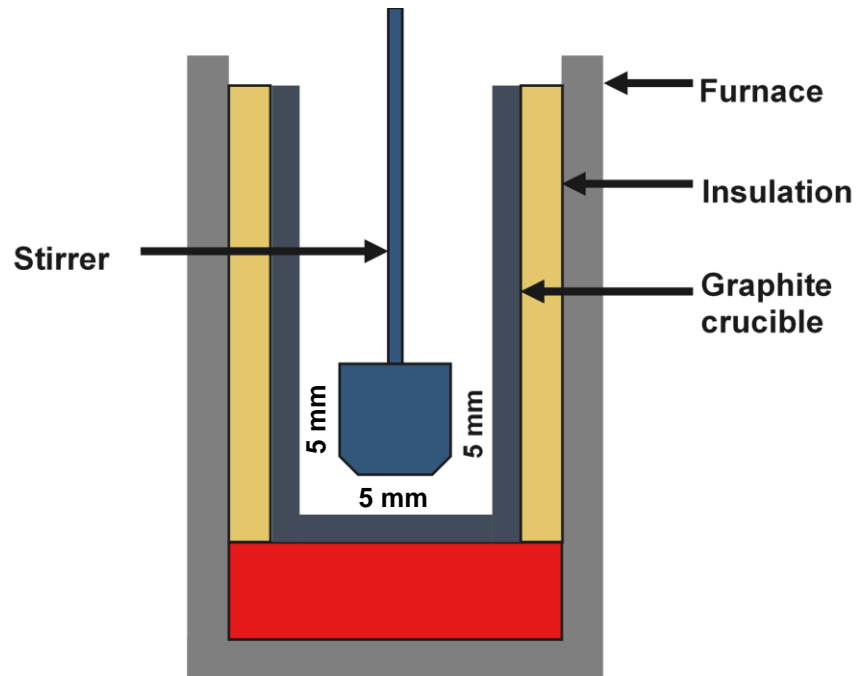
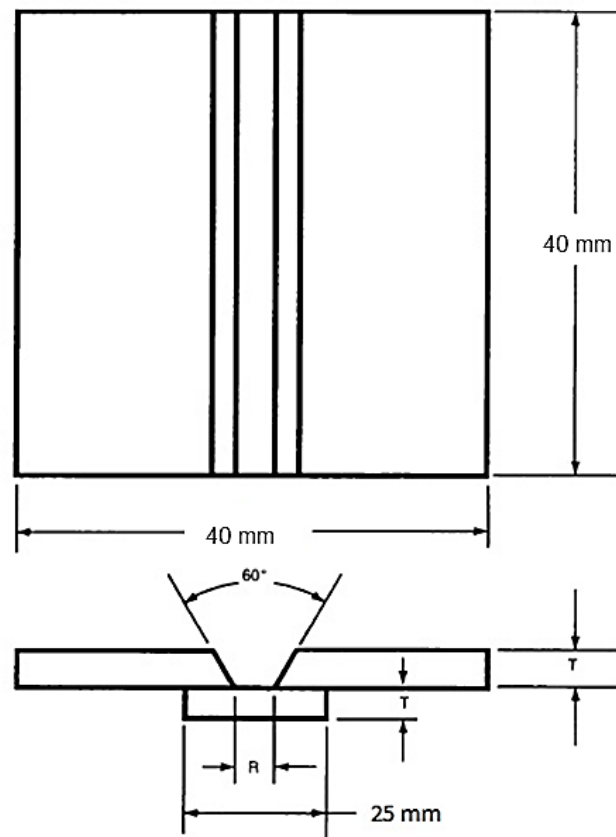


Figure 3.19 Schematic of the stirrer inside the graphite crucible.

The Welding Procedure Specification

To study the weld quality, a single V-groove weld (60° angle) was used to test the filler material. As previously mentioned, the base material for the welding test was commercial AA 6061 aluminum alloy plates. Figure 3.20 shows a schematic of the groove weld test assembly. We prepared the samples following the AWS 5 -10 standard of the America Welding Society.



Electrode Diameter		Plate Thickness (T)		Minimum Root Opening (R)		Welding Position
in.	mm	in.	mm	in.	mm	Flat
3/32	2.4	1/4	6	1/4	6	

Figure 3.20 Groove weld test assembly dimensions.

The Brinell hardness and porosity tests of the manufactured specimens followed ASTM E10 - 17 and ASTM B647 - 10 standards. Five indentations per sample were performed on the entire surface of the weld to indirectly reveal the distribution of the reinforcement.

Sample Preparation

After welding the test specimen (Figure 3.21), the excess material was cut off. These pieces were then polished to conduct the said Brinell hardness and porosity tests (Figure 3.22).

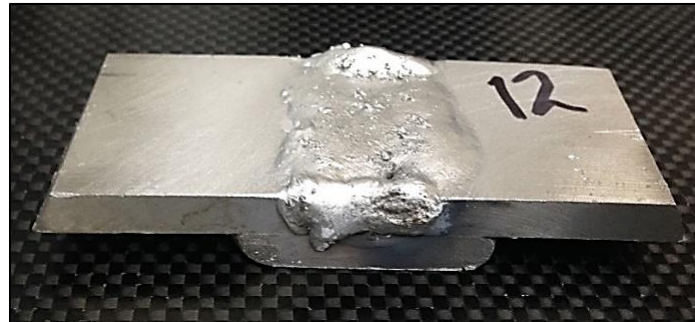


Figure 3.21 Test specimen welded with filler reinforced with NbB₂ nanoparticles.

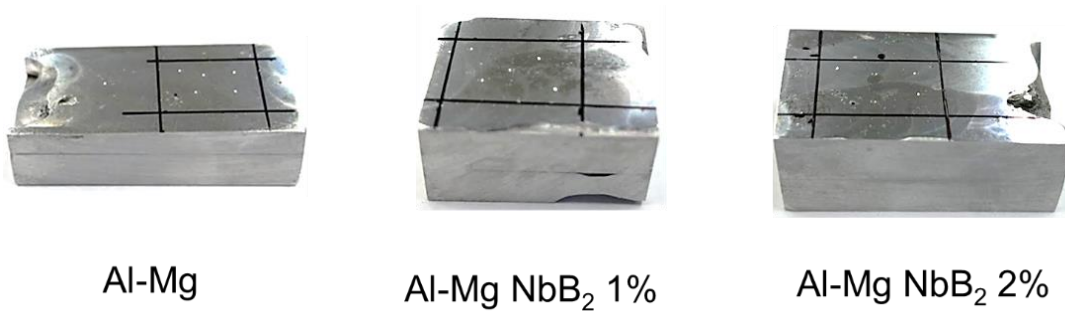


Figure 3.22 Polished samples for Brinell hardness and porosity tests.

3.2.2 Results and Discussion

Brinell hardness

The Brinell hardness results are shown in Figure 3.23 where the means are represented by the different NbB₂ amounts. The intervals of the filler reinforced with NbB₂ do not overlap with the filler without NbB₂. All five indentations were made across the weld. Figure 3.24 shows the hardness dispersion in the Individual Value Plot. The dispersion of the data is constant in the presence of the reinforcement, indicating that the distribution of the NbB₂ is homogeneous on the weld. These results also demonstrate that the NbB₂ nanoparticles increased in hardness 4% and 11%, by adding 1% and 2% to 5% Al-Mg, respectively.

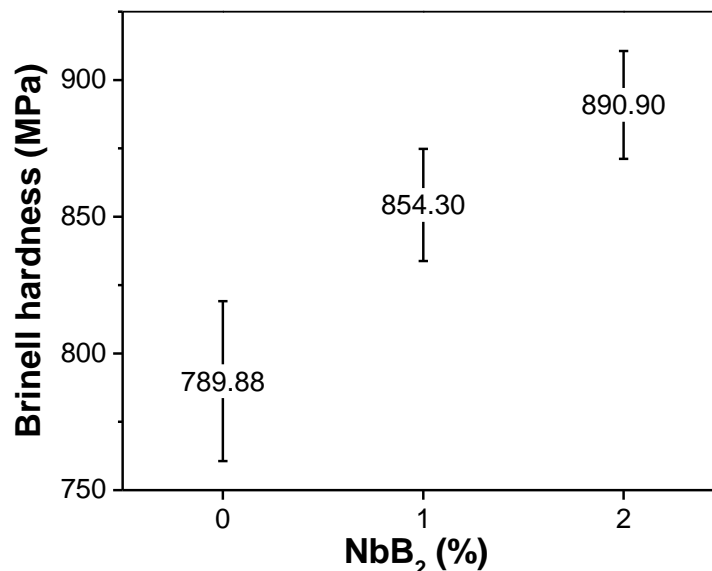


Figure 3.23 Hardness analysis of the Al-Mg 5% filler with NbB₂.

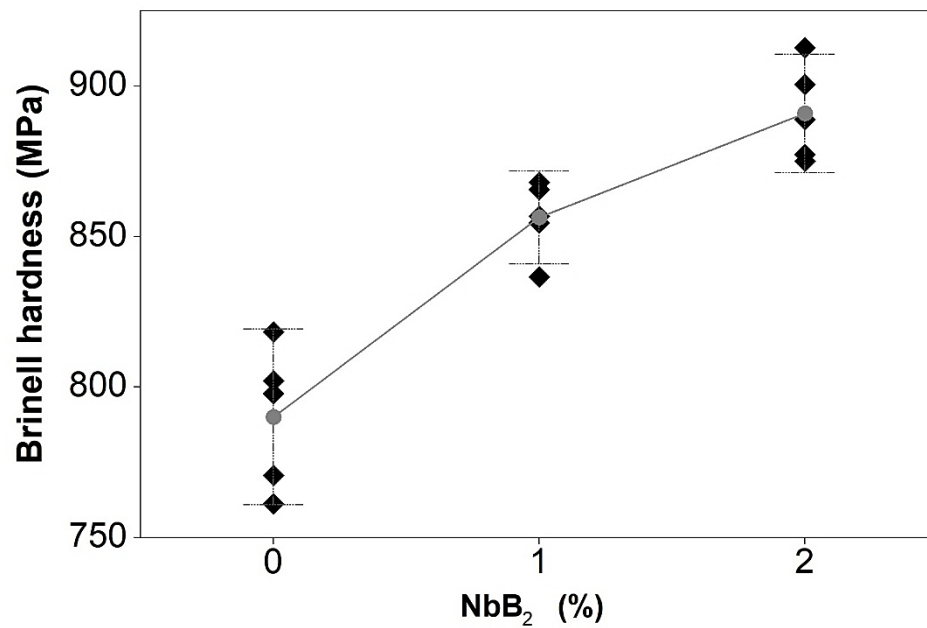


Figure 3.24 Individual Value Plot of Hardness analysis of the Al-Mg 5% filler with NbB₂ (95% CI for the Mean).

We examined whether the variances of the two treatments were similar using a 0.05 significance level. Figure 3.25 presents the confidence intervals for the ratio of variances and p-values for Bonett and Levene tests. These tests consider the distances of the observations from the sample median. The p-value of the Bonett's test is 0.575, whereas for the Levene's test is 0.505. This suggest that treatments have equal variances.

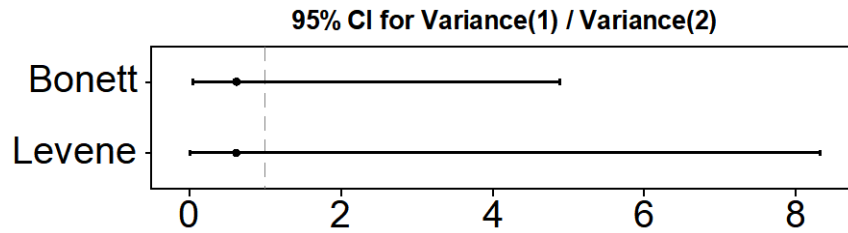


Figure 3.25 Test for two variances: 1% NbB₂ Weld, 2% NbB₂ Weld, Ratio = 1 vs Ratio $\neq 1$.

Porosity Tests

Porosity test can help assess weld quality, since the less weld porosity, the less the weld is prone to fractures. A total of 35 photos were taken to perform the analysis of porosity percent in each solid. Compared to previous experiments (Figure 3.11), the porosity was much lower using the stir casting method. Although, 2.6% porosity was found in the Al-Mg 2%NbB₂ sample because the material overheated during welding. The porosity of these samples is shown in Figure 3.26, and the porosity results are provided in Figure 3.27.

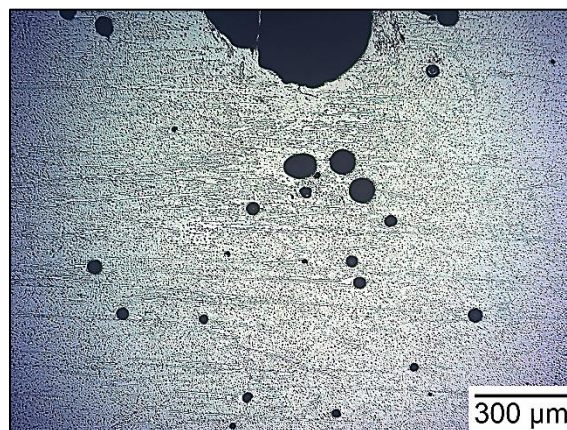


Figure 3.26 Porosity of the sample welded with Al-Mg-NbB₂ 2% filler.

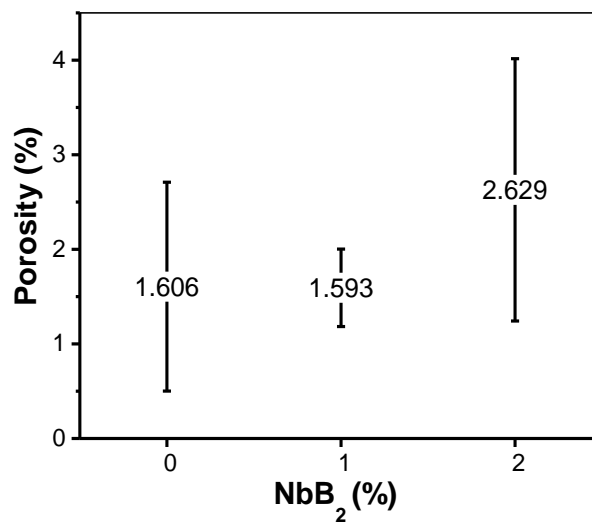


Figure 3.27 Percent porosity of welded samples.

Optical Microscopy

While analyzing the optical micrographs, low quality welding was observed, along with some slag, but there was no visible crack. Also, some porosity was apparent, which normally originates from poor gas shielding due to leaks in the gas line, a high gas flow rate and excessive turbulence in the weld pool. This allowed for the absorption of nitrogen, oxygen and hydrogen in the molten weld pool, resulting in porosity. Another problem that can cause porosity is the possible contamination generated during the manufacturing process of the filler material [27]. Figure 3.28 shows representative microstructures of the weld.

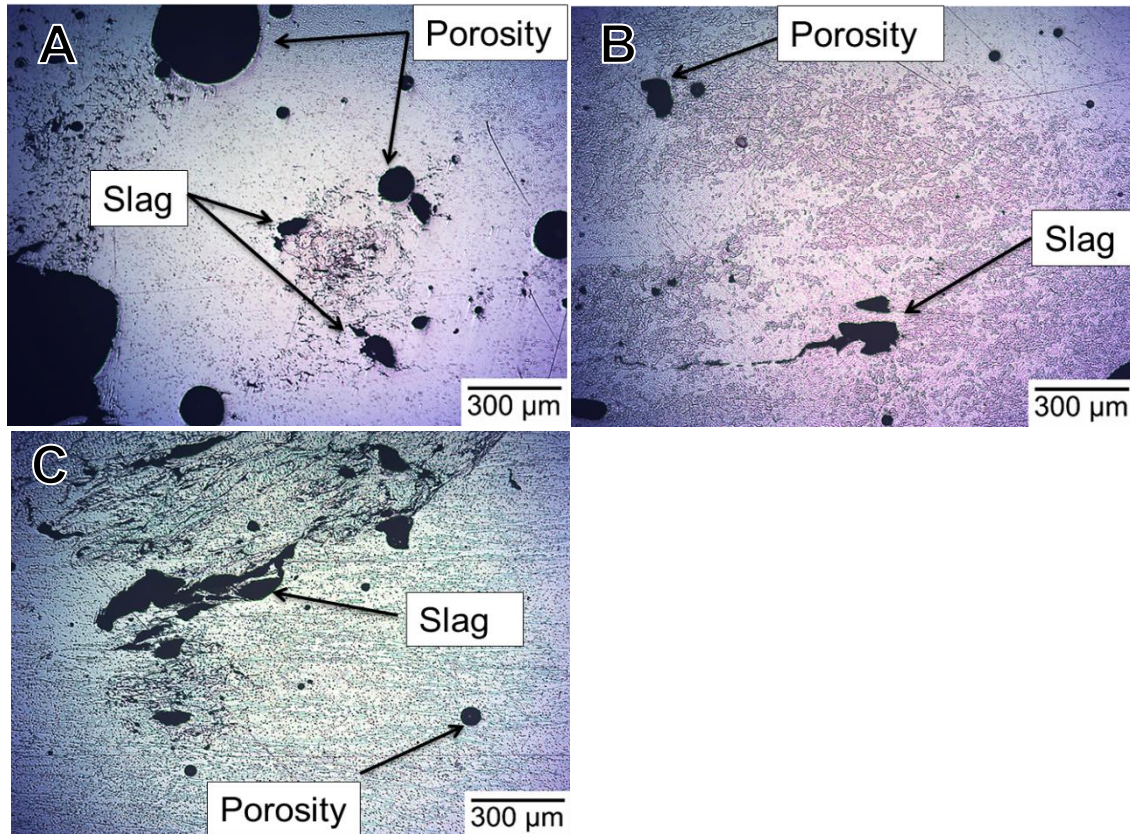


Figure 3.28 Optical micrographs of the weld: (A) Al-Mg 5%; (B) Al-Mg 5% NbB₂ 1%; and (C) Al-Mg 5% NbB₂ 2%.

3.2.3 Conclusions

- ♦ NbB_2 nanoparticles by adding 1% and 2% to 5% Al-Mg raised the filler hardness 4% and 11%, respectively.
- ♦ In the Al-Mg-2% NbB_2 sample, the observed 2.6% porosity was the likely result of overheating the material upon welding. Yet, the level of porosity in the weld was reduced below 3% from prior experiments. According to the literature on weld quality control, when below 4%, porosity does not impact welding significantly.
- ♦ The micrographs showed an inadequate quality weld, as some slag and cracks were found.
- ♦ The employment of stir casting during the manufacturing process allowed for a better distribution of NbB_2 nanoparticles during welding. The next step is to study the factors in the stir casting process in more detail, aiming at improving the filler manufacturing process. The agglomeration breakdown process attained a more homogeneous size and shape of the Al- NbB_2 nanocomposite pellets.

IV. CHAPTER

4. Optimization of Stir Casting Process of Aluminum Filler Reinforced with NbB₂ Nanoparticles

In manufacturing, optimization is a tool that helps design, control, and improve processes. In turn, optimization can be defined as the discovery of values for decision variables that fulfill competitively and simultaneously several measures of performance or criteria. To produce new metal matrix composites with reinforcement at nanometric scale, different types of processes have been implemented, seeking to better their mechanical properties and to make them commercially viable. Many of these processes are costly, since the resulting parts are difficult to manufacture continuously on a production line.

Stir casting is a method commonly used in the industry for its low cost and high effectiveness. Based on this reason, we analyzed the factors involved in stir casting filler material manufacturing. A statistical design of experiments (DOE) represented the best viable alternative to optimize this process in novel filler materials for aluminum welding. A DOE, aside from being an expeditious and inexpensive methodology, has some advantages, such as the possibility of building a system model that produces predictions without experimental data. Nevertheless, this methodology also has disadvantages: for instance, as the number of factors increase, the number of replicas also increases. For the realization of an experiment design, it is important to consider three stages: design, execution, and analysis. These should be planned considering the type of process and the difficulties of making samples (affecting reproducibility). Extensive knowledge of the

limitations of the characterization instrumentation must also be considered. The overall manufacturing of the fillers involves many external variables, such as the electrical system parameters, temperature and humidity in the laboratory, manual operations, amount and cost of material for production, as well as the preparation time, and many others that cannot be completely controlled.

There are different types of designs, such as factorial designs and the Taguchi method, for which a composite central design (CCD) was defined. The central composite DOE is one of the most used ones in process optimization studies. Thus, this methodology can develop an empirical model of the process to obtain an accurate estimate of the operating conditions of the stir casting [38].

4.1 Full Factorial Experiment of Stir Casting Process

Full factorials are used when several concurrent factors need to be studied to describe the general behavior of a process. Also, full factorials are necessary to find the combination of the factor levels that produce an optimal value of the dependent variable. This section, therefore, focuses on the full factorial analysis of the stir casting process for a filler material reinforced with niobium diboride nanoparticles for aluminum welding. Preliminary experiments showed uniform distribution of nanoparticles in the filler to improve weld quality. This improvement was achieved by the implementation of stir casting in the manufacturing process, as detailed in section 3.2. In addition, we incorporated a mixing technique to break up the agglomeration of the nanoparticles after

ball milling. This process ensured a homogeneous distribution of nanoparticles and uniform size in the pellets. Correspondingly, a full factorial experiment allowed assessing the effect of stir casting factors, namely melt stirrer speed and stirring time. Therefore, prior experiments helped identify the factor levels that allowed for the optimization of the manufacturing process of the ingots, which will then be used as filler material for welding. As a response variable, ultimate tensile strengths of the ingot were obtained.

4.1.1 Methodology

Full Factorial Design

A 2^2 full factorial design with 2 central points was used. Figure 4.1 shows the graphical representation of the full factorial, and Table 4.1 shows the factors with their respective levels. A total of 10 runs were completed with the order of runs randomly assigned by Minitab 17 statistical package. Ultimate tensile strength (UTS) measurements in our experiments corresponded to the response Y. The full factorial design matrix of Ultimate tensile strength obtained from Minitab is presented in Appendix B.1.

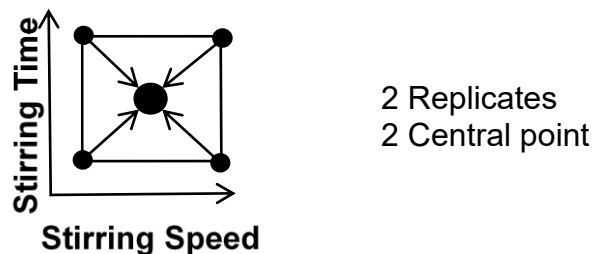


Figure 4.1 Full factorial design for stir casting process.

Table 4.1 2^2 full factorial parameter for stir casting process.

Parameter	Units	Lower	Higher
Stirring time	sec	5	25
Stirring speed	RPM	500	1000

Experimental Conditions

As aforementioned, there are three important steps in developing an experimental design: design, execution, and analysis. To perform this analysis, several experimental conditions were considered starting with the stirring speed levels. The instrument used for mixing was a digital overhead stirrer manufactured by Fisher Scientific. This instrument ranges in speed from 40 to 1,000 rpm. Thus, the fastest speed selected was 1,000 rpm. The instrument also has a digital speed control that allows for better precision. Moreover, one must consider that longer stirring times and high-speed mixing result in increased friction between the molten metal and the crucible walls. Hence, as a result of such friction, graphite particles removed from the crucible wall can cause melt contamination, which could lead to more porosity and poor weld quality. For this reason, the mixing time factor was limited at 50 sec.

Manufacturing process

For the manufacturing process, the new procedure for the synthesis of nanocomposite was used; for the stir casting process temperatures remained the same as in previous experiments. The melt was poured into a cylindrical mold to produce 5 mm diameter ingots. Figure 4.3 illustrates the manufacturing process to be analyzed via the full factorial DOE. Tensile tests were performed in specimens prepared from the said ingots, in order to verify their properties before being plastically deformed and welded. The test followed the ASTM B557M (Standard Test Methods for Tension Testing Wrought and Cast Aluminum- and Magnesium-Alloy Products) standard. The standard tensile test specimen was modified to fit the size of the ingot. Figure 4.2 shows the results of the tensile test specimen.

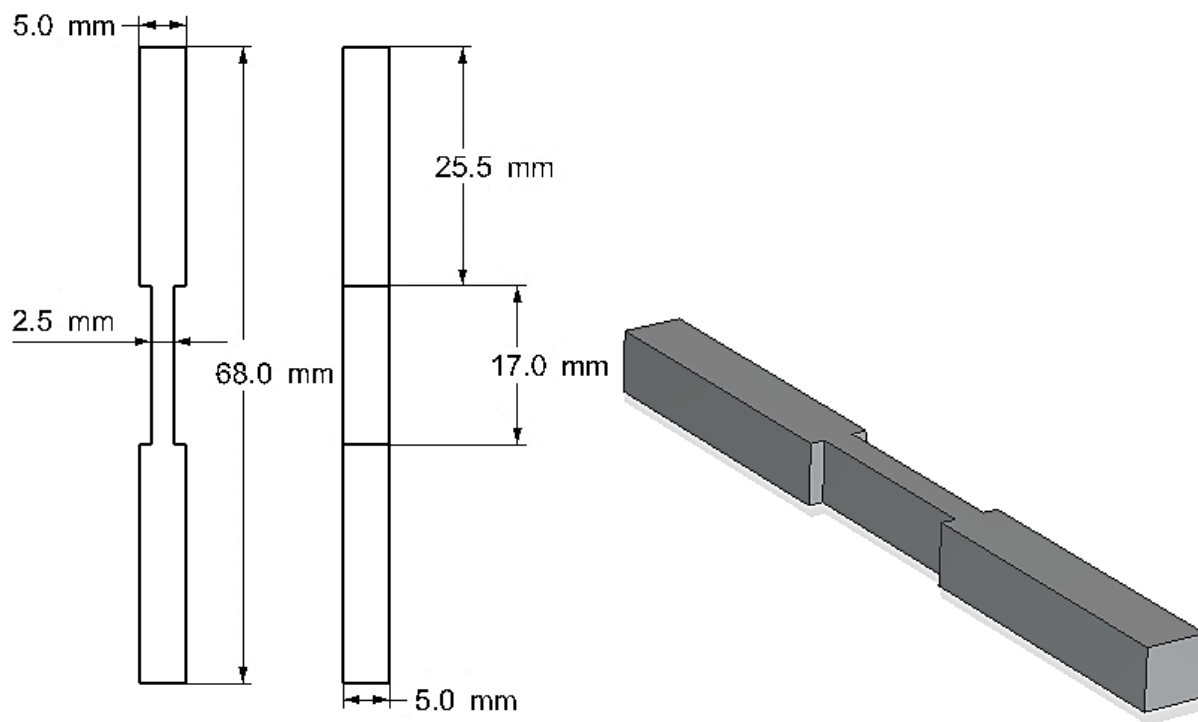


Figure 4.2 Schematic and 3D model of the tensile test specimen.

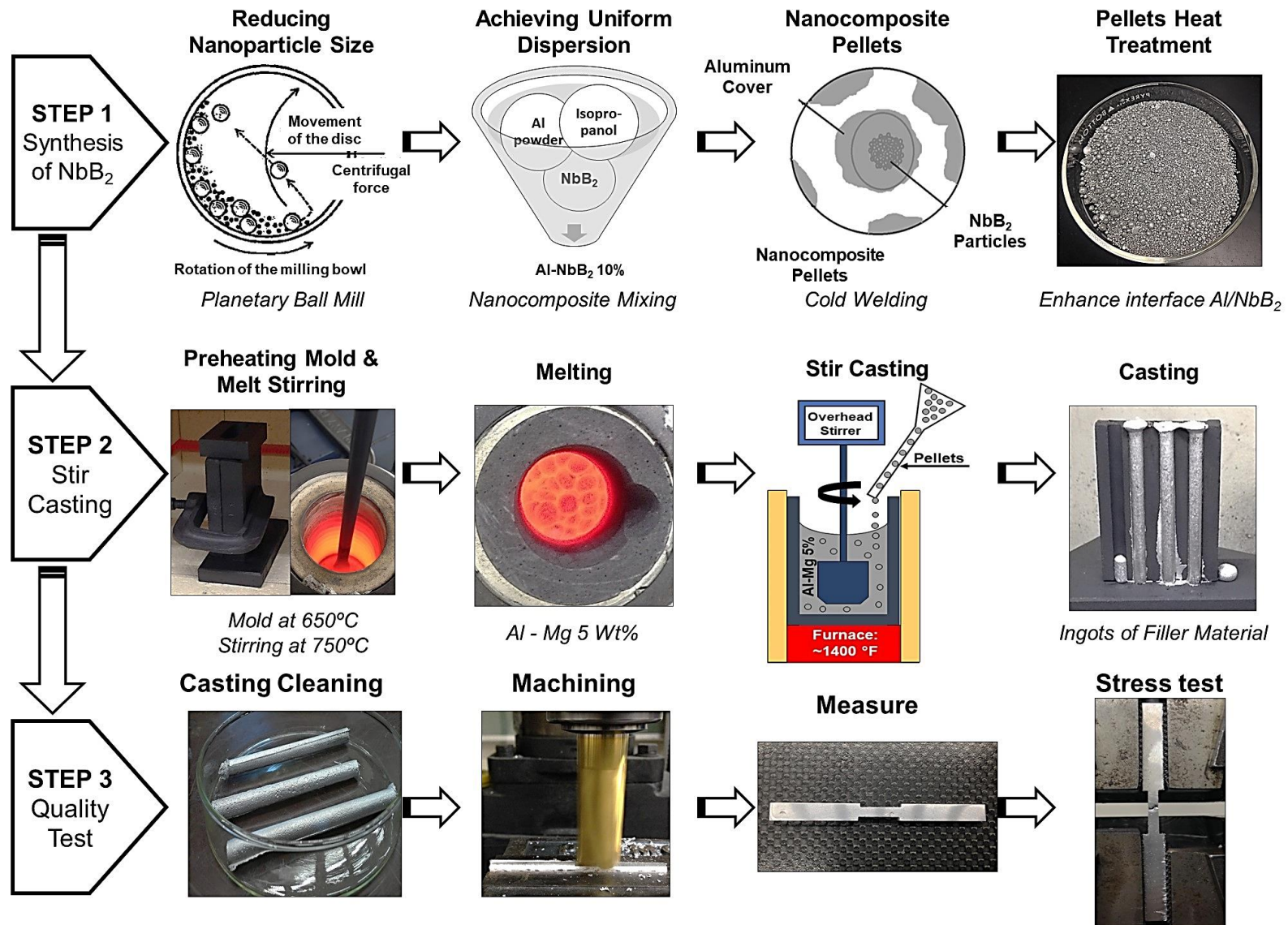


Figure 4.3 Diagram of the manufacturing process.

4.1.2 Results and Discussion

Factorial Design Analysis

Minitab 17 was employed to conduct the statistical analysis. The results are presented in Appendix B.1 together with the full factorial design matrix of the Ultimate tensile strength. First, the adequacy of the fundamental model was verified. We checked the normal distribution of the data by plotting the probability plot of the Ultimate tensile strength. The p-value was 0.569 and since it is larger than 0.05, one does not enough evidence to conclude that the results do not follow a normal distribution. Figure 4.4 shows the normal probability plot of UTS.

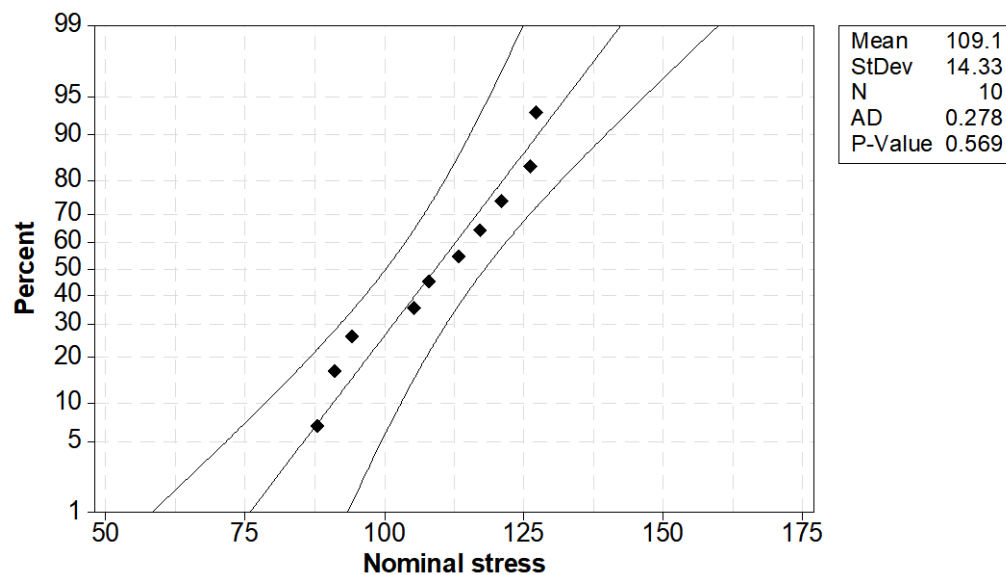


Figure 4.4 Normal probability plot of Ultimate tensile strength (95% CI).

Figure 4.5 shows the residuals versus fitted values of the Ultimate tensile strength.. In our case, we observed an inward opening funnel; this indicates that the variance increases as the response decreases. This is known as heteroscedasticity, so that the variance is not constant throughout the observations. One of the basic assumptions of the linear regression model is unfulfilled.

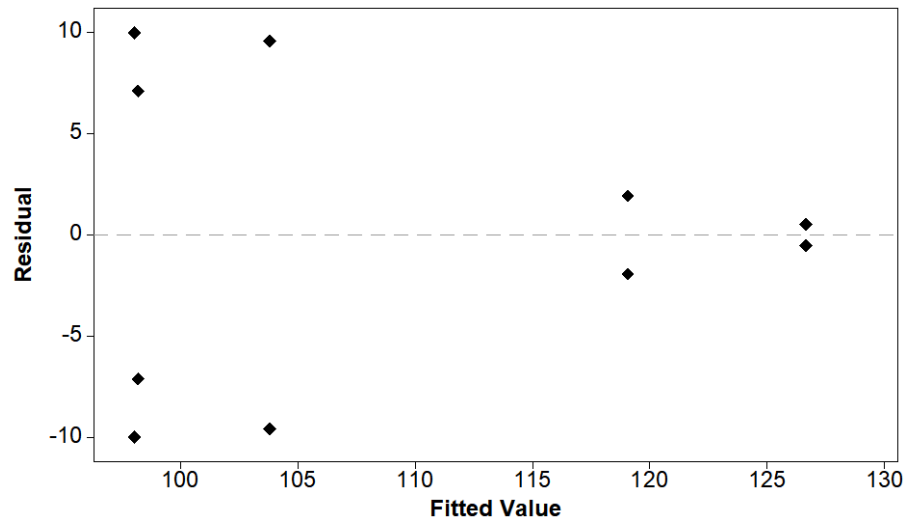


Figure 4.5 Residuals versus the fitted value of Ultimate tensile strength.

Therefore, we used a Box-Cox transformation that could help us correct the bias in the distribution of errors and the unequal variance. We could also identify extreme values, which can cause problems that can influence the regression model. The deleted residuals were used as an alternative to handle this problem. Figure 4.6 shows the normal probability plot of deleted residuals of Ultimate tensile strength. The graph reveals nothing particularly problematic with the normal distribution as mentioned above.

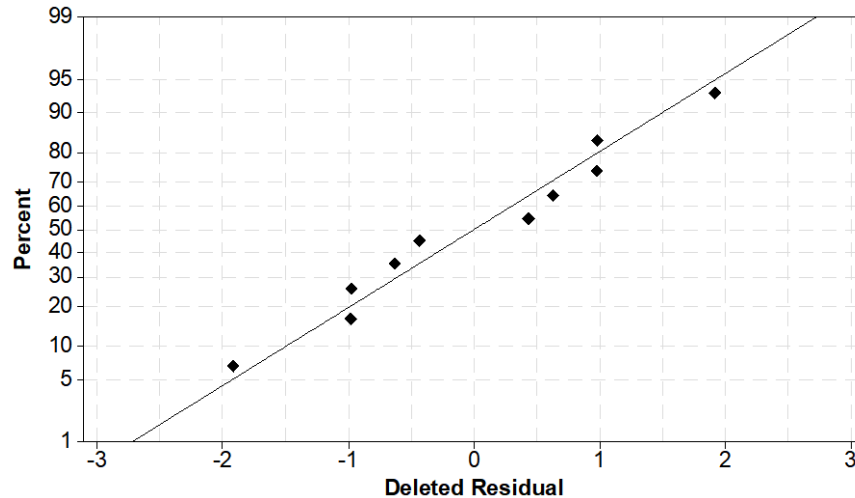


Figure 4.6 Normal probability plot with Box Cox transformation of Ultimate tensile strength.

Figure 4.7 shows the deleted residuals versus the fitted values of the Ultimate tensile strength. Despite the funnel behavior that persists, a better dispersion of the data is observed. In conclusion, the data is heterogeneous, and not constant. This might be due to the small sample size or other factors not taken into account in the model. Further exploration is encouraged.

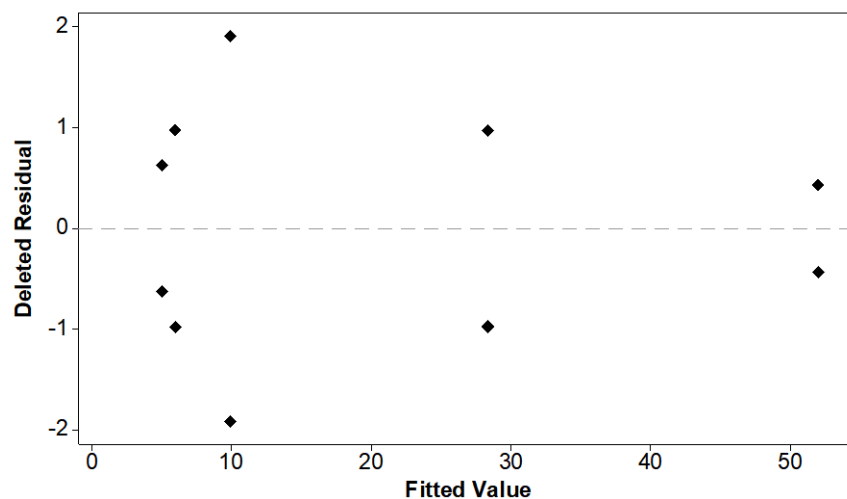


Figure 4.7 Deleted residuals versus fitted values with Box Cox transformation of the Ultimate tensile strength.

One can verify the assumption of independence between the residuals using the residuals versus order plot (Figure 4.8). Evidently, the residuals are randomly distributed around the center line, demonstrating that the residuals are not correlated with each other.

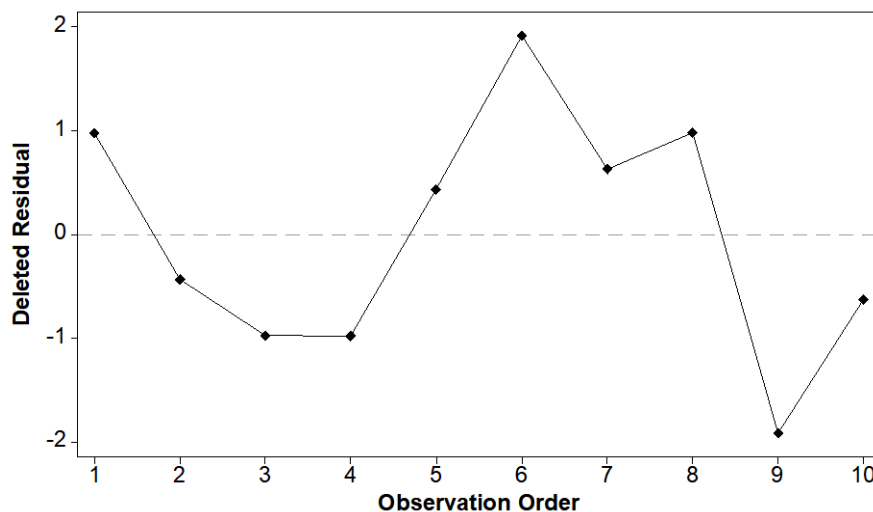


Figure 4.8 Deleted residuals versus order plot with Box Cox transformation of Ultimate tensile strength.

The analysis of variance is summarized in Table 4.2. The F-value statistics for the stirring speed is 4.06, which leads one to conclude that there is no evidence of iteration. Table 4.2 also shows that the effect of stirring time has an F-value of 9.35, being the most significant main effect. Moreover, the highest F-value was obtained by the interaction between stirring speed * stirring time, with a value of 49.06. This demonstrates that the main factors have a strong interaction between them. Having a meaningful interaction can hide the true significance of the main effects. Hence, we decided to examine the levels of each factor, keeping the levels of the others fixed, to draw conclusions about the stirring time as main effect.

Table 4.2 Analysis of variance for the transformed response Ultimate tensile strength

	DF	Adj SS	Adj MS	F-Value	p-Value
Model	4	3233.7	808.43	18.55	0.003
Linear	2	584.4	292.21	6.7	0.038
Stirring Speed	1	176.8	176.78	4.06	0.1
Stirring Time	1	407.6	407.65	9.35	0.028
2-Way Interactions	1	2138.3	2138.33	49.06	0.001
Stirring Speed*Stirring Time	1	2138.3	2138.33	49.06	0.001
Curvature	1	511	510.99	11.72	0.019
Error	5	217.9	43.59		
Total	9	3451.7			

The normal and Pareto plots helped us visualize the magnitude and the effect of each factor. In particular, the Pareto plot presents the absolute value of the effect and draws a reference line, any effect that exceeds this line was considered statistically significant. Figure 4.9 shows the Pareto chart of the standardized effects, and Figure 4.10 presents the normal plot of the standardized effects of stir casting.

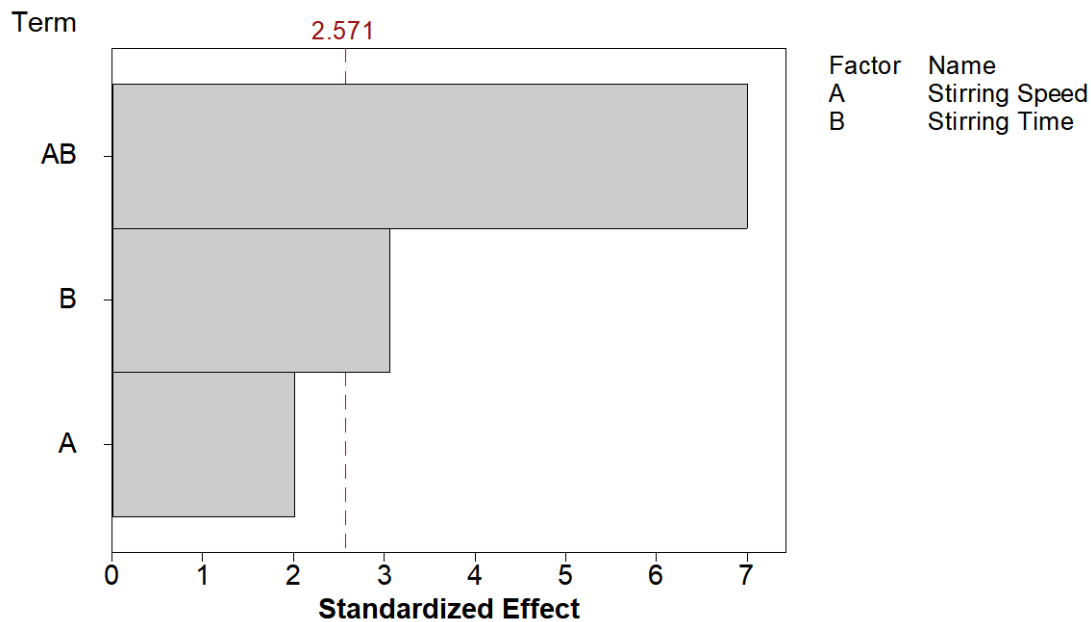


Figure 4.9 Pareto chart of the standardized effects of stir casting (response is the Ultimate tensile strength, $\alpha = 0.05$).

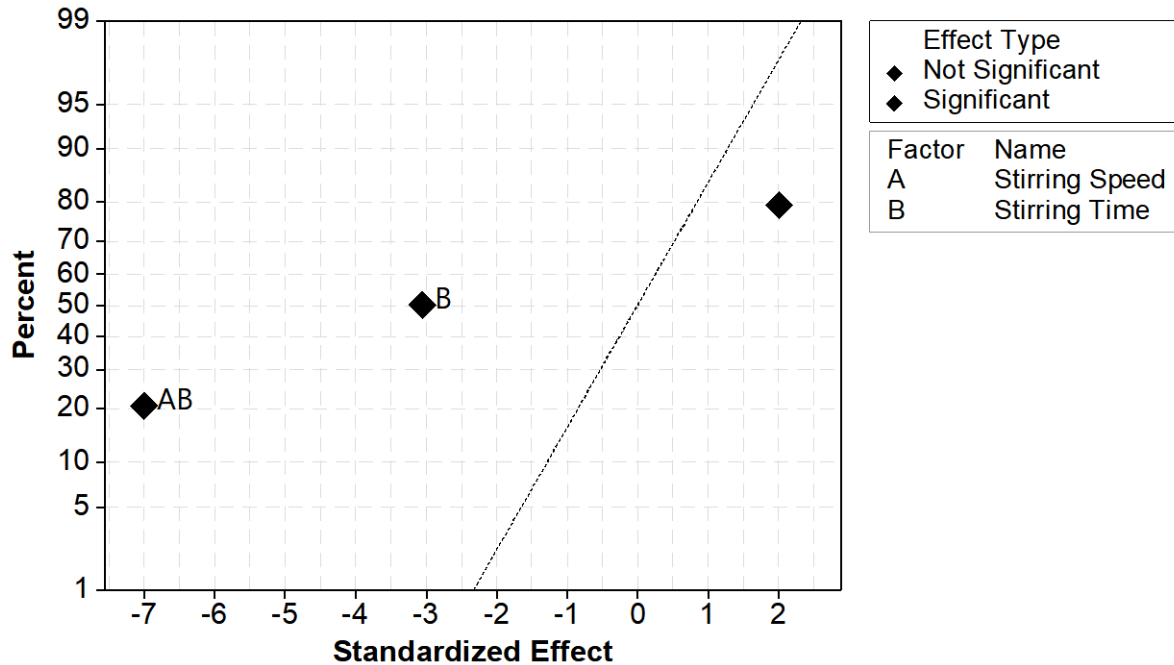


Figure 4.10 Normal plot of the standardized effects of stir casting (the response is the Ultimate tensile strength, $\alpha = 0.05$).

To better visualize the interaction between stirring speed * stirring time factor, the interaction plot for Ultimate tensile strength is shown in Figure 4.11. The greater the slope between the lines, the greater the degree of interaction. This graph indicates that faster and shorter higher UTS was observed. Interestingly, the central point is very close to the point of intersection of the slopes. This effect can be studied much better with a response surface.

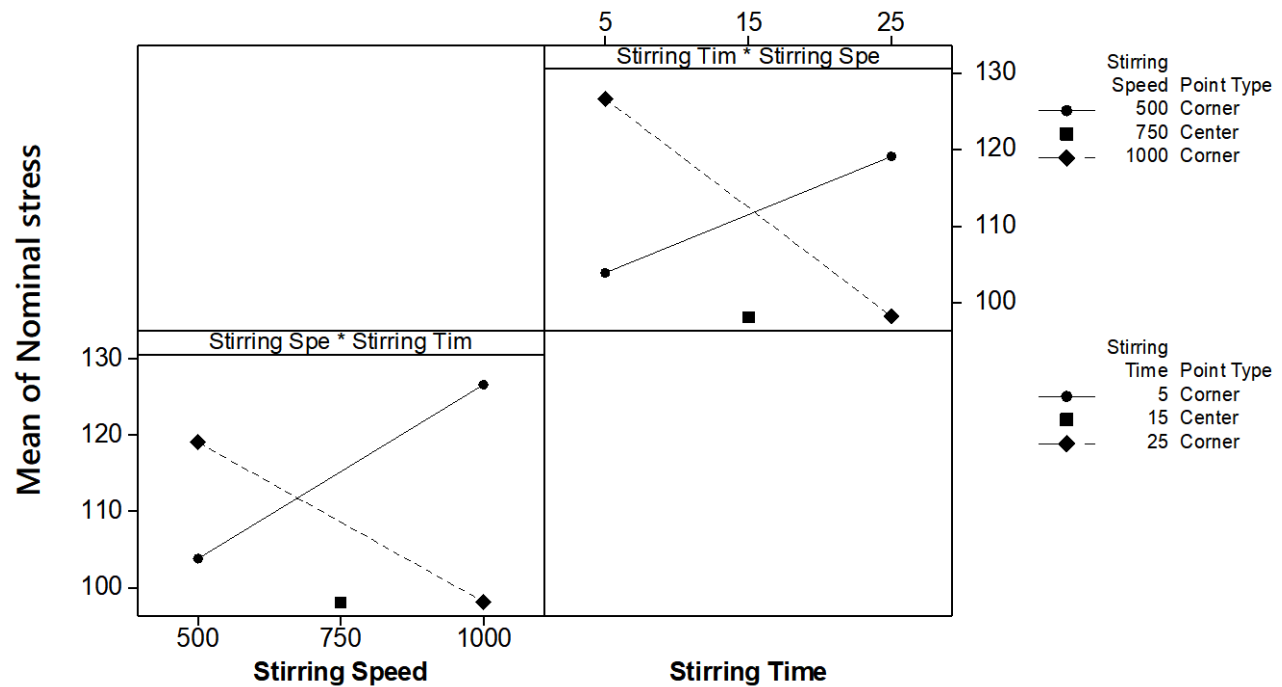


Figure 4.11 Interaction plot for Ultimate tensile strength (fitted means).

Table 4.3 shows the model summary for the transformed response variable. This table presents how well the data fitted our regression model, which is able to predict 74.74% of the new observations. Table 4.4 shows the coefficients of the model. Each effect is estimated independently, as an assumption of orthogonality. The Variance inflation factor (VIF) effects and interaction is 1, which indicates that the predictors were not correlated.

Table 4.3 Model Summary for Transformed Response Ultimate tensile strength.

S	R-sq	R-sq(adj)	R-sq(pred)
6.60218	93.69%	88.63%	74.74%

Table 4.4 Coded Coefficients for Transformed Response Ultimate tensile strength.

Term	Effect	Coef	SE Coef	T-Value	P-Value	VIF
Constant		23.84	2.33	10.21	0	
Stirring Speed	9.4	4.7	2.33	2.01	0.1	1
Stirring Time	-14.28	-7.14	2.33	-3.06	0.028	1
Stirring Speed*Stirring Time	-32.7	-16.35	2.33	-7	0.001	1
Ct Pt		-17.87	5.22	-3.42	0.019	1

Using the regression equation for Ultimate tensile strength, one can build a response surface to predict a response at intermediate levels of the factors. Figure 4.12 shows the two-dimensional contour plot of the surface of nominal stress. This graph indicates that near 1,000 rpm of stirring speed and a stirring time of 5 s, our material reached the highest UTS.

$$\text{Regression Equation of Ultimate tensile strength} = -53.1 + 0.1169 \text{ Stirring Speed} \\ + 4.191 \text{ Stirring Time} - 0.006540 \text{ Stirring Speed} * \text{Stirring Time} - 17.87 \text{ Ct Pt (eq. 02)}$$

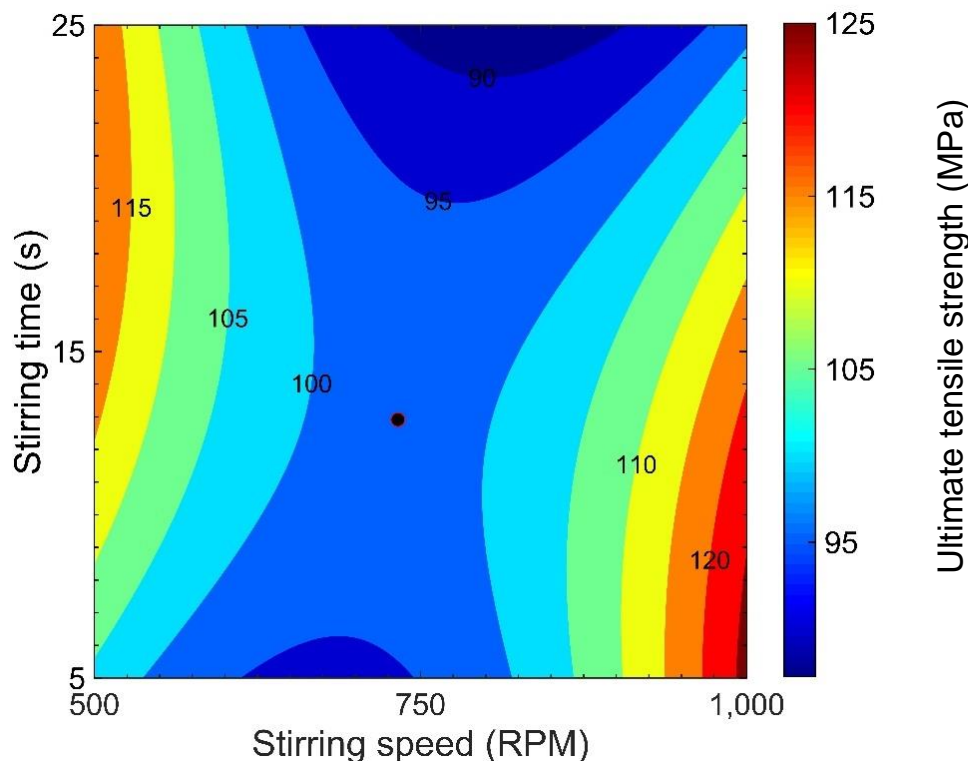


Figure 4.12 Two-dimensional contour plot of the surface of Ultimate tensile strength.

The curvature is also better appreciated in Figure 4.13, where the response surface of the UTS is shown. In this graph, we can see that the response displays concentric ellipses in the Minimax system. In the center of the system, the stationary point allowed calculating the saddle point, as 12.92 s of stirring time and 732.71 RPM stirring speed for a 98.35 MPa strength.

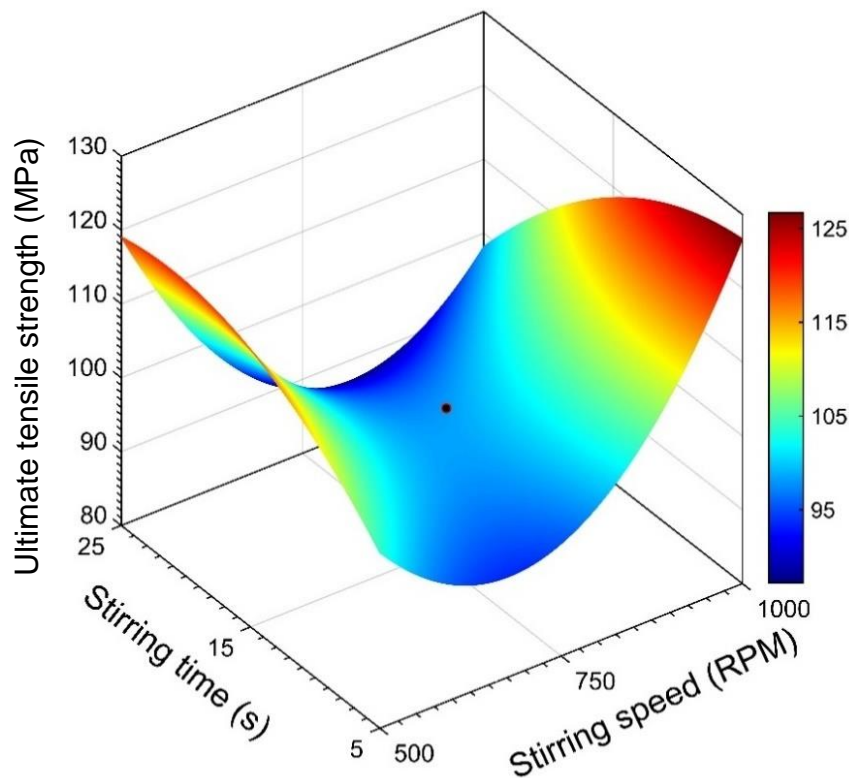


Figure 4.13 Response surface of the Ultimate tensile strength.

The Minitab 17 response optimizer tool permitted to calculate the different experimental configurations that affect the predictive response variable, and to obtain an optimal response variable. Our objective was to maximize the ultimate tensile stress of the stir casting process for the filler reinforced with NbB_2 nanoparticles. For the analysis, we gave

the same weight and importance to both factors. The parameters to calculate the optimal are summarized in Table 4.5. After calculating the optimal multiple response prediction, shown in Table 4.6, optimal levels to achieve maximum UTS were 1000 RPM of stirring speed and stirring time of 5 seconds, with a UTS of 126.67 MPa. The standard error of the fits (SE fits) was 7.01 and this was used to generate the confidence interval (CI) for the prediction; for a 95%, CI was (108.64, 144.69) MPa. We also used the composite desirability to assess how well a combination of input variables fitted the optimal response. Our optimal one has a favorable desirability of 0.986. The scale of the composite desirability is in a range of zero and one, where zero indicates that some of the responses are outside the acceptable limits, and one represents the ideal case.

Table 4.5 Parameters to calculate the optimal of Ultimate tensile strength (MPa).

Response	Goal	Lower	Target	Upper	Weight	Importance
Ultimate tensile strength	Maximum	88.0238	127.207		1	1

Table 4.6 Optimal Response Prediction of Ultimate tensile strength.

Solution	Stirring Speed (RPM)	Stirring Time (s)	Ultimate tensile strength Fit (MPa)	Composite Desirability
1	1000	5	126.667	0.986213

4.1.3 Conclusions

Thus far, we have presented the effect of the most important factors of the stir casting process. We discovered that the stirring speed * stirring time interaction was the most significant, and the mixing time was the main factor. The Minitab analysis indicated that to maximize the UTS, the settings to reach 126.7 MPa were a stirring speed of 1,000 RPM and a 5 s of stirring time.

The response surface analysis identified that the response displays concentric ellipses in a Minimax system. For this system, the saddle point was calculated at 12.2 s of stirring time and a stirring speed of 710 RPM for a 101.2 MPa strength level. The location of this point is important to understand the nature of the system and to calculate the minimum response that satisfies all maximal responses.

During this experiment, we fixed the amount of NbB₂ nanoparticles at 1% wt. Changing the percentages of nanoparticles during the stir casting process can help optimize our process. It is important to remember that in working with non-constant variance and heterogeneous data some important variables could have been omitted. In the next chapter, we present a central composite design by adding different amounts of nanoparticles and exploring new levels of the factors studied.

4.2 Filler Optimization: Central Composite Experiment of Stir Casting

In stir casting we selected to analyze the casting factors in order to reduce the variability of the process. Previously, a full factorial experiment allowed assessing the effect of those casting factors, namely melt stirrer speed and stirring time, as detailed in section 4.1. This analysis helped to define the levels of a central composite design and to estimate a second-degree polynomial model, which enabled the optimization of the manufacturing process.

The filler was prepared with different weight percentages of nanoparticles and with an Al - 5 wt.% Mg binary alloy. This level of magnesium was added to strengthen the filler and make it comparable to the AA 5356 commercial filler, where Mg is the main alloying element. Filler rods with 2.4 mm in diameter were obtained via rolling, and tested using TIG welding. In this chapter, we also analyzed weld hardness and weld porosity. The methodology of the experiment design and the ensuing manufacturing is discussed in the next section.

4.2.1 Methodology

Design of Experiment (Central Composite)

In our research, being able to implement the axial executions would allow adding the quadratic terms into the model to help us build second-order response surface models. In our case, the CCD is a 3^2 factorial, with 2 replicates in the factorial, six axials, and four center points. The practical deployment of a CCD often arises through sequential experimentation. However, in this investigation, there were several previous and subsequent processes that affected the variability of filler manufacturing. Hence, central and axial points were added to analyze the response surface. Figure 4.14 shows the central composite design studied. The factors are the amount (percent) of nanoparticles, stirring speed, and stirring time. Each factor was evaluated at two levels. Table 4.7 shows the factors and their respective levels for the experiment. The central composite design matrix obtained from Minitab is presented in Appendix B.2.

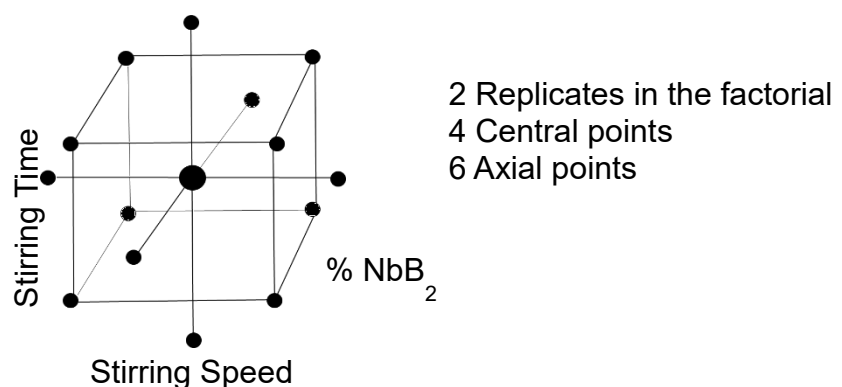


Figure 4.14 Central composite design for the stir casting components.




Table 4.7 Central Composite parameter for the stir casting components.

Parameter	Units	Lower	Higher
NbB ₂	wt. %	0.5	1.5
Stirring time	Sec	20	40
Stirring speed	RPM	300	600





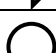



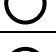
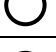







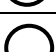


Experimental Conditions

A total of 26 runs were completed with the order of the runs was randomly assigned by Minitab 17. All experiments were carried out in one day. Thus, the laboratory's humidity and temperature conditions were controlled with air conditioning at 20 °C and 50% humidity. A total of 4 people participated in the experiment and each of them performed specific tasks. The casting process diagram for the production of one ingot is included in Table 4.8. The time registered for each manufacturing process was 116.7 minutes, during normal conditions. The biggest challenge while conducting this experimental design was the number of samples required, i.e. 26 runs, which had to be made through a continuous manufacturing process under identical conditions.

Table 4.8 Stir Casting process diagram.

Symbol	Name	Description
	Operation	Add Value
	Transport	Material movement
	Delay	Temporary Delay/Hold

Time (minute)	Symbol	Description	Operator
2	○	Setting the furnace	1
2	○	Setting up electric melter 1	1
2	○	Setting up electric melter 2	1
20	D	Wait until desired temperatures are reached	
3	○	Al - Mg are weighed	2
3	○	Pellets with nanoparticles are weighed	2
	➡	Al - Mg is transferred to the casting area	2
2	○	Stirrer is cleaned with a wire brush	3
4	○	Mold is cleaned with a wire brush	3
1	○	Stirrer is painted with graphite	3
1	○	Mold is painted with graphite	3
5	D	Wait until the paint dries	
2	○	Adapt the stirrer to the motor	1
	➡	Move the Stirrer to the electric melter 2	1
1	○	The stirrer is placed inside the electric melter 2	1
2	○	Set the stirrer speed	1
10	D	Wait for the stirrer to reach the temperature	
	➡	Move the mold to the furnace	3
1	○	The mold is put inside the furnace	3
10	D	Wait for the mold to reach the temperature	

Time (minute)	Symbol	Description	Operator
0.5		Al - Mg are placed on the electric melter 1	4
5		Wait for the Al-Mg to melt	
		Transfer the pellets to the casting area	2
		Transfer the stirrer to the electric melter 1	4
1		Insert the stirrer into the electric melter 1	4
1		Enter the pellets into the electric melter 1	4
0.2		Wait for pellets to mix with Al-Mg	
0.5		Remove stirrer from the electric melter 1	1
1		Remove mold from furnace	3
0.5		Casting	4
1		Wait for solidifying the compound	
2		Open the mold	2
2		Remove ingots	3
		Transfer the ingots to the cleaning area	2
10		Wait for the ingots to cool	
10		Clean the ingots of burrs (deburring)	2
1		Pack the ingots with Silica gel	2
		Transport ingots to the desiccator	1
10		Wait for the stirrer and mold to cool	
		Move stirrer and mold to the cleaning area	3
116.7	Total time of production of one ingot		

In addition, for the sake of characterization, we required a minimum of 3 fillers for each experimental condition. Due to these restrictions, a new mold was designed and manufactured. This mold allowed fabricating three ingots simultaneously, which permitted a proper filling of the area to be welded for hardness testing and porosity measurement, as indicated in Figure 4.15.

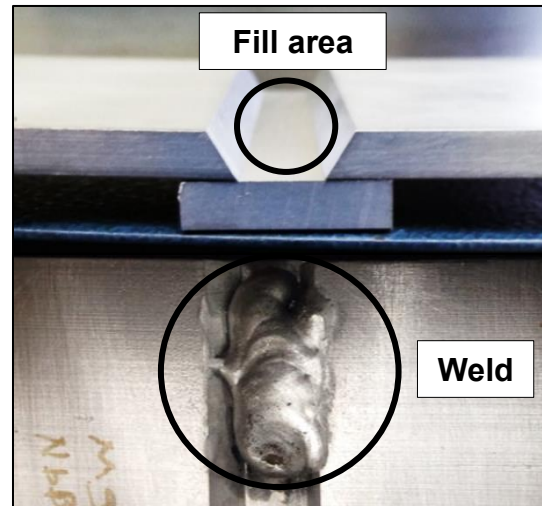


Figure 4.15 Area to be filled with the welded filler material.

In designing this mold, different factors were considered: the pouring temperature of the metal to be casted, size of the casting, number of castings per mold, and cost of the mold material. Gray iron, a ferrous alloy commonly used for its low cost and good machinability, was employed for the manufacture of this permanent mold. In effect, gray iron molds, which show good wear resistance, have the capacity to make a long series of aluminum and magnesium castings that will then be machined, and from which, more than 100,000 discharges are obtained [32]. Figure 4.16 shows the design and photo of the mold with three cast ingots, while Figure 4.17 includes a schematic of the mold.

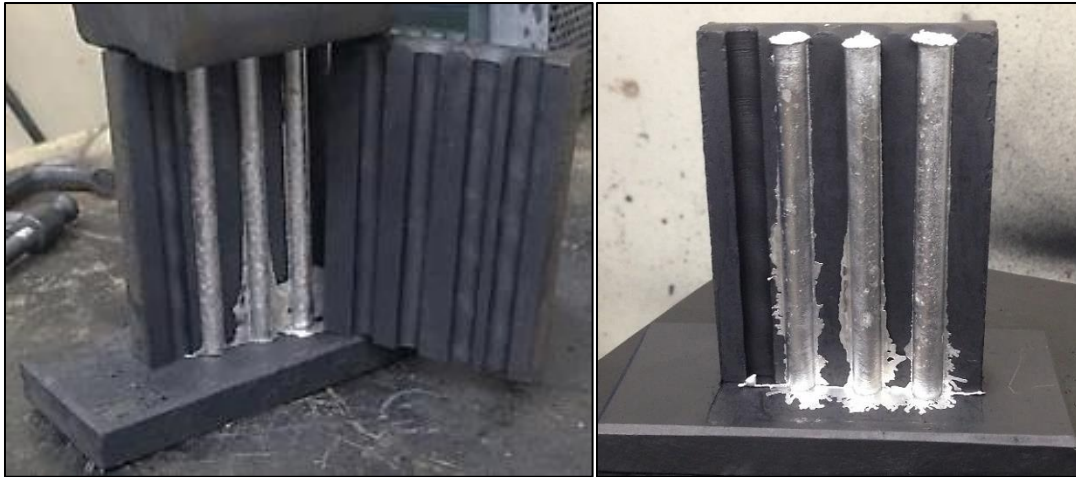


Figure 4.16 Photos of mold with three cast ingots.

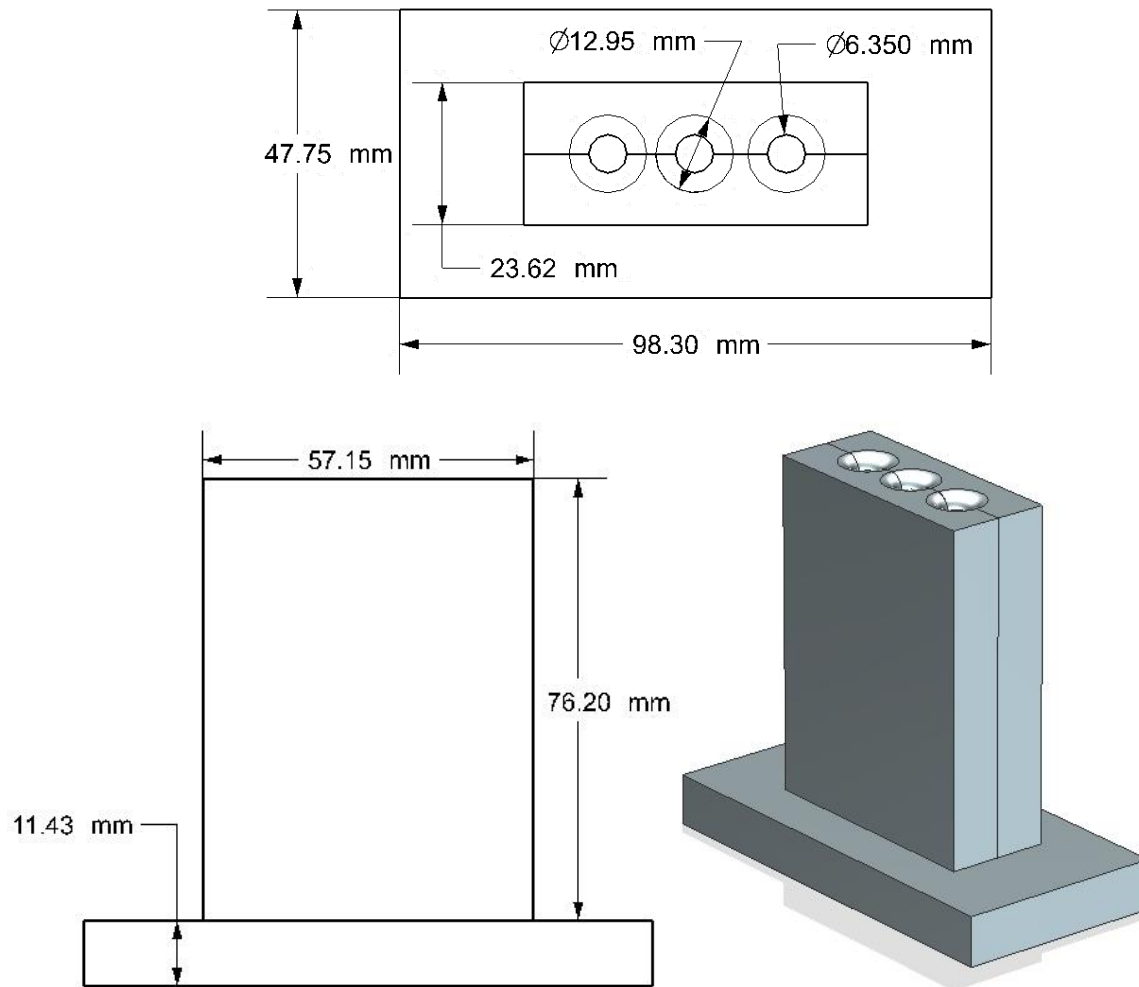


Figure 4.17 Mold schematic and 3D model.

The method used to produce the ingots was gravity casting, which is done by pouring the molten metal into the mold, allowing it to flow by its own weight. A pouring basin made of gray iron assured that the weight be sufficient to fill the three chambers of the mold as the molten metal was evenly distributed. Figure 4.18 depicts a 3D model of the said basin.

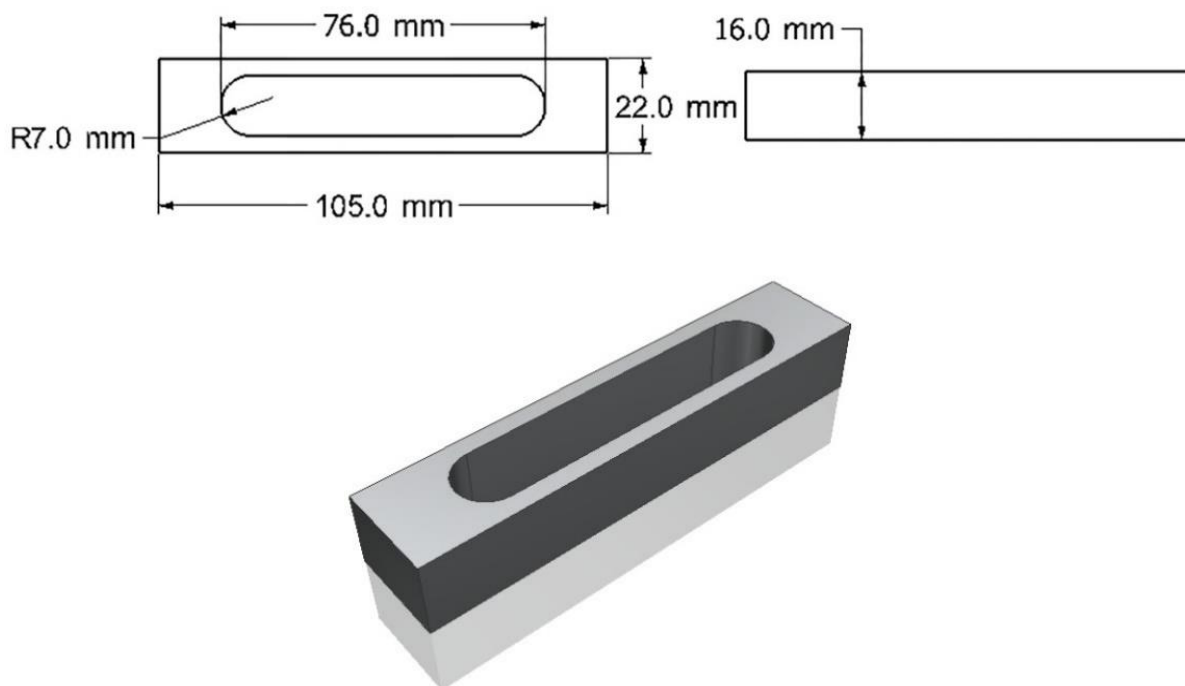


Figure 4.18 Pouring basin schematic and 3D model.

All preparations intended to properly execute the experimental design, i.e. a central composite one, included some practices to help reduce the process variability. The next section presents the manufacturing process of the Al-NbB₂ nanocomposite pellets. It also includes the procedure to welding, and characterizing the samples.

Manufacturing Process

Our first step was the preparation of the NbB₂ Nanoparticles. To this purpose, a varioplanetary ball mill (Pulverisette 4, manufactured by Fritsch GmbH, Idar-Oberstein, Germany) allowed fragmenting the as-received NbB₂ particles (Alfa Aesar, Ward Hill, Massachusetts, USA) to attain nanostructure size. Ball-to-powder ratio (BPR) weight and rotational speed were two controlled parameters that dictate particle size in ball milling processes [39]. Smaller NbB₂ size particles were present when BPR and rotational speed increased, shortening milling times [9].

In contrast, we needed longer times and lower speeds to effectively fragment the NbB₂ particles. Hence, the ball mill rotational speed was set at 800 rpm for 20 hours. After ball milling, the NbB₂ particles were studied using a Siemens® D500 (Princeton, NJ, USA) x-ray diffractometer with Cu K α radiation ($\lambda = 0.154178$ nm). Figure 4.19 displays the x-ray powder diffraction graph of the NbB₂ without ball milling and of NbB₂ particles after 20 milling hours. Using Scherrer's equation [36], the calculated crystallite size of the NbB₂ nanoparticles was found to be 15 nm.

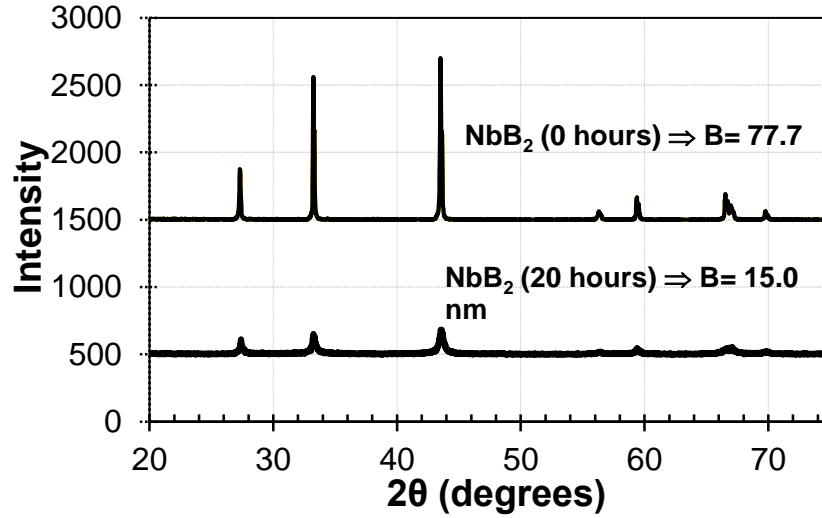


Figure 4.19 XRD pattern of NbB₂: as-received (without ball milling, upper spectrum), and NbB₂ particles after 20 hours of milling (lower spectrum).

As mentioned in section 3.1.1.2, the manufacture of the Al-NbB₂ pellets was performed by mechanical alloying (cold welding). The grinding took 20hr and the results are shown in Appendix B.3. This procedure also favored the breakup of the agglomeration of NbB₂ nanoparticles after milling to achieve uniform reinforcement distribution.

The second step was the stir casting, where the experimental filler material was fabricated with an Al-Mg (5 wt.% Mg) master alloy. Moreover, as mentioned above, the central composite design for the stir casting process allowed estimating a second-degree polynomial model for the manufacturing process optimization. The experimental conditions applied in this central composite were explained at the beginning of this section. The stirring speeds and stirring times were set according to the levels and run order. Next, the stir casting process for the manufacture of the nanocomposite will be discussed.

In a graphite crucible, we melted pure aluminum along with the Al-Mg master alloy at 700 °C. We inoculated the melt with the Al-NbB₂ pellets and mechanically stirred the molten material to improve the particle distribution. The treated melt was then poured into a cylindrical mold to produce 6-mm-diameter ingots.

Finally, the said quality tests were performed to measure the parameters being studied. Figure 4.20 shows the steps to perform these quality tests. According to the AWS 5 -10 standard, the filler should have a 2.4 mm diameter, which we obtained by cold rolling.

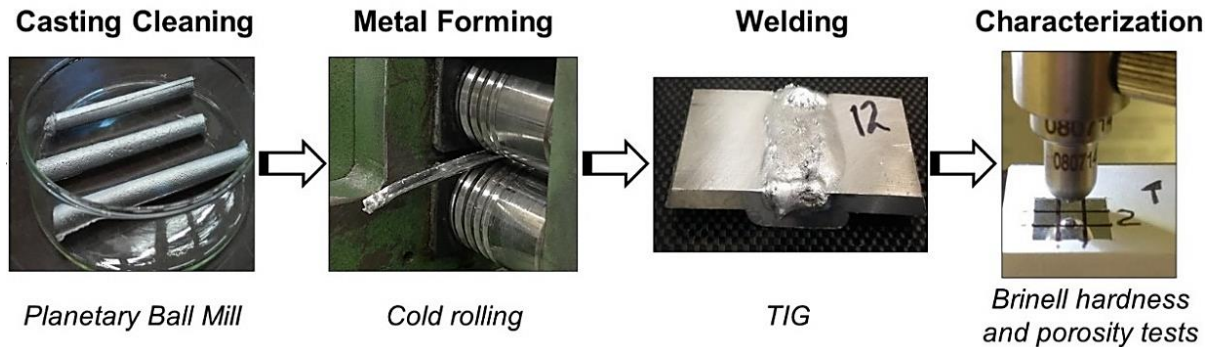


Figure 4.20 Steps to perform the quality test.

Before welding, the samples were cleaned with a steel wire brush and rinsed with acetone to remove the oxide layer. As described previously, they were then TIG welded, with the parameters controlled by the TIG welding machine (Lincoln Electric Precision TIG 225 230V AC/DC TIG). After welding, the excess material was cut off the test specimen. These cut pieces were then polished to perform Brinell hardness and to measure porosity.

4.2.2 Results and Discussions

Central Composite Design Analysis: Brinell Hardness

The probability plot of the Brinell hardness helped analyze the normal distribution of the data (Figure 4.21). The resulting p-value, i.e. 0.073, is greater than 0.05, which is not enough evidence to conclude that the results do not follow a normal distribution. The normal probability plot reveals nothing particularly problematic, although there are two outliers at the end of the tails. The results are presented in Appendix B.2 together with the central composite design matrix of Brinell hardness.

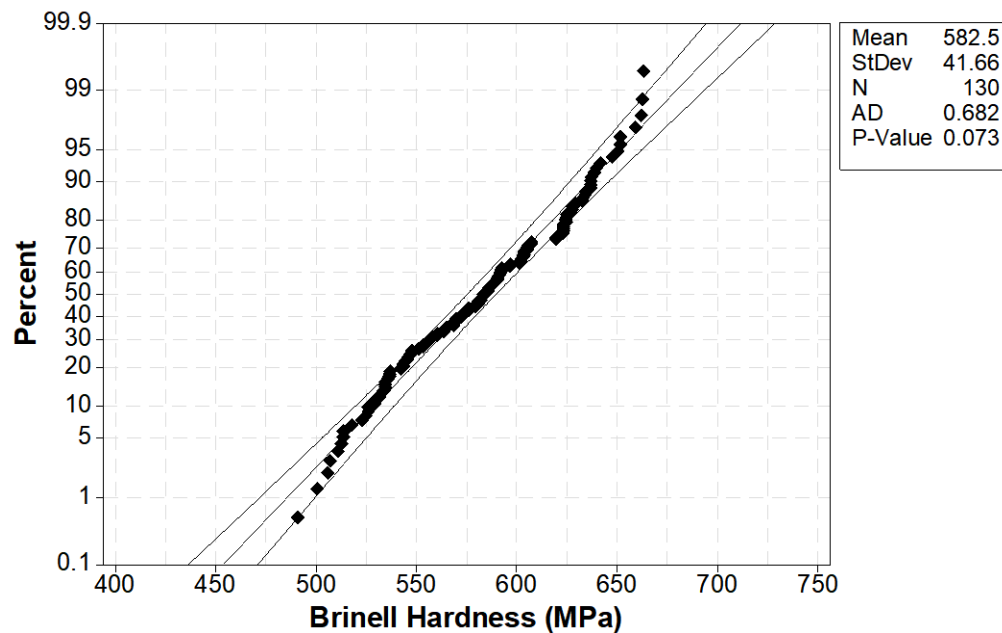


Figure 4.21 Box-Cox of normal probability plot of the Brinell hardness (MPa), (95% CI).

As mentioned, a Box-Cox transformation allowed correcting the bias in the distribution of errors and the unequal variance by obtaining a λ of 0.5. Figure 4.22 shows the deleted residuals versus the fitted values of the Brinell hardness. The deleted residuals were used as an alternative to identify outliers.

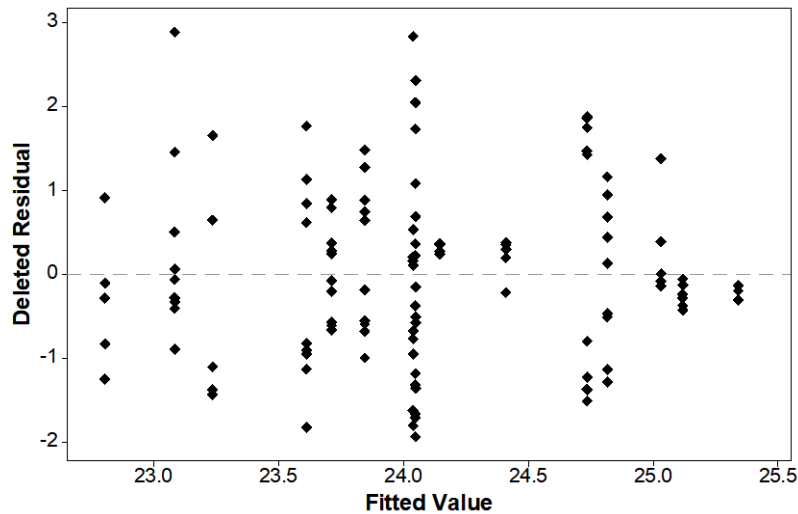


Figure 4.22 Box-Cox of deleted residuals versus fitted values of the Brinell hardness (MPa).

The graph of the deleted residuals versus order plot of the Brinell hardness (Figure 4.23) shows some correlation between the error terms that are near each other in the order in which the data were collected. Clearly, the residuals are randomly distributed around the center line; hence, the assumption of independence error terms has not been violated.

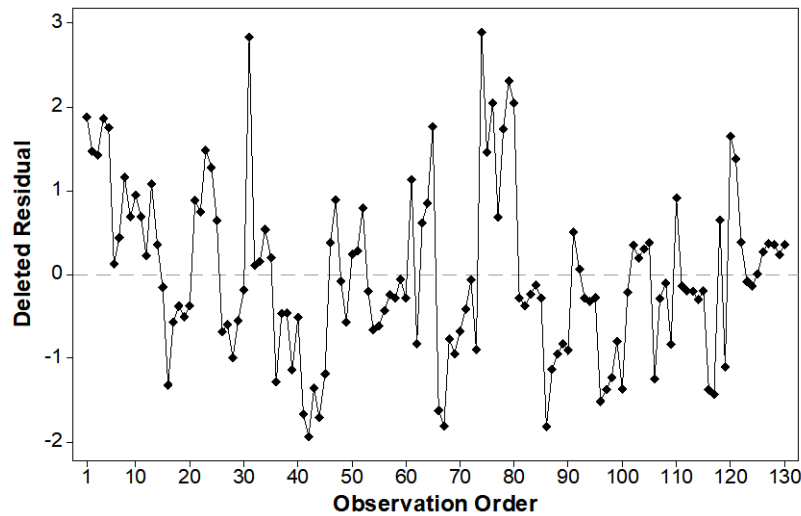


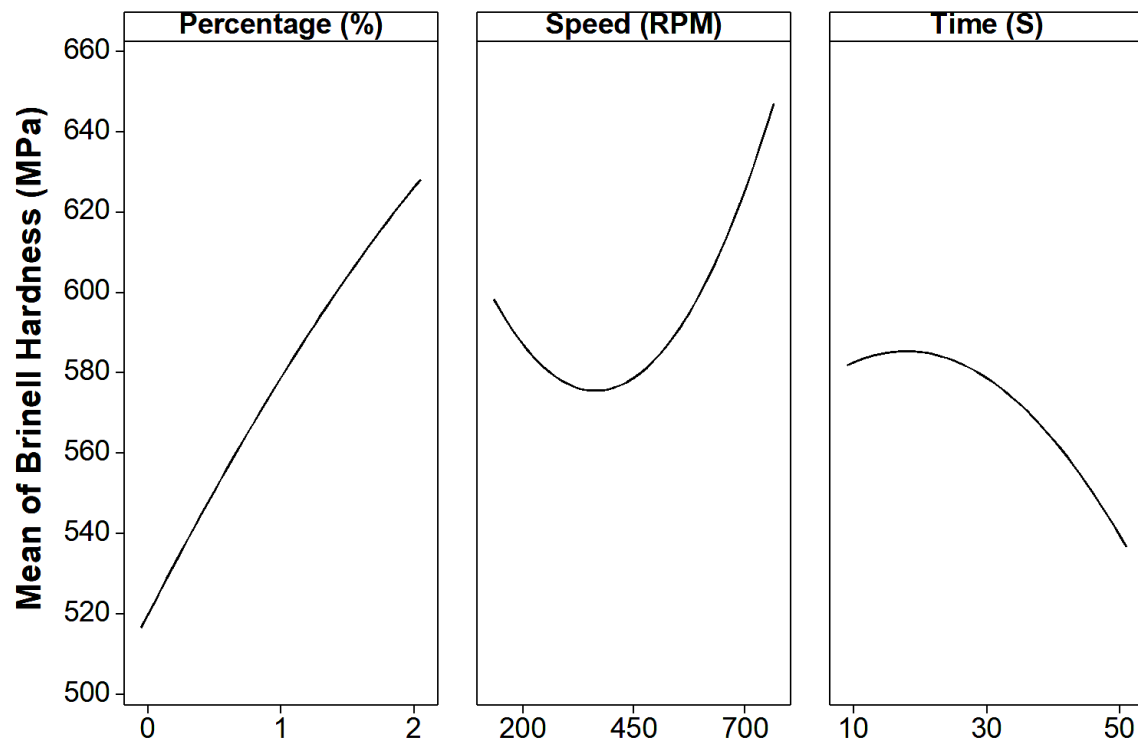
Figure 4.23 Box Cox of deleted residuals versus order plot of the Brinell hardness (MPa).

The ANOVA in Table 4.9 reveals that the percentage of nanoparticles, with an F-value of 117.8 ($p < .001$), is the most significant factor in filler production and hardness. Moreover, the stirring speed showed an F-value of 20.56 ($p < .001$), while the stirring time, an F-value of 19.67. These results suggest that the two factors do not influence the hardness as much, but they do affect the reinforcement distribution and the weld quality.

Table 4.9 Analysis of Variance for Transformed Response.

	DF	Adj SS	Adj MS	F-Value	P-Value
Model	10	58.993	5.8993	18.71	0
Blocks	1	0.0051	0.0051	0.02	0.899
Linear	3	49.826	16.6086	52.67	0
Percentage (%)	1	37.142	37.1415	117.8	0
Speed (RPM)	1	6.4812	6.4812	20.56	0
Time (S)	1	6.2031	6.2031	19.67	0
Square	3	7.98	2.66	8.44	0
Percentage (%)*Percentage (%)	1	0.1219	0.1219	0.39	0.535
Speed (RPM)*Speed (RPM)	1	3.6803	3.6803	11.67	0.001

Time (S)*Time (S)	1	0.7939	0.7939	2.52	0.115
2-Way Interaction	3	1.1158	0.3719	1.18	0.321
Percentage (%)*Speed (RPM)	1	0.0228	0.0228	0.07	0.788
Percentage (%)*Time (S)	1	0.3162	0.3162	1	0.319
Speed (RPM)*Time (S)	1	0.7769	0.7769	2.46	0.119
Error	119	37.521	0.3153		
Lack-of-Fit	4	1.5529	0.3882	1.24	0.297
Pure Error	115	35.968	0.3128		
Total	129	96.515			



All displayed terms are in the model.

Figure 4.24 Main effects plot of the Brinell hardness.

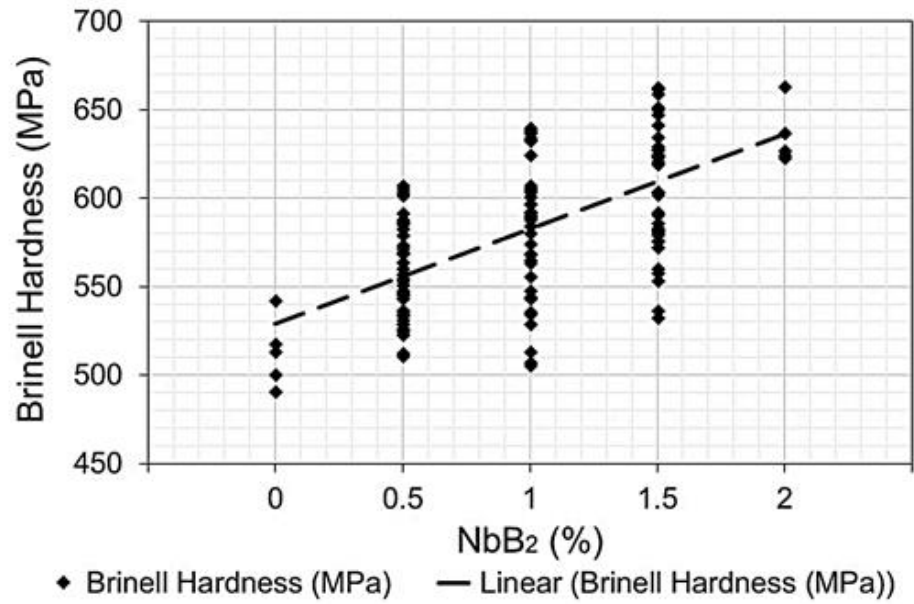


Figure 4.25 Individual value plot of the Brinell hardness as a function of the NbB₂ percent using lineal regression.

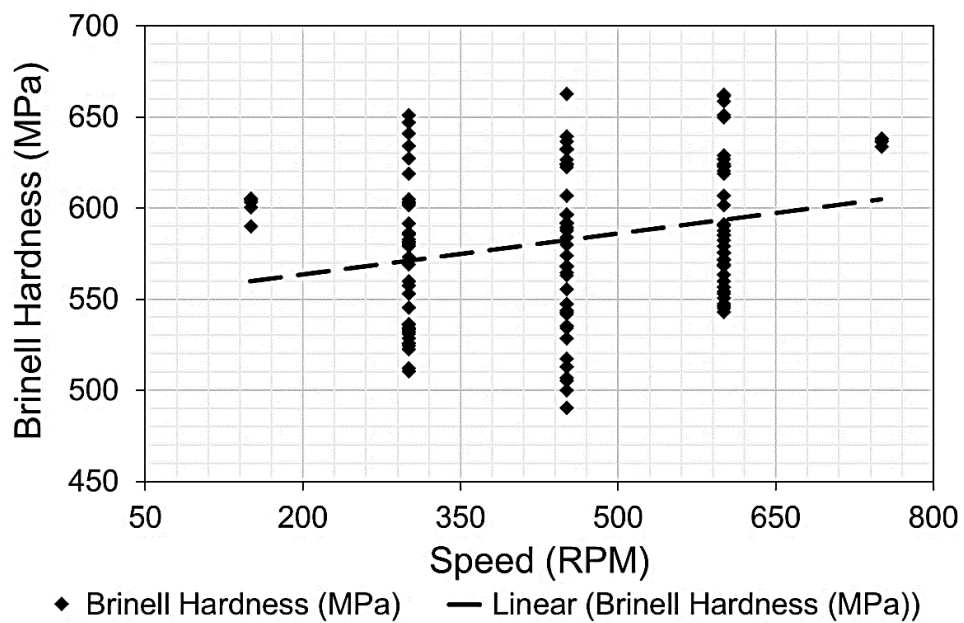


Figure 4.26 Individual value plot of the Brinell hardness as a function of the stirring speed with lineal regression.

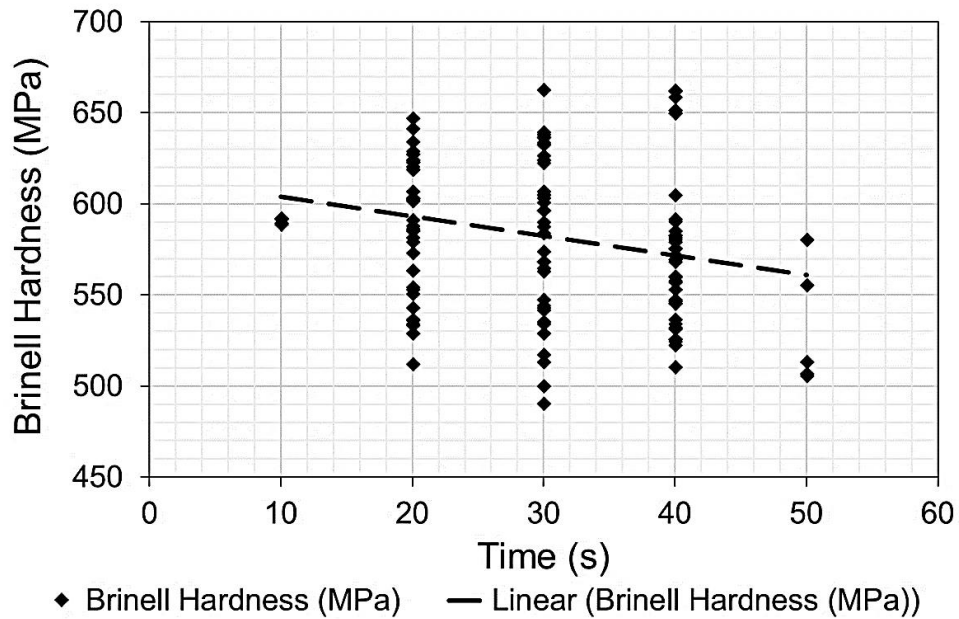


Figure 4.27 Individual value plot of the Brinell hardness as a function of the stirring time using lineal regression.

Table 4.10 shows the model summary for the transformed response variable of the Brinell hardness. This table presents how well the data fitted the regression model, which is able to predict 54.52% of the new observations. Table 4.11 shows the model coefficients. The variance inflation factor (VIF) of the main effects is 1, which indicates that the predictors were not correlated.

Table 4.10 Model Summary for Transformed Response Brinell hardness.

S	R-sq	R-sq(adj)	R-sq(pred)
0.56152	61.12%	57.86%	54.52%

Table 4.11 Coded Coefficients for Transformed Response Brinell hardness.

Term	Effect	Coef	SE Coef	T-Value	P-Value	VIF
Constant		24.06	0.161	149.67	0	
Blocks 1		-0.01	0.0694	-0.13	0.899	1.41
Percentage (%)	1.1127	0.556	0.0513	10.85	0	1
Speed (RPM)	0.4648	0.232	0.0513	4.53	0	1
Time (S)	-0.455	-0.23	0.0513	-4.44	0	1
Percentage (%)*Percentage (%)	-0.074	-0.04	0.0592	-0.62	0.535	1.44
Speed (RPM)*Speed (RPM)	0.4044	0.202	0.0592	3.42	0.001	1.44
Time (S)*Time (S)	-0.188	-0.09	0.0592	-1.59	0.115	1.44
Percentage (%)*Speed (RPM)	0.0338	0.017	0.0628	0.27	0.788	1
Percentage (%)*Time (S)	-0.126	-0.06	0.0628	-1	0.319	1
Speed (RPM)*Time (S)	0.1971	0.099	0.0628	1.57	0.119	1

At this point, one must keep in mind that the goal has been to determine the optimal operating conditions in the stir casting process to manufacture the filling material reinforced with NbB₂ nanoparticles. Within this framework, the response surface method is a sequential procedure. For this reason, in section 4.1, the full factorial experiment helped explore the levels of the two most important factors in stir casting. In conclusion, we discovered a strong interaction of factors, namely the stirring speed, and the stirring time, as well as the quadratic factors effect. For the second part, we decided to explore other levels of these factors, with longer stirring times and stirring speeds below 750 RPM, and selected a more elaborate second-order model to locate the optimum. The best way to represent the relationship between the three independent variables and the response is via a regression model. Using the regression equation for the Brinell hardness (eq. 03) we can find the levels of the factors that maximize the performance of the stir casting process. The regression equation for the Brinell hardness can help build a response surface able to predict the response at the factors intermediate levels. Figure 4.28 shows the contour plot generated by the Brinell hardness predictive equation, comparing the

stirring speed factor against the nanoparticles percent. This graph illustrates that for higher speeds and more nanoparticles, the material could reach higher hardness, which is obtained at 750 rpm and 2% nanoparticles.

$$\begin{aligned}
 \text{Regression Equation of Brinell Hardness (MPa)}^0.5 = & 24.37 + 1.683 \text{ Percentage (\%)} \\
 & - 0.00874 \text{ Speed (RPM)} + 0.0166 \text{ Time (S)} - 0.147 \text{ Percentage (\%)} * \text{Percentage (\%)} \\
 & + 0.000009 \text{ Speed (RPM)} * \text{Speed (RPM)} - 0.000939 \text{ Time (S)} * \text{Time (S)} \\
 & + 0.000225 \text{ Percentage (\%)} * \text{Speed (RPM)} - 0.0126 \text{ Percentage (\%)} * \text{Time (S)} \\
 & + 0.000066 \text{ Speed (RPM)} * \text{Time (S)} \quad (\text{eq. 03})
 \end{aligned}$$

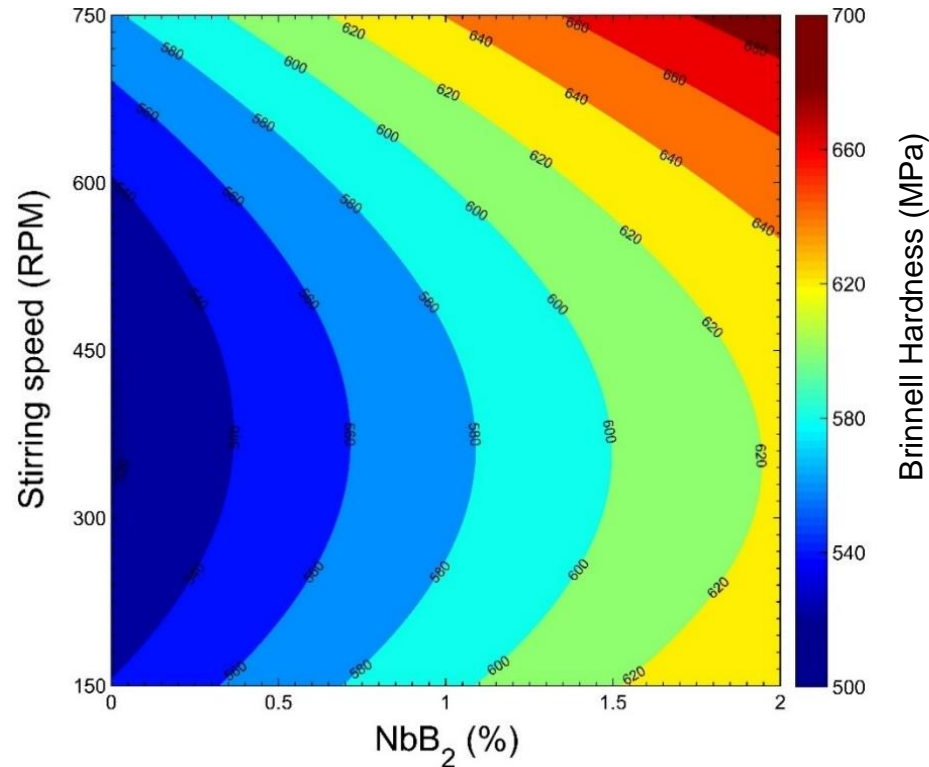


Figure 4.28 Contour plot of the Brinell hardness as a function of the stirring speed and NbB₂ percent.

Mohammad in 2015 observed a similar behavior, that the incorporation of B_4C particles in stirring speeds of 700 RPM, and also when the reinforcement percent rose, the composite microstructure improved [40]. The response surface graph in Figure 4.29 offers an alternative viewpoint to appreciate better the combined effect of these two factors. Even though it provides the same information as a 2D plot, the curvature in the stirring speed is much more apparent.

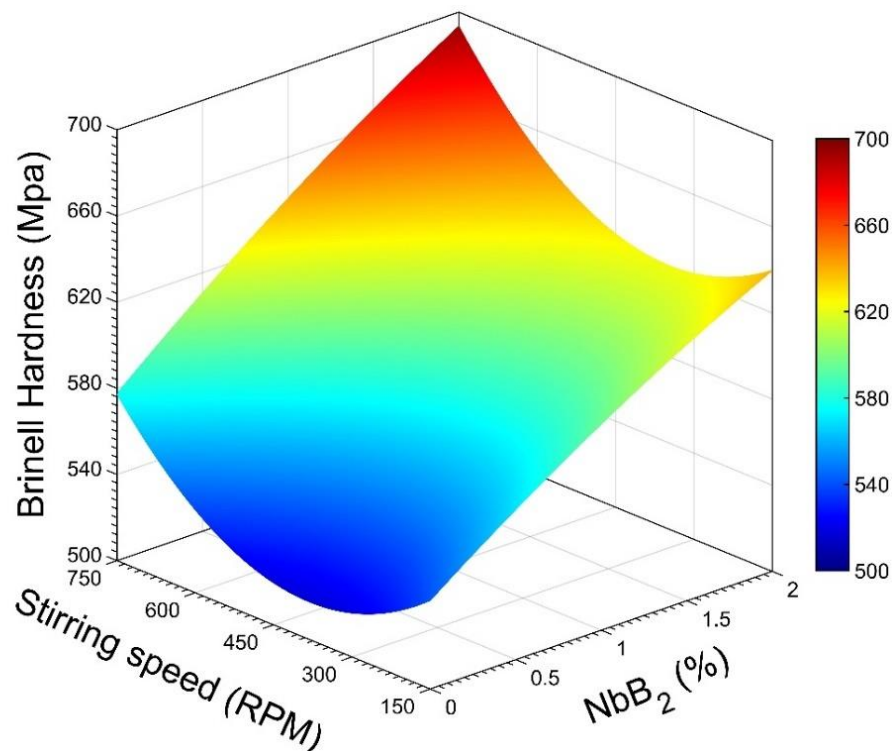


Figure 4.29 Response surface of the Brinell hardness as a function of the stirring speed and NbB_2 percent.

Figure 4.30 is a contour plot of the Brinell hardness surface that reveals that with a stirring time between 10 and 20 seconds and 2% percent of nanoparticles, the material could reach higher hardness. Li Yu in 2016 presented a study on the effect of titanium content and stirring time of Al- B_4C composite. In this work, greater tensile strength was obtained

with titanium levels of 3.5 wt% and shorter stirring time. On the other hand, with the same amount of titanium, lower tensile strength was obtained with prolonged stirring time [41]. This helps us understand the impact of stirring time in the manufacture of nanocomposites. Figure 4.31 shows the response surface of the Brinell hardness as a function of the stirring time and amount of nanoparticles. This graph clearly shows how hardness increases for higher NbB_2 amounts. This type of behavior was also observed in the work of Li Yu, where the hardness showed an inclined leaf-shape curve.

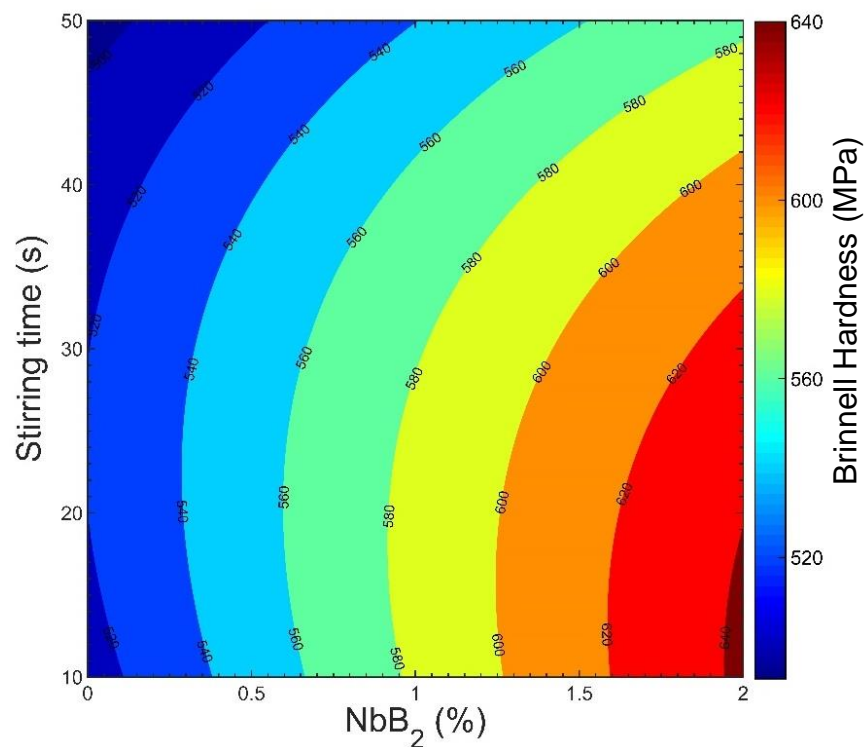


Figure 4.30 Contour plot of the Brinell hardness as a function of the stirring time and NbB_2 percent.

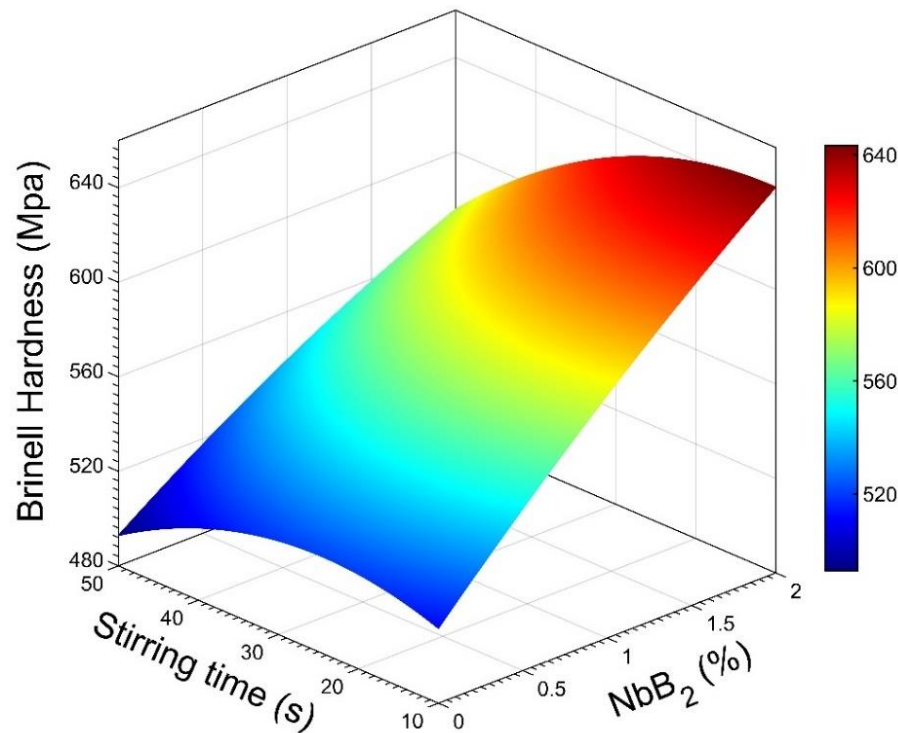


Figure 4.31 Response surface of the Brinell hardness as a function of the stirring time and NbB₂ percent.

Figure 4.32 shows the contour plot of the Brinell hardness as a function of the stirring time and speed. The graph shows the same behavior observed in the full factorial experiment in section 4.1. This system has the characteristic that by increasing or reducing both factors simultaneously, the response becomes smaller. However, when one factor rises and the other lowers, such combination leads to a larger response. For example, one can observe that between 10 and 20 seconds, at a speed of 750 rpm, a high hardness results. The response surface of the Brinell hardness as a function of the stirring time vs the Stirring speed graph in Figure 4.33 provides more information on how the weld hardness is affected by these two factors. This graph also indicates that the stirring time does not affect the hardness at speeds higher than 700 RPM.

S. Balasivanandha studied the influence of stirring speed and stirring time on the particles distribution in the stir casting process. The study revealed that these two factors have a significant effect on the production of metal matrix composites, and the higher speeds favors a more homogeneous distribution of the reinforcement [42]. Moreover, Figure 4.30 shows a different behavior at 150 RPM, because a small increase in hardness is observed. Yet, every time the stirring time increases at this speed, an aggressive decrease in the hardness is observed. This can be attributed to the low porosity level occurring at these speeds, as discussed in a later section.

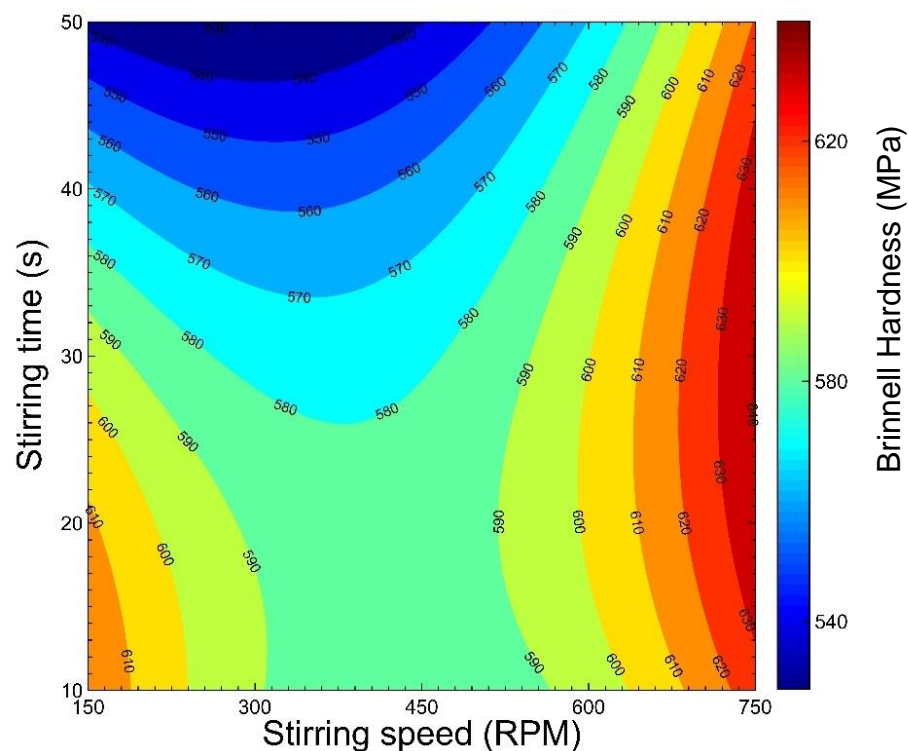


Figure 4.32 Contour plot of the Brinell hardness as a function of the stirring time and stirring speed.

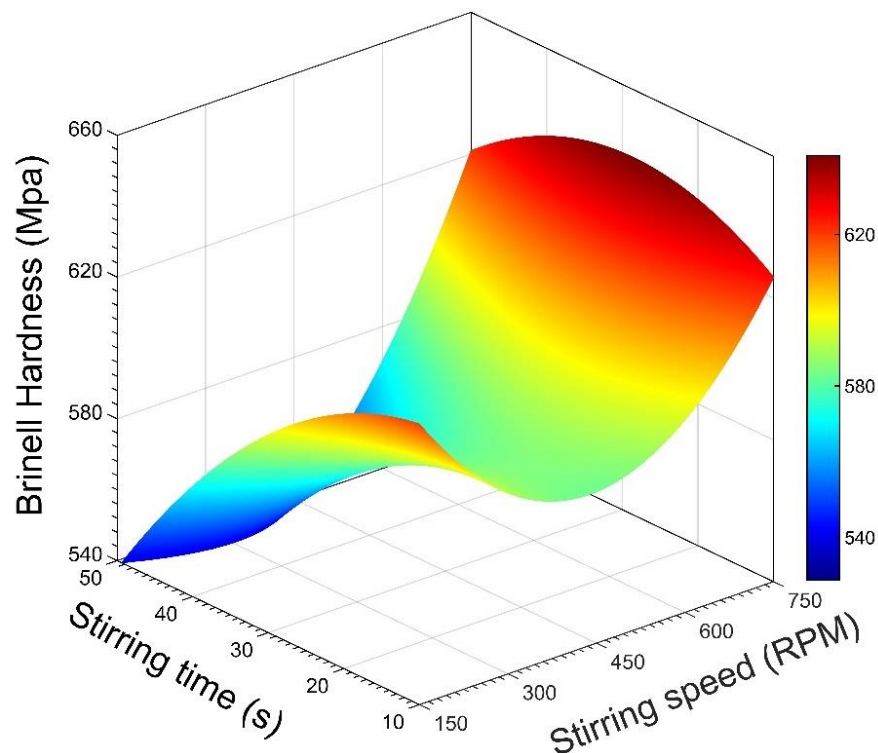


Figure 4.33 Response surface of the Brinell hardness as a function of the stirring time and Stirring speed.

Once again, our objective has been to maximize the Brinell hardness of the fillers using a stir casting process. The response optimizer tool available in Minitab 17 permitted to obtain an optimal response variable, where both factors were assigned the same weight and importance. The weight indicates the distribution of the desirability between the lower or upper limit and goal [43]. The parameters used to calculate the optimal Brinell hardness are summarized in Table 4.12. After computing an optimal Brinell hardness, an optimal multiple response prediction was performed. The ensuing results in Table 4.13 reveal that the optimal levels for this regression model to achieve that maximum Brinell hardness are 2% of NbB_2 , a 750 RPM stirring speed, and 21.717 seconds of stirring time, which leads to a Brinell hardness of 698.494 MPa. The confidence interval (CI) for the prediction was

(653.471, 745.017) MPa for a 95% CI. Desirability estimates how the combination of variables satisfies a set of responses in general. The scale of the composite desirability is in a range of zero and one, where zero indicates that some of the responses are outside the acceptable limits, and one represents the ideal case. Our optimal response had a desirability of 1.

Table 4.12 Parameters to calculate the optimal Brinell Hardness.

Response	Goal	Lower	Target	Upper	Weight	Importance
Brinell Hardness (MPa)	Maximum	490.853	662.975		1	1

Table 4.13 Optimal Response Prediction of Brinell Hardness.

Solution	Percentage (%)	Speed (RPM)	Time (S)	Brinell Hardness (MPa) Fit	Composite Desirability
1	2	750	21.717	698.494	1

Central Composite Design Analysis: Porosity

Figure 4.31 shows the normal probability plot of percent porosity. The graph reveals a typical problem, a sharp curve up and down at both ends, indicating that the tails of this distribution are enough to question the normality assumption. Yet, since the p-value was 0.010, there is enough evidence to conclude that the results do not follow a normal distribution.

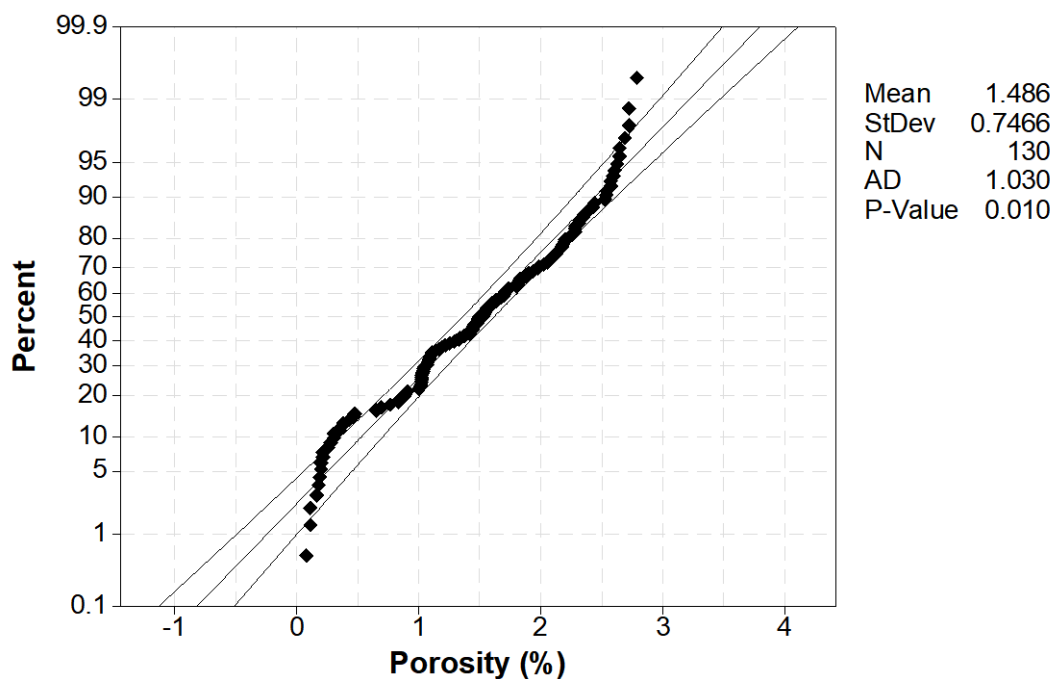


Figure 4.31 Normal probability plot of porosity (%), (95% CI).

Figure 4.32 shows the normal probability plot with the Box Cox transformation of porosity. As mentioned before, a Box-Cox transformation can help correct the curves in the distribution and enhance the residual normalization. In effect, the transformation helped to improve the distribution of the data on the center line and to increase the p-value to 0.079. Minitab calculated the estimated λ as 1.04625

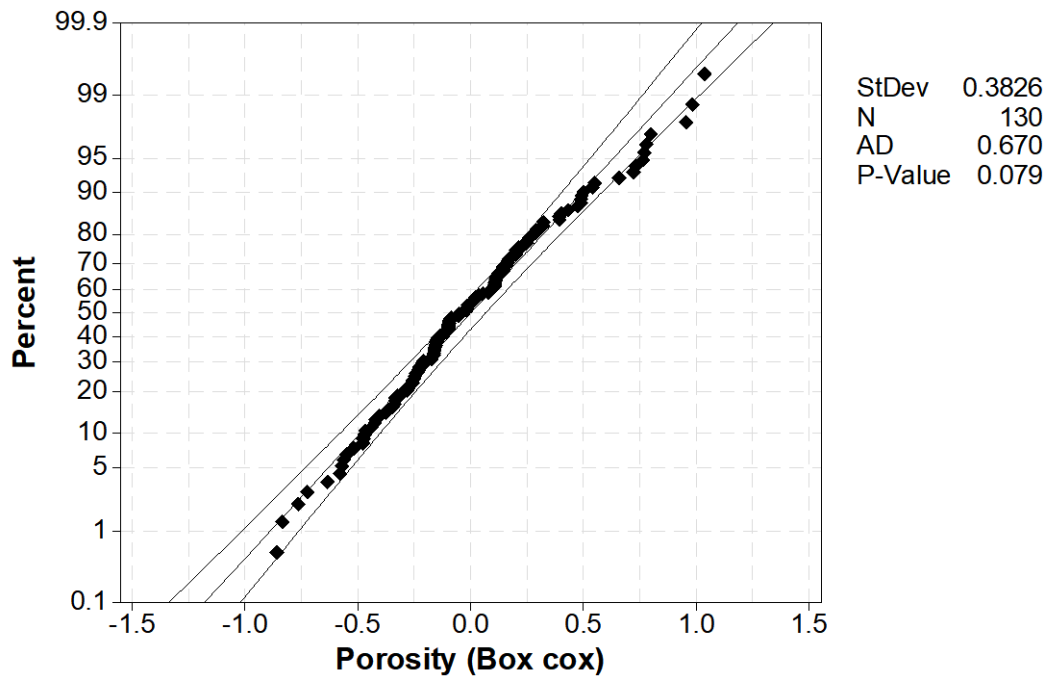


Figure 4.32 Normal probability plot with Box Cox transformation of porosity (95% CI).

The graph shown in Figure 4.33 depicts the deleted residuals as a function of the fitted porosity values, indicating that there are no outliers. Although the residuals variance decreases slightly as a function of the fitted values, the plot does not seem to have a considerably different variability.

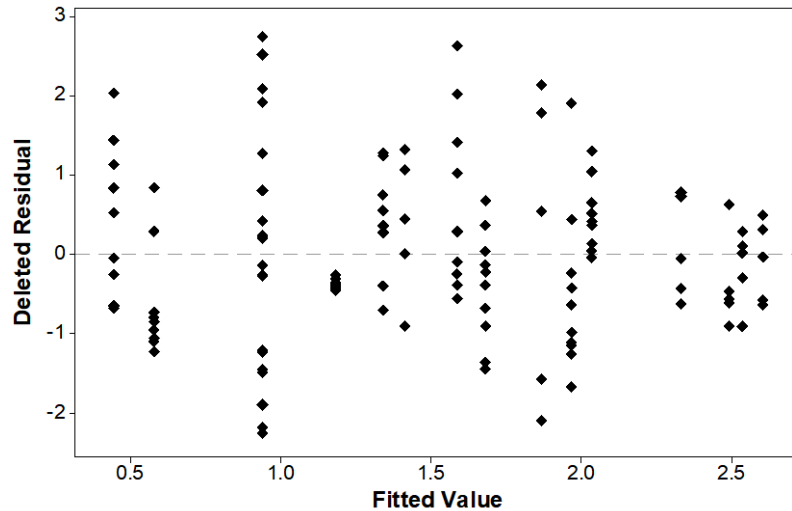


Figure 4.33 Deleted residuals versus as a function of the transformed values of porosity.

In the deleted residual order plot of the porosity graph, i.e. Figure 4.34, the residuals fall randomly around the center line. No pattern is observed, indicating that residuals are not correlated. Therefore, there is no evidence that residues are independent.

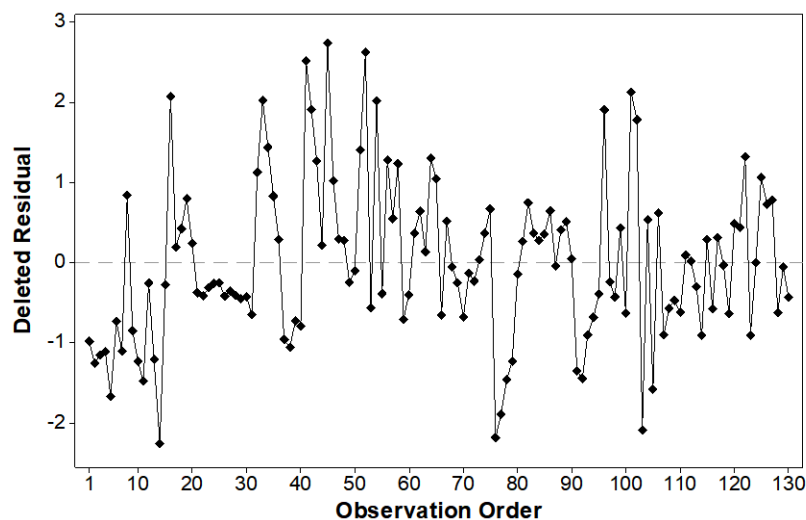


Figure 4.34 Deleted residuals versus order plot of porosity measurements.

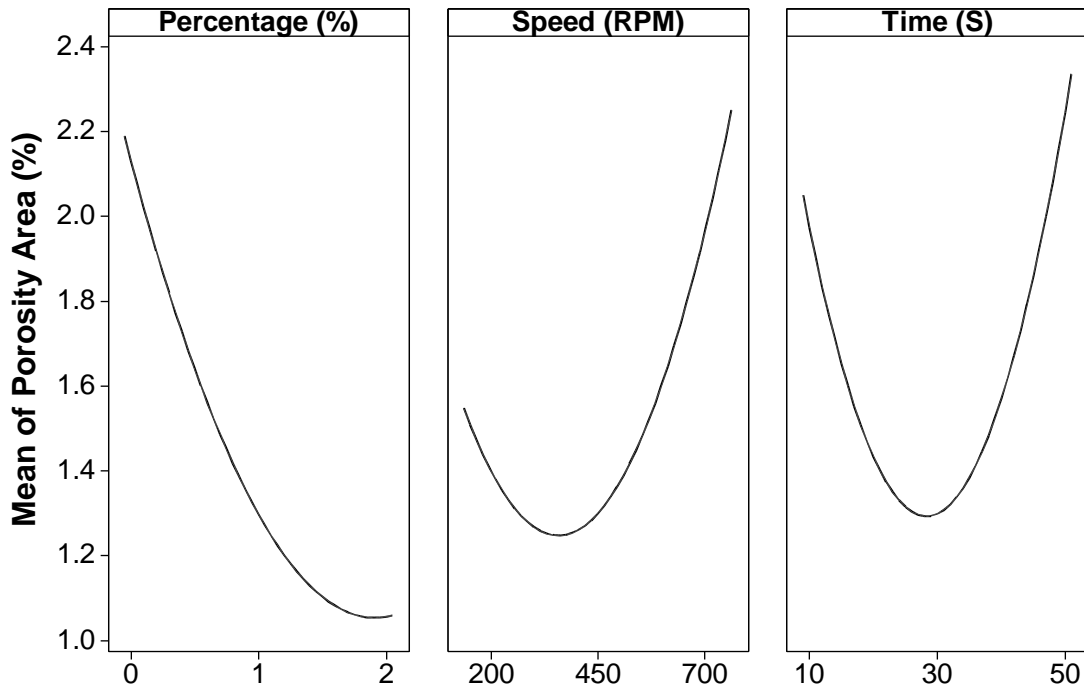
The ANOVA in Table 4.14, again, reveals that the percentage of nanoparticles, with an F-value of 54.74, is the most statistically significant factor. In addition, the interaction between the NbB₂ percent and the stirring speed showed a strong influence on the porosity percent..

Table 4.14 Analysis of variance for transformed response porosity area.

	DF	Adj SS	Adj MS	F-Value	P-Value
Model	10	53.025	5.3025	33.41	0
Blocks	1	8.3991	8.3991	52.93	0
Linear	3	12.5931	4.1977	26.45	0
Percentage (%)	1	8.6864	8.6864	54.74	0
Speed (RPM)	1	3.3546	3.3546	21.14	0
Time (S)	1	0.5521	0.5521	3.48	0.065
Square	3	4.055	1.3517	8.52	0
Percentage (%)*Percentage (%)	1	0.491	0.491	3.09	0.081
Speed (RPM)*Speed (RPM)	1	1.6713	1.6713	10.53	0.002
Time (S)*Time (S)	1	3.6975	3.6975	23.3	0
2-Way Interaction	3	16.1331	5.3777	33.89	0
Percentage (%)*Speed (RPM)	1	13.0154	13.0154	82.02	0
Percentage (%)*Time (S)	1	0.2423	0.2423	1.53	0.219
Speed (RPM)*Time (S)	1	2.8754	2.8754	18.12	0
Error	119	18.8845	0.1587		
Lack-of-Fit	4	3.0355	0.7589	5.51	0
Pure Error	115	15.849	0.1378		
Total	129	71.9095			

The next step is to analyze the main effects individually in order to determine the factor levels that would yield an optimum result. The Main Effects Plot for porosity is shown in Figure 4.35. This tool reveals that, to minimize the porosity in the welding, we must use high NbB₂ percentage, while the stirring time value must remain at the central point value. It should be remembered that in the ANOVA (Table 4.13), there was a strong interaction between the percentage of nanoparticles and the stirring speed.

This is further observed in the graph presented in Figure 4.36 displaying the different interaction combinations. The parallel lines indicate that there is no interaction between the factors, while the steeper the slope between the lines, the greater the magnitude of the interaction. The plot denotes an interaction between the NbB₂ percentage and the stirring speed, with a steeper slope at speeds of 300 RPM and 2% NbB₂. On the other hand, regarding the percentage and the stirring time, the slope of the lines is smaller and at different levels. To better understand the behavior of our model we compared the original data with respect to the regression model. Figures 4.36, 4.37 and 4.38 support the deductions we have discussed previously in the main effects plot of the Brinell hardness.



All displayed terms are in the model.

Figure 4.35 Main effects plot for porosity (%).

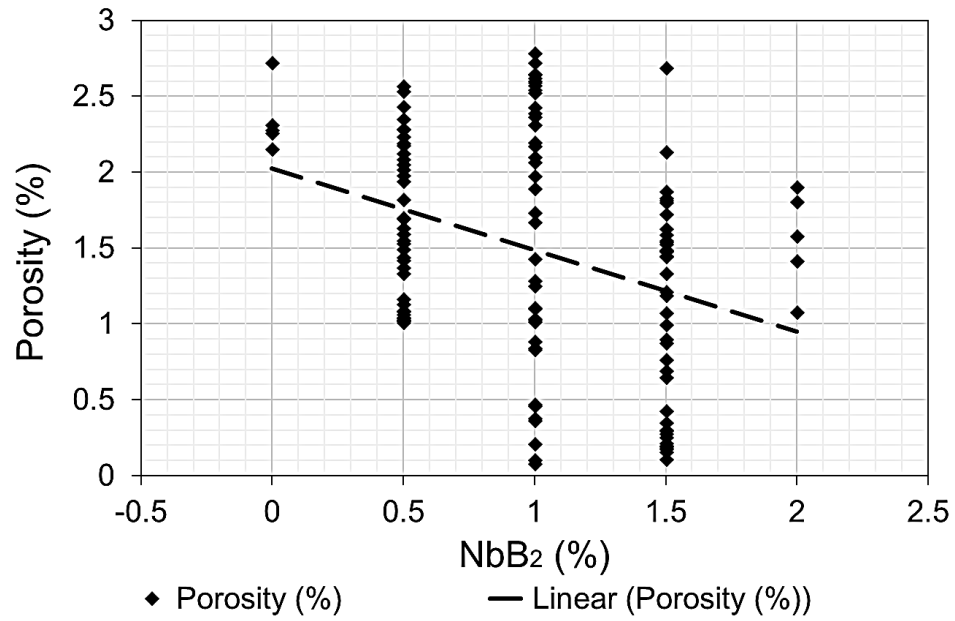


Figure 4.36 Individual value plot of Porosity as a function of the NbB₂ percent using a lineal regression.

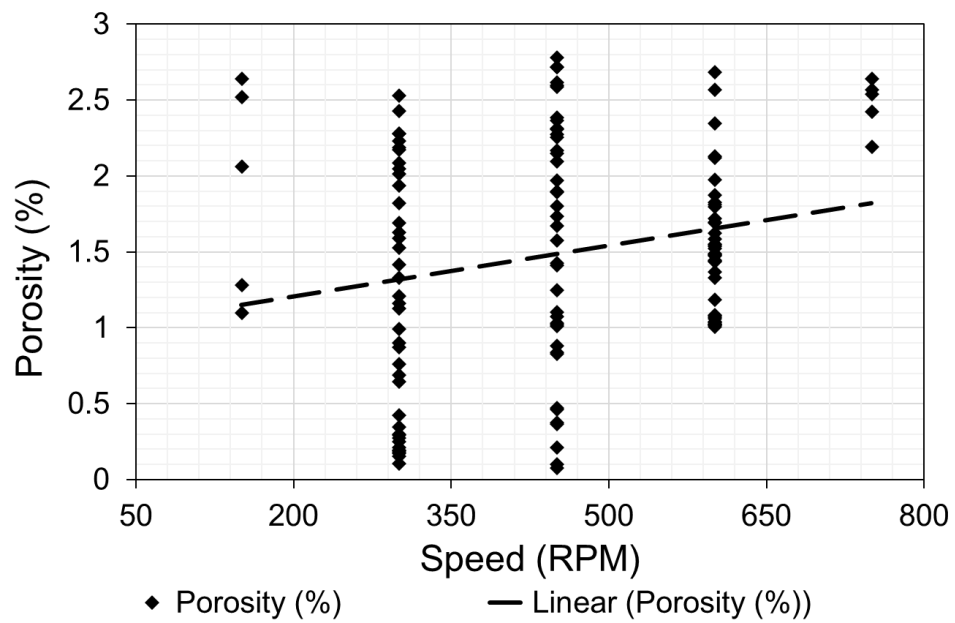


Figure 4.37 Individual value plot of porosity as a function of the stirring speed using a lineal regression.

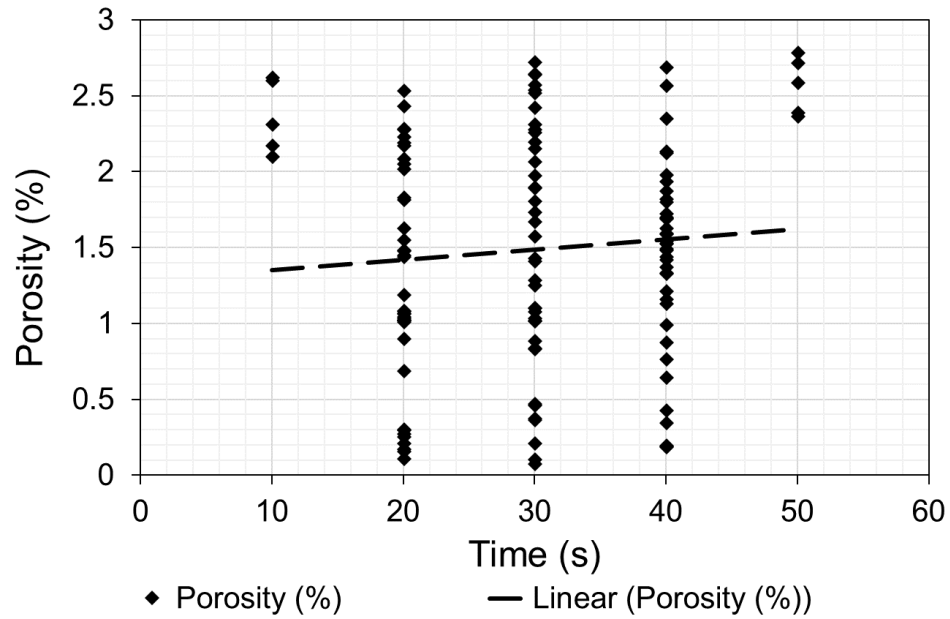


Figure 4.38 Individual value plot of porosity as a function of the stirring time using lineal regression.

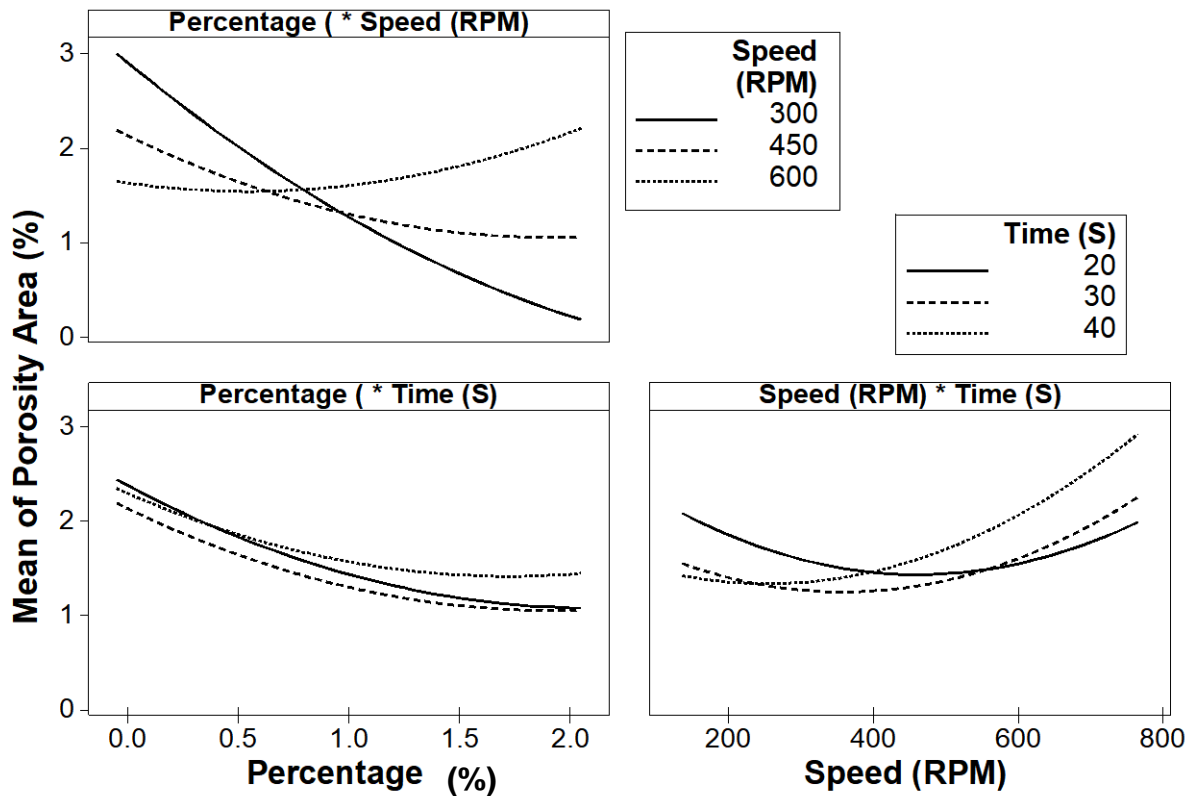


Figure 4.39 Interaction plot for porosity.

Table 4.15 Model summary for transformed response of porosity.

S	R-sq	R-sq(adj)	R-sq(pred)
0.398364	73.74%	71.53%	69.11%

Table 4.15 shows the summary of the model for the porosity transformed response variable. This table presents how well the data fitted the regression model, which is able to predict 69.11% of new observations. The error term, S, is 0.398364. The variance inflator factor (VIF) of the main effects is 1, which indicates that the predictors were not correlated. Table 4.16 shows the model coefficients for transformed response porosity. The main factors are not correlated with predictors.

Table 4.16 Coded coefficients for transformed response porosity.

Term	Effect	Coef	SE Coef	T-Value	P-Value	VIF
Constant		1.298	0.114	11.38	0	
Blocks 1		-0.36	0.0492	-7.28	0	1.41
Percentage (%)	-0.538	-0.27	0.0364	-7.4	0	1
Speed (RPM)	0.3344	0.167	0.0364	4.6	0	1
Time (S)	0.1357	0.068	0.0364	1.87	0.065	1
Percentage (%)*Percentage (%)	0.1477	0.074	0.042	1.76	0.081	1.44
Speed (RPM)*Speed (RPM)	0.2725	0.136	0.042	3.25	0.002	1.44
Time (S)*Time (S)	0.4054	0.203	0.042	4.83	0	1.44
Percentage (%)*Speed (RPM)	0.8067	0.403	0.0445	9.06	0	1
Percentage (%)*Time (S)	0.1101	0.055	0.0445	1.24	0.219	1
Speed (RPM)*Time (S)	0.3792	0.19	0.0445	4.26	0	1

We must recall at this point that the goal of this research segment has been to determine the optimal operating conditions in the stir casting process in order to minimize weld porosity. Briefly, weld porosity could be affected by the strong interaction between the percentage of nanoparticles and the stirring speed. Using the regression equation for

porosity (eq. 04), we can represent the relationship between the independent variables and the response one via a regression model and build a response surface that helps us understand better the influence of the three factors studied during welding.

$$\begin{aligned}
 \text{Regression Equation of Porosity (\%)} = & 8.934 - 3.879 \text{ Percentage (\%)} \\
 & - 0.01351 \text{ Speed (RPM)} - 0.1827 \text{ Time (S)} + 0.295 \text{ Percentage (\%)*Percentage (\%)} \\
 & + 0.000006 \text{ Speed (RPM)*Speed (RPM)} + 0.002027 \text{ Time (S)*Time (S)} \\
 & + 0.005378 \text{ Percentage (\%)*Speed (RPM)} + 0.01101 \text{ Percentage (\%)*Time (S)} \\
 & + 0.000126 \text{ Speed (RPM)*Time (S)}. \quad (\text{eq. 04})
 \end{aligned}$$

Figure 4.37 shows the contour plot generated by the porosity predictive equation and comparing the stirring speed factor against the nanoparticles percent. This graph indicates that at 150 RPM and 2% of nanoparticles, the material displays its minimum porosity. Previous studies concluded that stir casting conducted at high speeds creates turbulence, trapping gases within the Al - Mg melt due to pressure differences. As a result, porosity is inherited by the composite solid. Moreover, for slower stirring speeds, the reinforcement distribution becomes poor and heterogeneous, but the porosity reduction is significant [44]. The response surface of the porosity as a function of the stirring speed vs the NbB₂ percent shown in Figure 4.38 offers a better viewpoint to appreciate the effects of these two competing factors. It clearly demonstrates that as the percentage of nanoparticles is raised, with a stirring speed between 150 and 450 RPM, there is less porosity. However, in the absence of NbB₂ nanoparticles, porosity levels increase for the same stirring speed. To explain this behavior, one must recall that the stir casting process

is influenced by various factors, such as the viscosity of the molten aluminum, the melt high gas solubility (particularly hydrogen), and the cooling rate. The melting temperature is related to the molten aluminum viscosity. Previous works demonstrated that the ultimate tensile strength (UTS) increases as the melting temperature increases, and at 830 °C, the best results are reached [44]. We believe that adding the Al-NbB₂ pellets at room temperature to the molten metal lowered the melt temperature and, consequently, increased its viscosity. As a result, the rotational flow is less turbulent, which in turn, abated the porosity levels [45]. The other factor that plays an important role upon stir casting is time, which we discuss below.

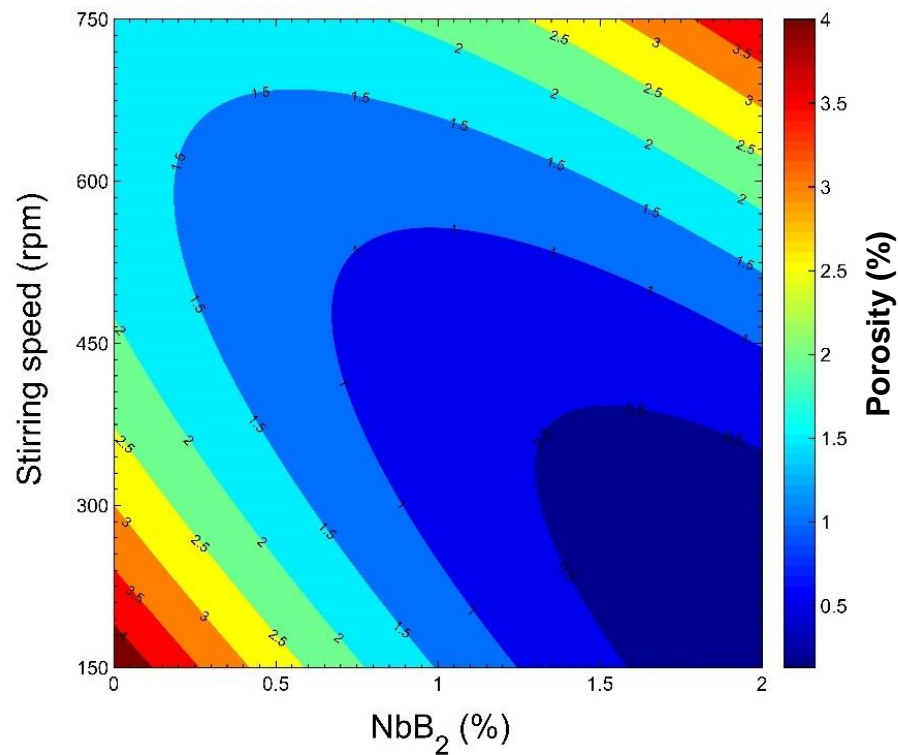


Figure 4.40 Contour plot of porosity as a function of the stirring speed and NbB₂.

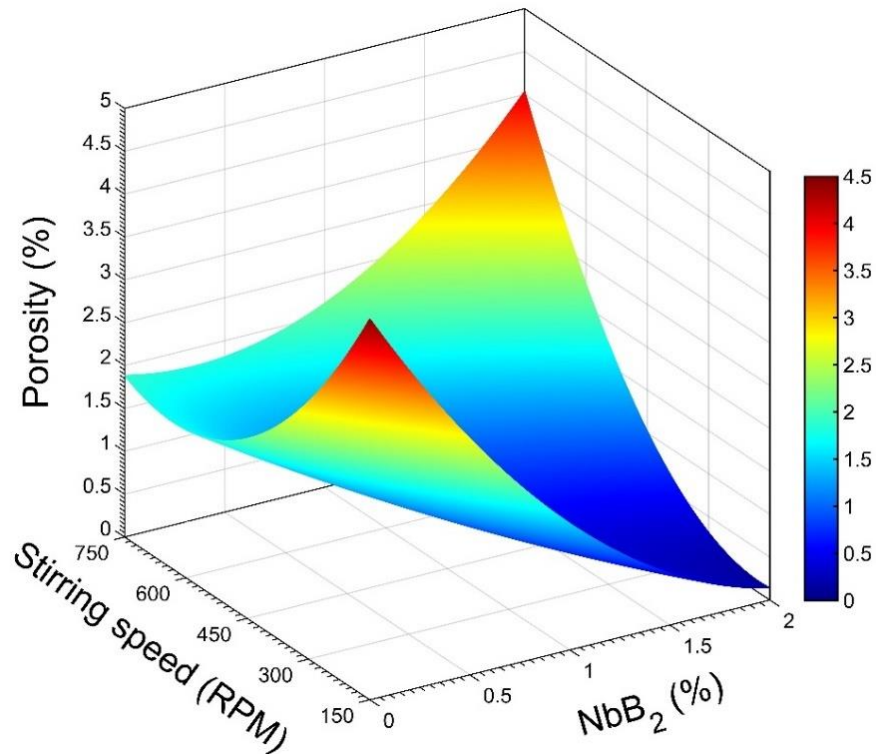


Figure 4.41 Response surface of porosity as a function of the stirring speed and NbB₂.

Figure 4.39 is a contour plot of the response surface in Figure 4.38 that reveals the interaction between the stirring time and NbB₂ percent. The contours are almost concentric ellipses with the center of the system being a point of minimum response. In addition, the graph shows again that the presence of nanoparticles at intermediate levels of stirring time minimized the porosity. Different studies concluded that to achieve a uniform distribution through the stir casting process, the particles need to be dispersed throughout the aluminum melt at the same time. However, this is achieved by force the particles to rotational currents for a defined period of time, while the vortex pulls the reinforcement particles well into the aluminum melt [42], [44], [45].

Yet, a prolonged agitation allows the vortex to suck in more air into the molten aluminum. As a result, greater entrapment of air will induce an increase in porosity. This effect of stirring time is clearly seen in the porosity response surface as a function of the stirring time and the amount of nanoparticles (Figure 4.40). It is observed that at times longer than 40 seconds, high porosity results.

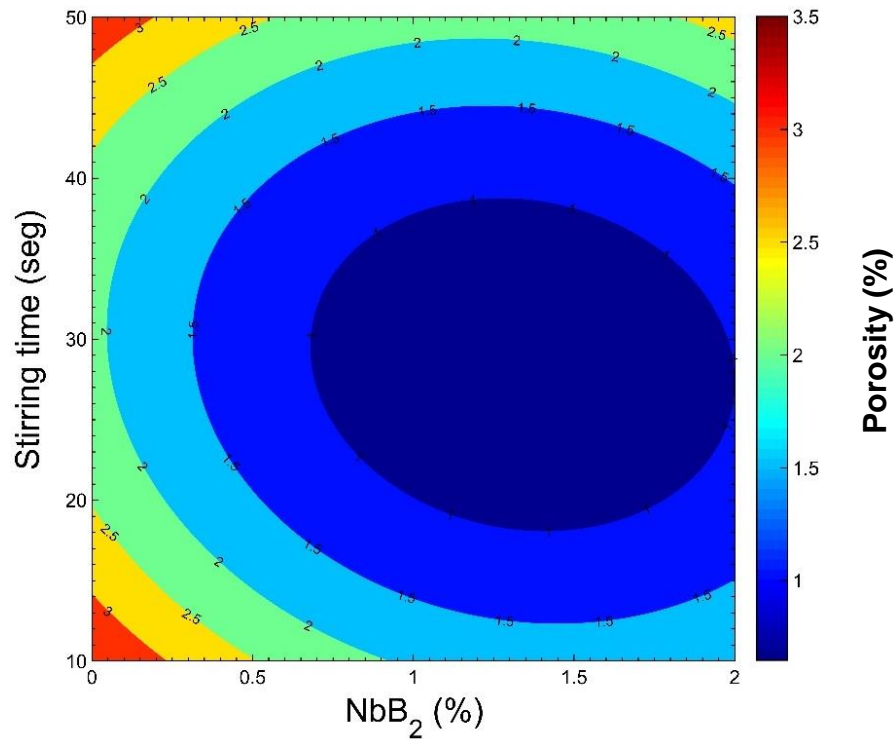


Figure 4.42 Contour plot of the porosity as a function of the stirring time and NbB_2 .

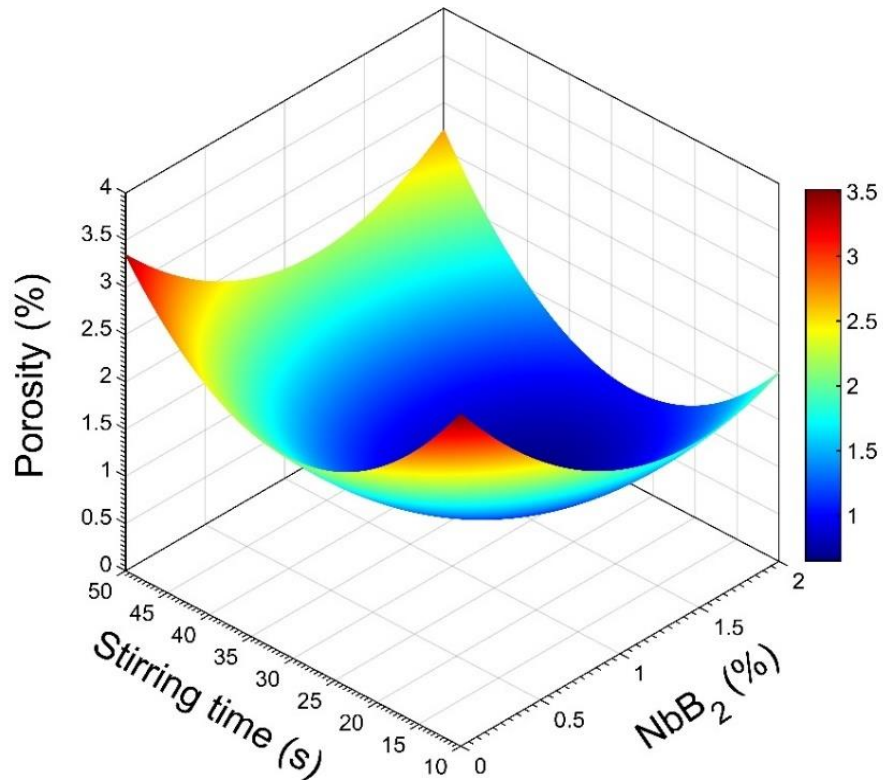


Figure 4.43 Response surface of the porosity as a function of the stirring time and NbB₂.

Previous works related to hardness and porosity demonstrated the influence of stirring time and stirring speed in the nanocomposite manufacturing process [44], [45]. Figure 4.41 exhibits the contour plot of the porosity as a function of the stirring time and speed. The apparent elliptical contour occurs as a result of a significant interaction between the independent variables [46].

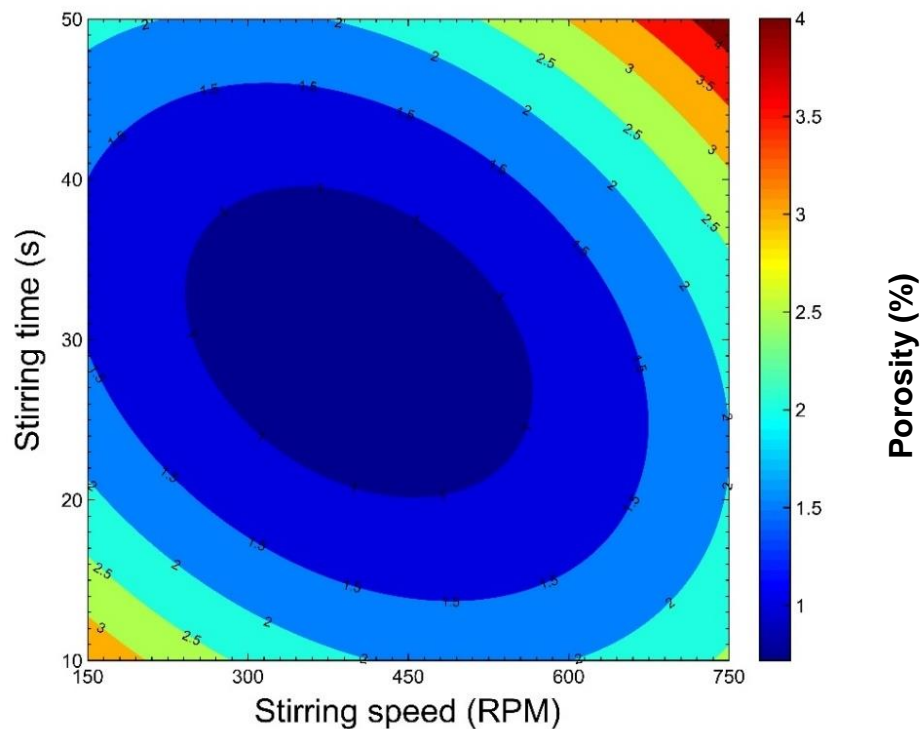


Figure 4.44 Contour plot of the porosity as a function of the stirring time and stirring speed.

The minimum point is assumed to be approximately at the intersection of the major and minor axes of the ellipse. Moreover, the response surface of the porosity as a function of the stirring time and the stirring speed (Figure 4.42) confirms that high stirring speed with prolonged mixing time increases the porosity significantly. This is attributed to the turbulence and the amount of air trapped in by the vortex.

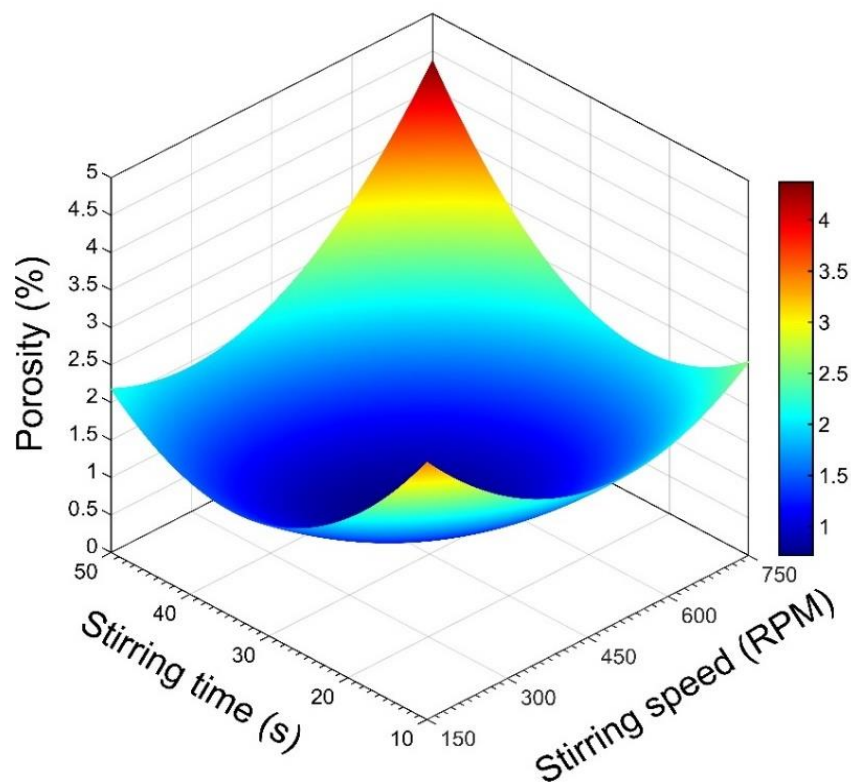


Figure 4.45 Response surface of the porosity as a function of the stirring time and the stirring speed.

Thus far, the goal has been to find the parameters that minimize the porosity of the fillers, allowing for a better quality welding. Table 4.17 shows the parameters used to calculate the conditions for minimal porosity. The response optimizer tool of Minitab 17 permitted to calculate an optimal multiple response prediction. Our results presented in Table 4.18 revealed that the optimal levels to achieve minimum porosity are 2% of NbB_2 , 150 RPM stirring speed, and 35.051 seconds of stirring time. Our desirability value is 1 for the optimal response, i.e. nigh the ideal case.

Table 4.17 Parameters to calculate the optimal of porosity (%).

Response	Goal	Lower	Target	Upper	Weight	Importance
Porosity Area (%)	Minimum		0.07967	2.787	1	1

Table 4.18 Optimal response prediction of porosity (%).

Solution	Percentage (%)	Speed (RPM)	Time (S)	Porosity Area (%) Fit	Composite Desirability
1	2	150	35.051	0.39711	1

Optimal Solution for The Two Variables Brinell Hardness and Porosity

After finding the equation for each response variable and analyzing the optimal solutions, we optimize the two variables using the desirability function. The goal is to find levels that maximize the hardness and capable of maintaining a 4% porosity target, because below this amount, welding quality is considered adequate. The Minitab 17 response optimizer tool allowed calculating an optimal response variable, to get the best welding quality. For the analysis, we assigned the same weight and importance to both factors; the parameters to calculate the optimal are summarized in Table 4.18.

Table 4.19 Parameters to calculate the optimal of Brinell hardness (MPa) and Porosity (%).

Response	Goal	Lower	Target	Upper	Weight	Importance
Porosity (%)	Target	0.08	3.9	4.29	1	1
Brinell Hardness (MPa)	Maximum	490.85	662.98		1	1

After calculating the optimal multiple response prediction, shown in Table 4.19, the optimal levels to achieve best welding with our novel filler are 2% of NbB₂, a 750 RPM of stirring speed and stirring time of 35.292 seconds, with a Brinell hardness of 687.413 MPa, and 3.9% of porosity. The standard error of the fits (SE fits) for porosity was 0.294 and the confidence interval (CI) for the prediction; for a 95%, CI was (2.920, 4.880) percentage. The standard error of the fits (SE fits) for Brinell hardness was 20 and the confidence interval (CI) for the prediction; for a 95%, CI was (620.8, 754.1) MPa.

Table 4.20 Optimal Response Prediction of Brinell hardness (MPa) and Porosity (%).

Solution	Percentage (%)	Speed (RPM)	Time (S)	Porosity (%) Fit	Brinell Hardness (MPa) Fit	Composite Desirability
1	2	750	35.292	3.9	687.413	1

4.2.3 Conclusions

In the present chapter, the process of stir casting for the Al-NbB₂ filler manufacturing for aluminum welding is optimized. As a general conclusion, it was possible to obtain a better welding quality, and the wettability between the NbB₂ and the aluminum matrix was appropriate to achieve a homogeneous filler. In addition, one can conclude that the factors studied, i.e. stirring speed, stirring time, and percentage of nanoparticles, have a significant influence on the mechanical properties of the weld. The main conclusions are summarized as follows:

- ♦ In the presence of 2% of NbB₂ nanoparticles the solder improves its hardness with a 0.4 % of porosity.
- ♦ A prolonged stirring time of 50 s produced 2.787% porosity, the highest percentage obtained during the study. This was due to the high amount of air sucked by the vortex and trapped in the melt.
- ♦ Central composite analysis indicated that to maximize the weld hardness and reduced the porosity, a filler bearing 2% NbB₂ was needed. The settings to obtain 687 MPa of Brinell hardness were: a stirring speed of 750 RPM and a stirring time of 35.292 s.

V. CHAPTER

5. Comparative Analysis of NbB₂-Treated Filler to Commercial 5356 Filler

Aluminum welds need to meet strict requirements for strong joints while adding minimal weight, as demanded in many aerospace structures. However, the performance of these welds at high temperatures is unsatisfactory, showing crack sensitivity. Pure aluminum has a tensile strength of about 90 MPa, that can significantly increase to 690MPa with alloying elements such as manganese, silicon, copper, and magnesium [47]. Unfortunately, when welding Al and its alloys, the weld properties seldom match those of the base metal; this represents an inability to attain adequate joint strength that is critical for effective load transfer among structural pieces. Heat treatments can restore much of that strength loss in some alloys. Nonetheless, in last-minute repair welds, those treatments may not be an option. To address this issue upon welding, the addition of nanocomposites as aluminum filler materials appears to be an appealing alternative to enhance the mechanical properties of welds.

It is known that TIG welding allows for greater control in weld penetration and cleanliness, leading to high quality weld joints [48], [49]. Such quality of a TIG-welded component is influenced by proven factors, like the gap between the parts, the torch angle, the pulse frequencies, and the electrode tip angle during welding. Further, metal filler material used during the TIG process can also affect the quality of a welded component. The ASM

Handbook Vol 6 [26] provides guidelines to incorporate and evaluate the different variables that affect the quality of metal welding, the ease of welding, strength of weld joint, weld ductility, its corrosion resistance, service temperature, and post weld treatment. These guidelines also assist in the selection process of filler materials as a function of the parent aluminum alloy [2], [4]. 6xxx series aluminum alloys can be welded with 5xxx series fillers (bearing nominally 5% Mg), providing higher ductility, higher tensile and shear strength, crack sensitivity, and best feedability when compared to 4xxx series aluminum alloy fillers (5% Si). Hence, this chapter focuses on the comparison of an Al-5% Mg filler reinforced with NbB₂ nanoparticles, and a commercial Al 5356 alloy filler (PowerWeld, Grand Prairie, TX, USA), selected for having elevated service temperature characteristics. To establish the adequacy of this new filler, several characterization techniques were used.

5.1 Full Factorial Experiment to Compare the Thermal Expansion Coefficient of Both Fillers Before Welding

The thermal expansion coefficient (CTE) of the filler with nanoparticles was measured and compared to the one of the commercial filler through a full factorial design experiment. Factorial designs offer the advantage of estimating the effects of a factor with several levels of the other factors, but in order to estimate the effect, it is necessary to verify the adequacy of the model. The CTE was obtained via thermomechanical analysis (TMA). In effect, the thermomechanical analyzer can experimentally provide a relationship between a material's mechanical properties and its temperature.

5.1.1 Methodology

As mentioned, the coefficients of thermal expansion (CTE) for the novel filler (containing NbB₂) and the commercial filler (5356) were compared via a statistical experimental design by performing measurements at 150°C and 300°C. A 2² full factorial with 4 replicates was used to perform the analysis, meanwhile a thermomechanical analyzer (TMA) permitted to measure the CTE with prepared samples based on the standard of the American Society for Testing and Materials (ASTM) E831-14 (Standard Test Method for Linear Thermal Expansion of Solid Materials by Thermomechanical Analysis) [50]. A variance analysis evaluated differences in hardness in both NbB₂-reinforced weld and non-reinforced weld. Characterization of the fabricated filler material was conducted on specimens prepared with the TIG welding technique following the AWS 5.10 standard.

Sixteen randomly ordered (Minitab 17 software) runs were completed. Figure 5.1 shows the graphical representation of the full factorial, and Table 5.1 presents the factors with their respective levels. The full factorial design matrix of CTE obtained from Minitab are presented in Appendix C.1.

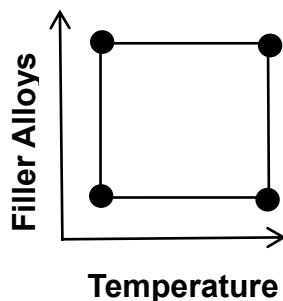


Figure 5.1 2² full factorial design for the novel filler NbB₂ and the commercial filler 5356.

Table 5.1 Full factorial Parameter for the novel filler NbB₂ and the commercial filler 5356.

Parameter	Units	Lower	Higher
Filler Alloys	Type	5356	Al-Mg-NbB ₂
Temperature	Celsius	150	300

Four samples of each filler (with an average sample length of 5.22 mm) were placed in the TMA instrument set at a constant load of 0.05N to register volumetric changes at 150°C and 300 °C. Figure 5.2 shows a schematic of the mechanical thermal analysis unit. The change in material length as a function of temperature and time was observed and then the thermal expansion of the material was computed.

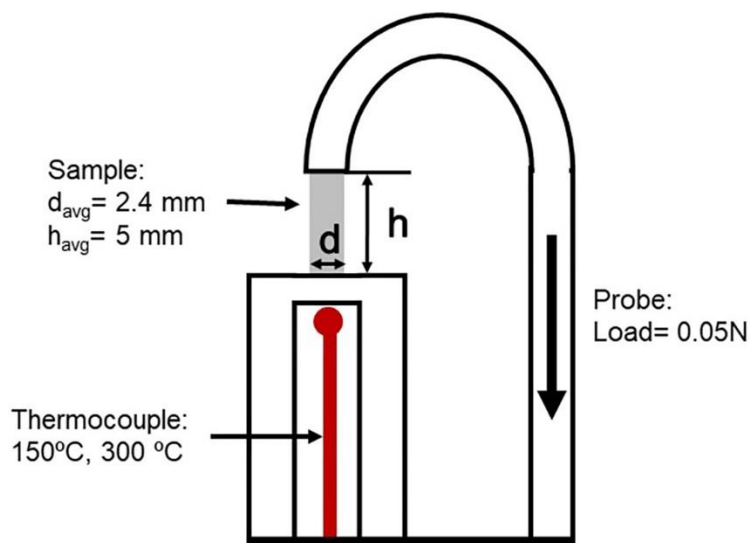


Figure 5.2 Schematic of the thermomechanical analysis unit.

5.1.2 Results and Discussion

Full Factorial Analysis of thermal expansion coefficient

The first aspect to verify is the normality assumption. Figure 5.3 shows the normal probability plot of the measured CTE values. The Anderson-Darling normality test reveals that the p-value is 0.05, which marginally points at a normal distribution. The results are presented in Appendix C.1 together with the full factorial design matrix of thermal expansion coefficient. However, this chart does give more information on the behavior of the data, for example, it shows some extreme values and dispersion in both tails. Also, the tendency of the graph to curve down slightly to the left side could indicate that the results do not exactly follow a normal distribution. At this point, a Box Cox transformation was implemented to investigate whether it would improve the residuals normalization and to better the variance. In effect, Box Cox easily normalized the skewed data, so that one can get a better estimate of the effects.

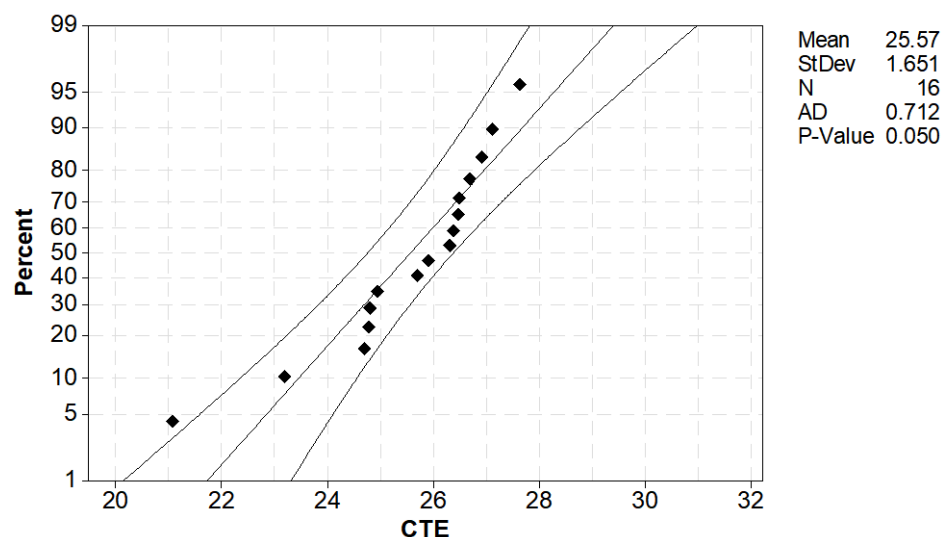


Figure 5.3 Probability plot of thermal expansion coefficient (95% CI).

Figure 5.4 shows the normal probability plot with the Box Cox transformation of the CTE. One can observe that the dispersion of the data is lesser, although some bias remains in both tails. However, in these cases, more attention should be paid to the central values of the graph than to the extreme ones. A distribution that has thin or thick tails is not of greater concern if the tails are not considerably skewed. The transformation helped to improve the distribution of the data on the central line and to increase the p-value to 0.818.

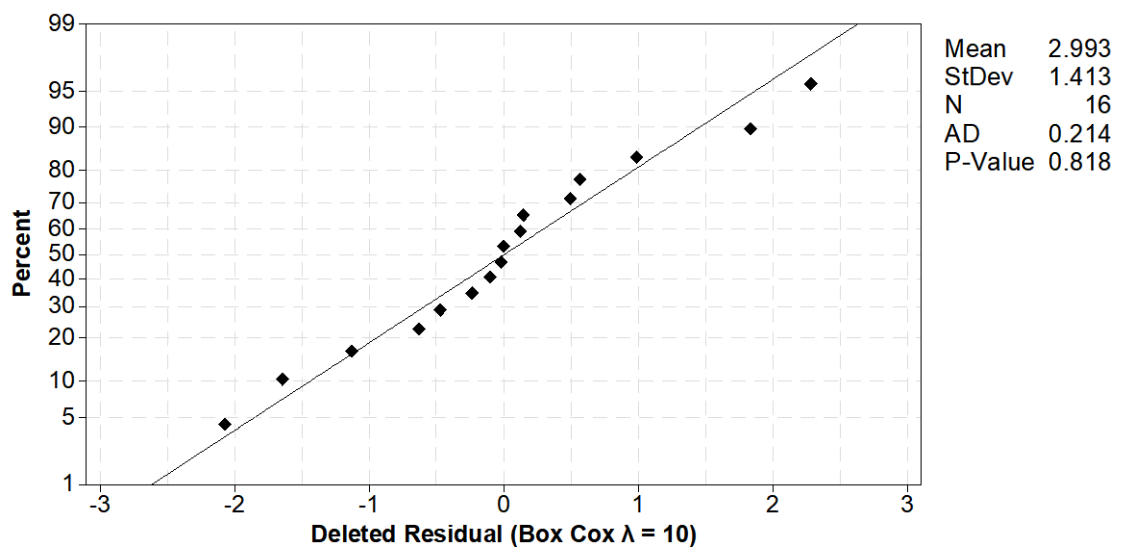


Figure 5.4 Normal probability plot with Box Cox transformation of the thermal expansion coefficient (95% CI).

Figure 5.5 shows the deleted residuals versus fitted values; here the residuals show particular structure. Further exploration is encourage to understand the heteroscedasticity on the residual. The assumption of independence is verified in Figure 5.6, which presents the residuals versus deleted residuals plot of the thermal expansion coefficient. This graph can be used to find non-random errors, because there is no reason to suspect any violation of independence assumptions.

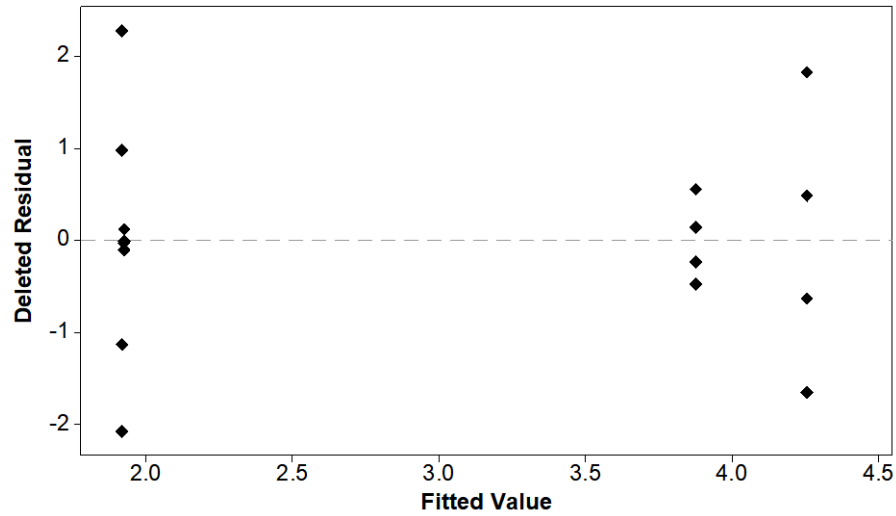


Figure 5.5 Deleted residuals versus the fitted value of thermal expansion coefficient.

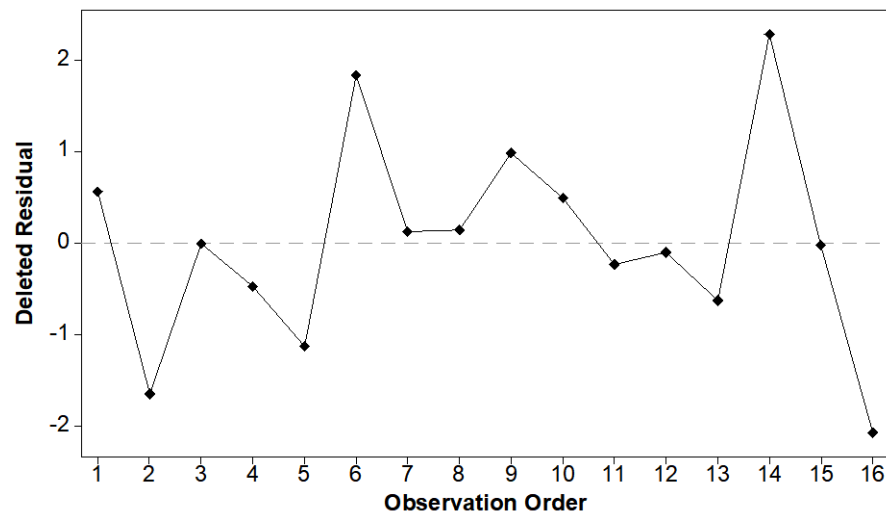


Figure 5.6 Residuals versus order plot of thermal expansion coefficient.

The analysis of variance is summarized in Table 5.2. Since, the F-value for the temperature is 19.68, one can conclude that the temperature is the main effect in both fillers. Both had a p-value of 0.15, which indicates that there is no significant difference

between their CTE. In conclusion, the optimization of the manufacturing process was able to improve the quality of the filler reinforced with nanoparticles to make the experimental filler comparable with the commercial one.

Table 5.2 Analysis of Variance for Thermal expansion coefficient.

	DF	Adj SS	Adj MS	F-Value	P-Value
Model	3	18.703	6.2342	6.66	0.007
Linear	2	18.554	9.2771	9.92	0.003
Filler Alloys	1	0.1372	0.1372	0.15	0.708
Temperature	1	18.417	18.417	19.68	0.001
2-Way Interactions	1	0.1485	0.1485	0.16	0.697
Filler Alloys*Temperature	1	0.1485	0.1485	0.16	0.697
Error	12	11.228	0.9356		
Total	15	29.93			

Figures 5.7 and 5.8 show the Pareto chart and the normal plot of the standardized effects, respectively. The normal and Pareto plots help us visualize the magnitude and the effect of each factor. The Pareto plot presents the absolute value of the effect and draws a reference line; the temperature is the effect that exceeds this line. Therefore, it is considered statistically significant.

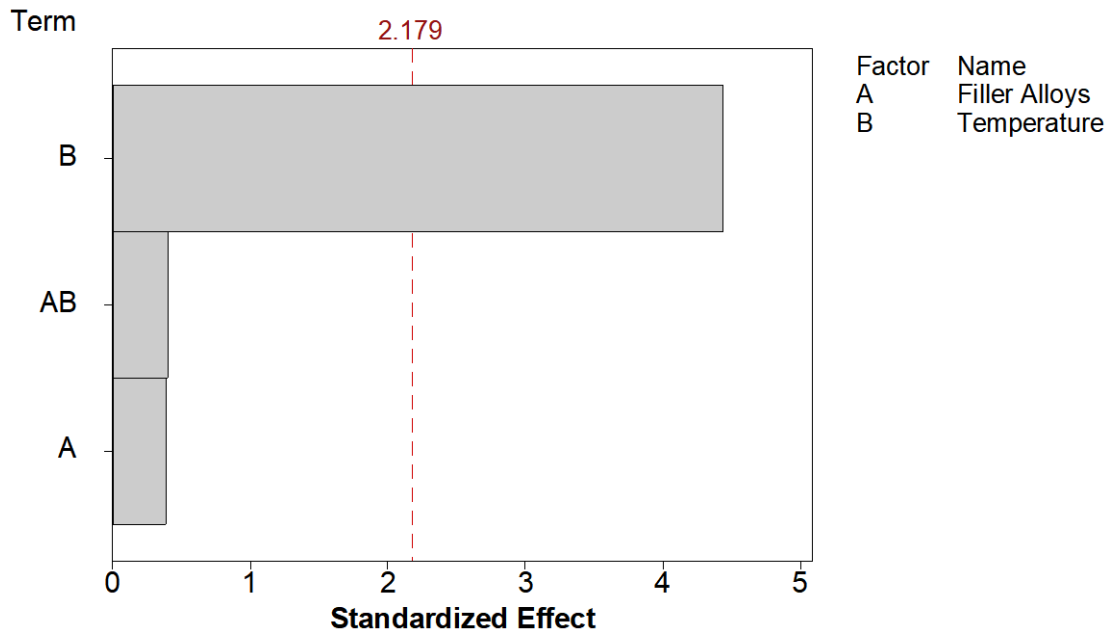


Figure 5.7 Pareto chart of the standardized effects of thermal expansion coefficient ($\alpha = 0.05$).

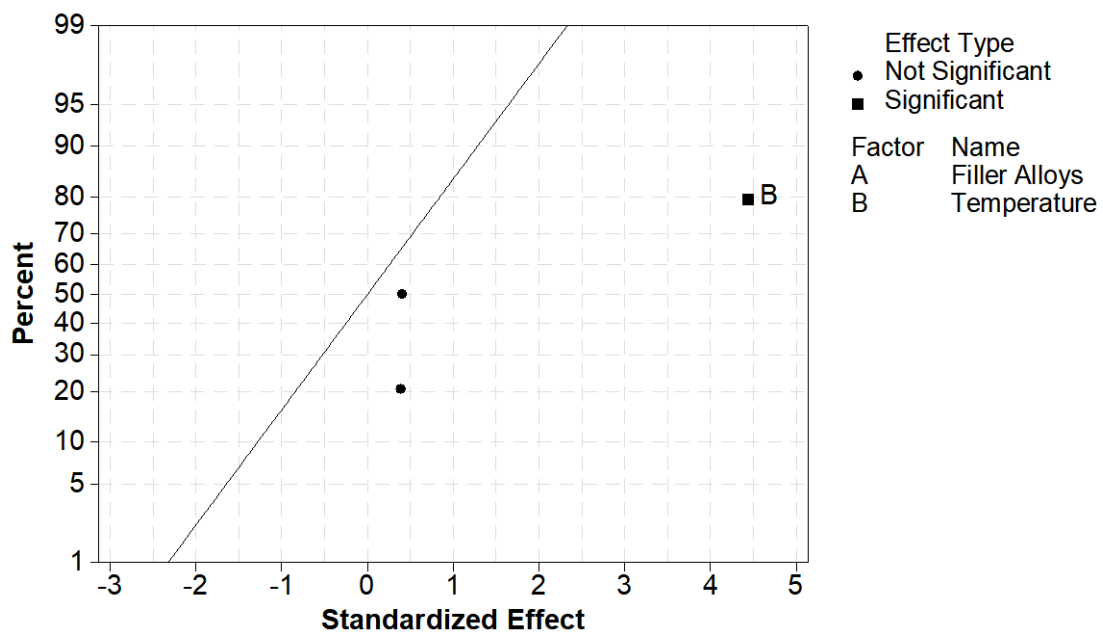


Figure 5.8 Normal plot of the standardized effects of thermal expansion coefficient ($\alpha = 0.05$).

Another useful chart for the practical interpretation of this experiment, presented in Figure 5.9, shows the two main effects and interaction between filler alloy and temperature. The lines do not intersect, which means that the interaction is not significant. Table 5.3 presents the transformed response model summary, showing how the data fits the regression model. However, our model can predict only a new observation with 33.31%. The model has an R^2 of 62.49%, and the error term, $S = 0.967287$, is small. Table 5.4 shows the coefficients of the model terms. As an assumption of orthogonality, each effect is estimated independently. The Variance Inflation Factor (VIF) effects and interactions are 1, indicating that predictors are uncorrelated.

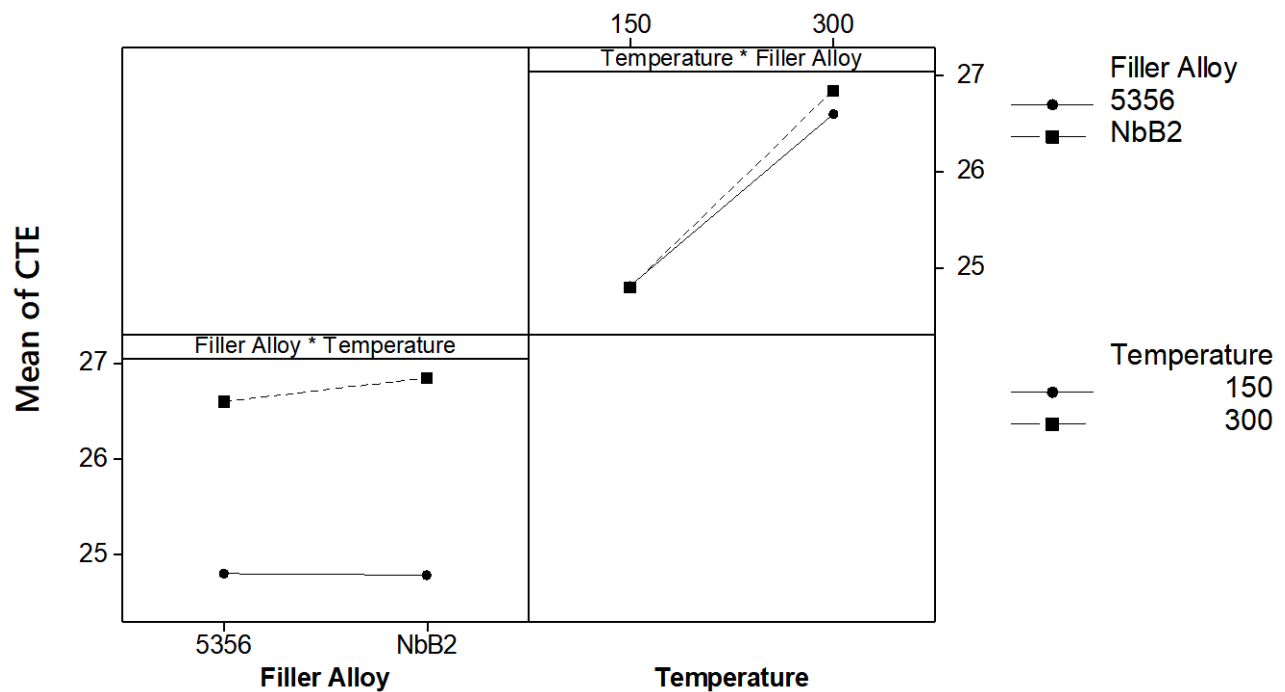


Figure 5.9 Interaction plot for thermal expansion coefficient (fitted means).

Table 5.3 Model Summary for Thermal expansion coefficient.

S	R-sq	R-sq(adj)	R-sq(pred)
0.967287	62.49%	53.11%	53.31%

Table 5.4 Coded Coefficients for Thermal expansion coefficient.

Term	Effect	Coef	SE Coef	T-Value	P-Value	VIF
Constant		2.993	0.242	12.38	0	
Filler Alloys	0.185	0.093	0.242	0.38	0.708	1
Temperature	2.146	1.073	0.242	4.44	0.001	1
Filler Alloys*Temperature	0.193	0.096	0.242	0.4	0.697	1

In our analysis, Figure 5.10 shows the cube plot for thermal expansion coefficient (fitted means), which is the relationship between factors and response that helps to predict values for each factor level combination using the means. As mentioned above, the temperature had a significant effect on both fillers, but the difference of CTE between the fillers in both temperatures was low. The optimization of the manufacturing process of our NbB₂-reinforced filler satisfies our expectations to compete with the commercial material, i.e. AA 5356. In previous experiments presented in chapter 3.1, our material did not meet the requirements to compete with the commercial material. However, after implementing the optimization process, the NbB₂ filler had a lower CTE when compared to the commercial one at 150 °C, while the commercial filler was better at 300°C, an operation temperature that is not realistic for aluminum structures. Figure 5.11 show the Individual value plot of the thermal expansion coefficient as a function of the temperature (lineal regression). This graph helped to understand the high dispersion of the CTE between the two fillers at 150 °C. Moreover, at 300 °C both materials presented CTE values with smaller dispersion. On the other hand, when we compare in the Individual value plot for thermal expansion coefficient (° C⁻¹) as a function of the fillers with linear regression, we

observe that our experimental filler has a high variability compared with the commercial material (Figure 5.12).

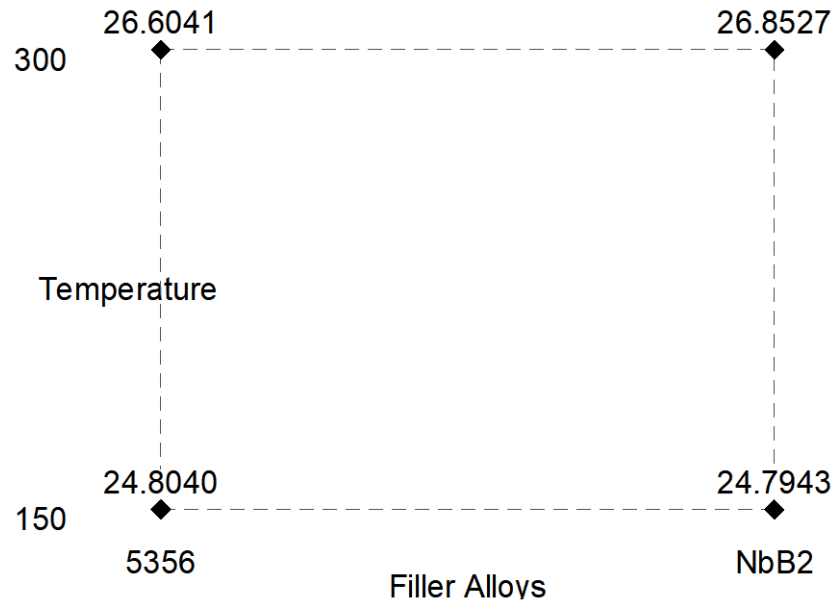


Figure 5.10 Cube Plot for thermal expansion coefficient ($^{\circ}\text{C}^{-1}$) fitted means.

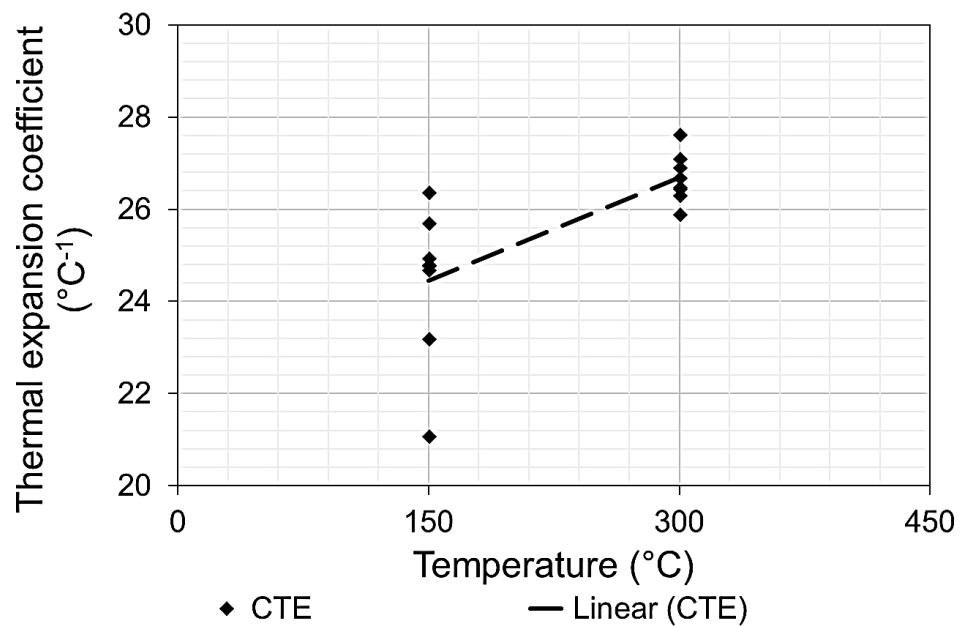


Figure 5.11 Individual value plot for thermal expansion coefficient ($^{\circ}\text{C}^{-1}$) as a function of the temperature with lineal regression.

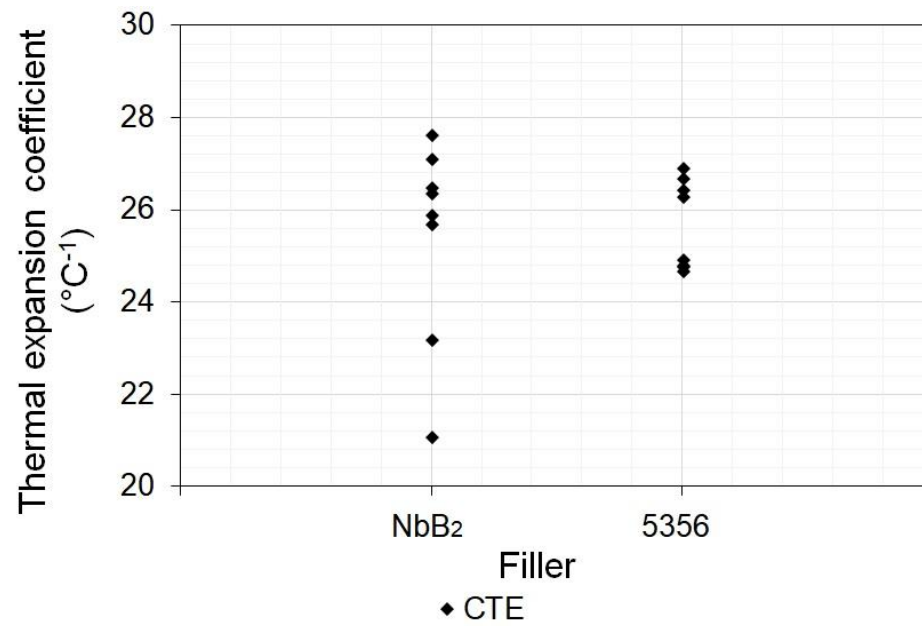


Figure 5.12 Individual value plot for thermal expansion coefficient (°C⁻¹) as a function of the fillers.

5.1.3 Conclusions

This preliminary comparative analysis enabled us to fulfill a main objective of this thesis: to develop a novel filler interchangeable with competing commercials, that is adaptable to TIG welding methods. The thermal expansion coefficient of the filler with nanoparticles was measured and compared to the one of the commercial filler (5356). The CTE was obtained via thermomechanical analysis by performing measurements at 150°C and 300°C. Accordingly, here are the main conclusions:

- ♦ The temperature is the main effect in both fillers, and the interaction between the temperature and filler alloys is not significant.
- ♦ Al-5% Mg filler reinforced with NbB₂ at 150°C has an average coefficient of 24.7 °C⁻¹, compared to 5356 with an average coefficient of 24.8 °C⁻¹. Moreover, at 300°C the NbB₂ filler has a coefficient of 26.8 °C⁻¹, higher than the one for 5356 with 26.6 °C⁻¹.
- ♦ The thermomechanical analysis showed that the quality of the filler reinforced with nanoparticles is comparable with the commercial one. This leads to a filler that can compete with 5356 commercial ones, which require post-welding treatment to achieve proper microstructure and strength.

5.2 Comparison of the experimental and commercial fillers after welding

Filler alloys for aluminum can typically meet or exceed the tensile strength of the base material in the as-welded condition. Since aluminum welding is more complex than in other metals, selecting the correct filler is based on the conditions and job specifications. Important considerations must be the ease of welding, critical chemistry, crack sensitivity, groove weld tensile strength, ductility, corrosion resistance, service temperature, and post-weld heat treatment [27]. Accordingly, this research sought to produce a filler able to compete with commercial aluminum - magnesium alloy fillers (5xxx series). These fillers possess a higher strength, on-heat treatable aluminum alloys and, for this reason, are utilized in structural applications.

After analyzing the thermal expansion coefficient of both fillers without welding, one can conclude that the experimental filler reinforced with 1% nanoparticles ($24.6\text{ }^{\circ}\text{C}^{-1}$) performed better at 150°C than the commercial filler ($24.7\text{ }^{\circ}\text{C}^{-1}$). Thus, the core of this section is to compare the weld quality of both filler materials on the same base material, i.e. an AA 6061 aluminum alloy. Brinell hardness values on the surface of the weld and a subsequent analysis of the resulting heat affected zone (HAZ) allowed assessing the properties of the welded work piece. The HAZ is the region in the base material, which is not melted but has its microstructure and properties altered by welding heat [26], [27]. To compare the experimental filler with the commercial one, we ran descriptive statistics..

5.2.1 Methodology

Two different fillers were manufactured following the optimal parameters studied in Chapter 4, and using 1 and 2 wt% of nanoparticles added to an Al - 5 wt% Mg binary alloy; both fillers had a 2.4 mm diameter. The weld joint for the commercial 5653 filler was prepared using 2.4 mm diameter wires. The welding parameters were controlled by the same TIG machine furnished with a 2.4 mm diameter tungsten electrode. The range of parameters and constant settings used to weld the samples were provided in Section 3.1.1.5. Argon with a 15 l/min flow rate was the shielding gas. Table 5.5 provides the chemical composition of the NbB₂ filler, the 5356 filler, and the 6061 base material are shown in.

Table 5.5 Chemical composition of NbB₂ filler, 5356 filler and 6061-base material (wt.%).

	Mg	Mn	Cr	Cu	Fe	Si	Ti	Zn	Be	NbB ₂	Al
AA 6061 (base material)	≤1.2	≤0.15	≤0.35	≤0.4	≤0.7	≤0.5	≤0.15	≤0.25	-	-	Balance
5356 (commercial material)	≤5.0	0.2	0.2	0.1	0.4	0.25	0.2	0.1	3E-04	-	Balance
Al-Mg-NbB ₂ (experimental filler)	≤5.0	-	-	-	-	-	≤0.001	-	-	≤ 2.0	Balance

Two different hardness tests, namely Brinell and Vickers, permitted to compare the hardness in the HAZ and fillers. A Brinell hardness test was conducted on the surface of the welding. Four specimens were welded with each type of filler, and 5 indentations per sample were made to reduce experimental error in the random order of the runs. Commonly, this HAZ studies employ Vickers hardness tests on the cross-section of the

welded sample. To this purpose, a horizontal band saw allowed cutting our specimens at low speed. Constant lubrication helped reduce local heating and surface defects in the area to be analyzed. Finally, standard grinding and polishing recommended for aluminum permitted to obtain a mirror-like surface [32]. The Vickers hardness measurements at two different depths of the transverse section of the welded workpiece followed the ASTM E384-17 & ASTM E92-17 standards (Figure 5.13). In this hardness test a diamond tip applied a specified load onto the sample surface and the extension of the indent is measured to compute the hardness value, as the apparent contact pressure. The resulting indentation or permanent deformation depends on the shape of the indenter. The test load and the area of the indentation are used to calculate the microhardness. The distance from the top indentation line is at a depth of 1 mm from the top of the sample (top line), whereas the second line at a depth of 2 mm (bottom line). In addition, for each test line, 15 indentations with a load of 0.2 kg allowed obtaining the Vickers hardness value (HV 0.2 scale). The schematic of microhardness tests on the HAZ is shown in Figure 5.11.

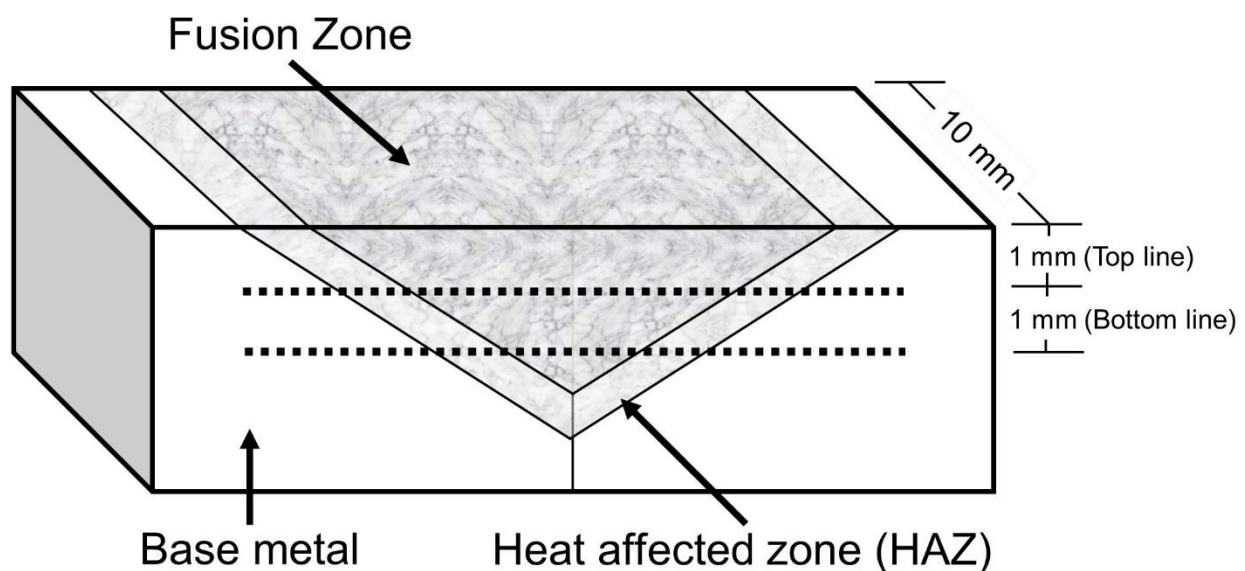


Figure 5.13 Schematic of microhardness indentations of heat-affected zone.

5.2.2 Results and Discussions

Comparison of welding Brinell hardness on the weld surface

Figure 5.14 illustrates the dot plot of the hardness for the experimental filler, the 5356, and the 6061 base material. The diagram reveals that in the presence of 1 and 2 percent of NbB_2 , the hardness value dispersion is lower than for the 5356 filler. Table 5.6 shows the descriptive statistics of the experiment. In the presence of 2% NbB_2 , the average hardness is 798.34 MPa, which is greater than the average hardness of the 5356 weld, which is 792.3 MPa. We can also underscore that using the experimental filler renders a much smaller standard deviation of the hardness values, compared to the commercial material and the base material.

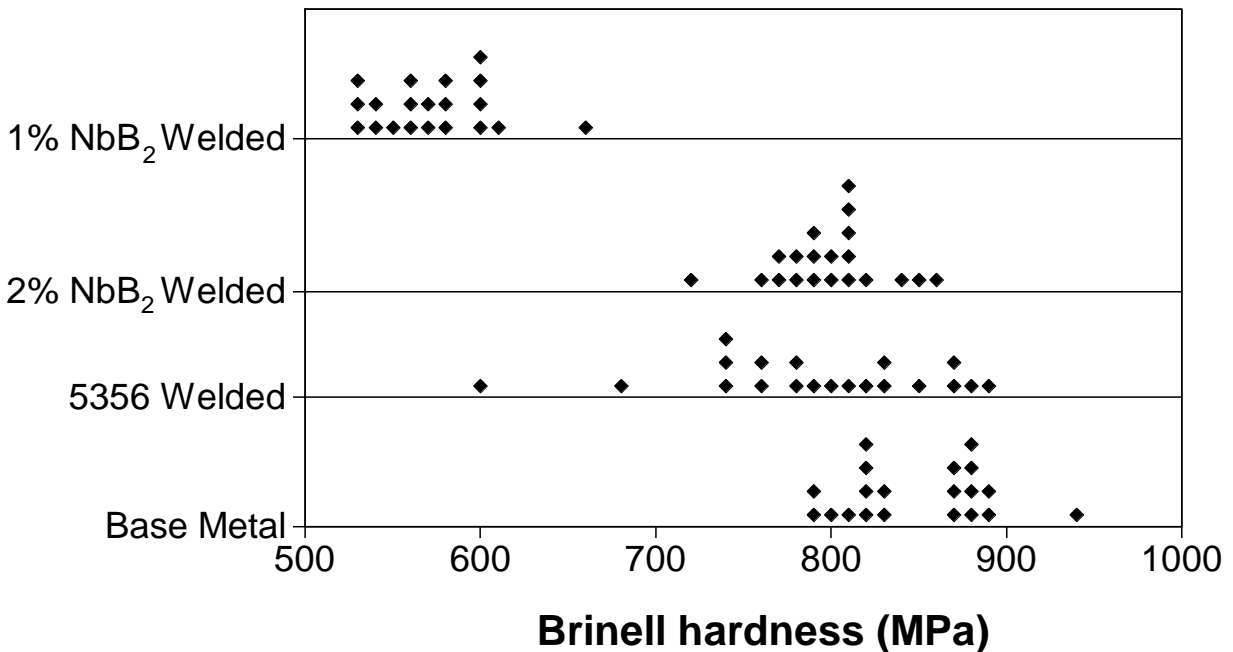


Figure 5.14 Dot plot of the hardness for experimental filler, 5356 filler and 6061 base material.

Table 5.6 Descriptive statistics of Brinell hardness on the fillers and th base alloy

Variable	Total Count	Mean	SE Mean	StDev	Variance	Min	Median	Max
1% NbB ₂ Welded	20	572.7	7.4	33.1	1096.1	526.0	570.9	663.0
2% NbB ₂ Welded	20	798.3	7.4	33.2	1098.8	715.5	800.8	863.5
5356 Welded	20	792.3	16.2	72.3	5226.4	599.3	796.6	892.0
6061 Base Metal	20	848.8	9.1	40.6	1650.1	785.3	847.4	937.6

Another very useful way to represent the difference in hardness is by means of the box diagram in Figure 5.15. Clearly, this graph reveals that the fillers containing NbB₂ display a lower hardness dispersion than the commercial one, producing a more predictable material. These results also reflect a better distribution of the reinforcement in the weld, assuming that the prior stir casting process was successful. In addition, the response surface methodology helped us find the optimal parameters to manufacture a better-quality filler. The hardness dispersion in both types of filler is best observed when studying the individual value plots related to the 2% NbB₂ filler and the 5356 commercial one in Figure 5.16. There is a manifest larger dispersion of hardness values in the commercial material.

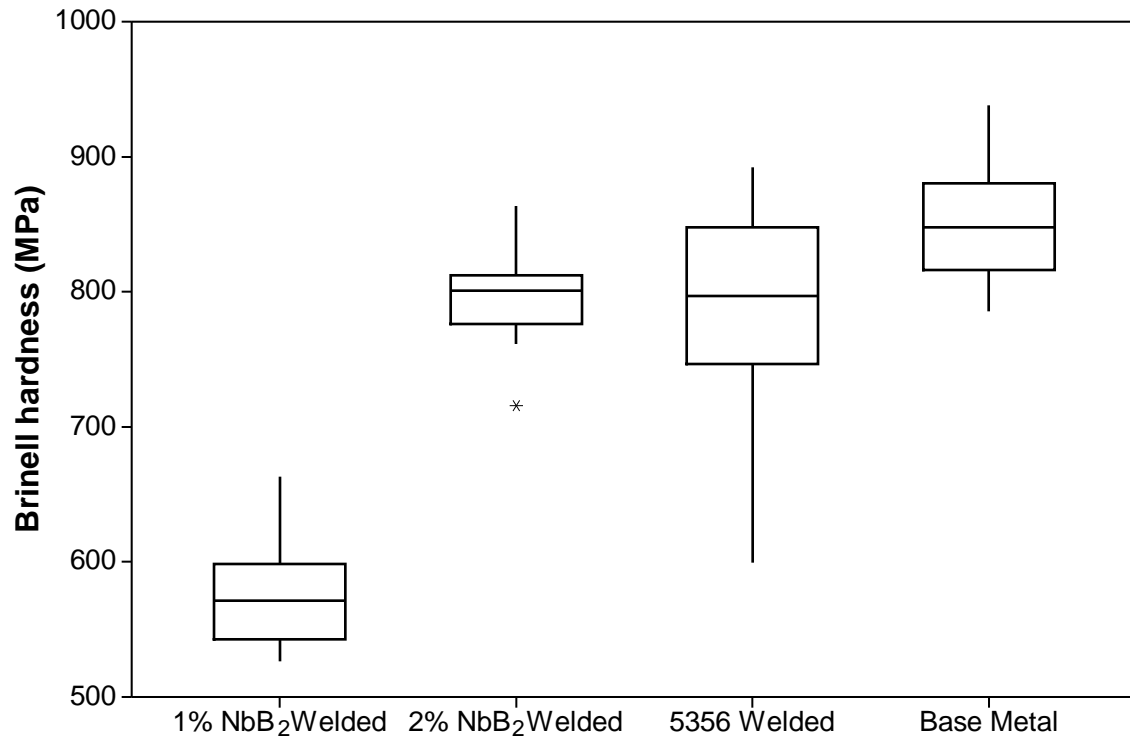


Figure 5.15 Boxplot of the Brinell values for NbB₂ filler, 5356 filler, and 6061 base material.

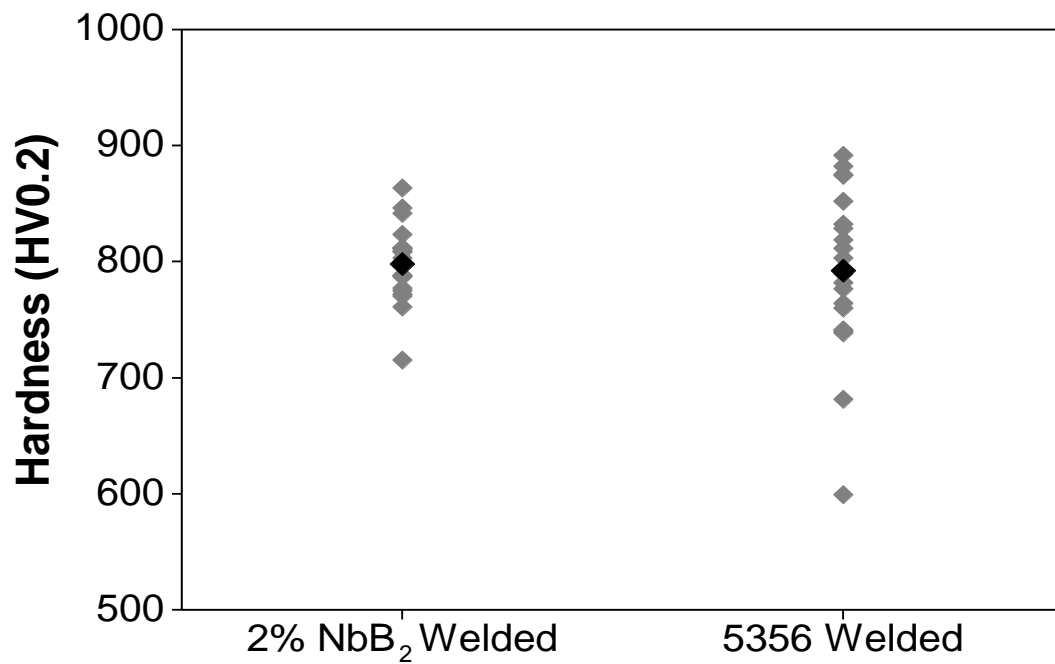


Figure 5.16 Individual value plot measured on the 2% NbB₂ filler and 5356 filler

The Bonett's and Levene's tests permitted to evaluate the variances in both fillers, i.e. the experimental and the commercial one. The use of the median makes the test more robust for smaller samples [38]. This test is an appealing alternative when the residuals do not follow a normal distribution. We examined whether the variances of the two treatments were similar, using a 0.05 significance level. Figure 5.17 presents the confidence intervals for the ratio of variances and p-values for both tests. These tests consider the distances of the observations from the sample median. The p-value of the Bonett's test is 0.031, whereas for the Levene's test it is 0.011. This rejects the null hypothesis that treatments have equal variances.

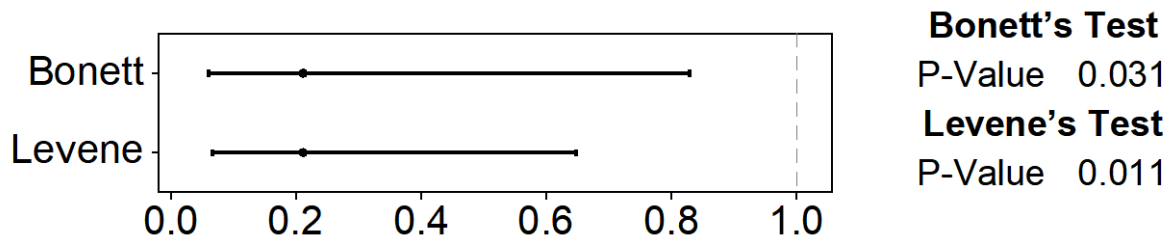


Figure 5.17 Test for two variances: 2% NbB₂ Weld, 5356 Weld, Ratio = 1 vs Ratio ≠ 1.

The Mann-Whitney test checks the equality of medians between the experimental filler and commercial filler with an $\alpha = 0.05$ without assuming a parametric model for distributions. Table 5.7 shows the Mann-Whitney Test and CI: 2% NbB₂ Weld and 5356 Weld; the sample medians of the ordered data is 800.8 for the experimental filler and 796.6 for the commercial filler. The test statistic $W = 412$ has a p-value of 0.9676. The p-value is greater than 0.05 so, one cannot reject the null hypothesis that the medians of the two fillers are equal.

Table 5.7 Mann-Whitney Test and CI: 2% NbB ₂ Welded, 5356 Welded		
	Results	Units
2% NbB₂ Welded Median	800.8	(MPa)
5356 Welded Median	796.6	(MPa)
Point estimate for $\eta_1 - \eta_2$	0.15	
95.0 Percent CI for $\eta_1 - \eta_2$	(-33.19,34.47)	
W	412	
Test of $\eta_1 = \eta_2$ vs $\eta_1 \neq \eta_2$	0.9676	p-Value

Comparison of heat-affected zones

Previously, we highlighted the good performance of the filler containing 2% NbB₂ nanoparticles compared to the 5356 one. Subsequently, the microhardness of the welded piece was examined in order to study the mechanical response of the weld and the HAZ. Figure 5.18 shows boxplots of the average microhardness values on the upper line of the weld, resulting from fifteen indentations measured from the center line of the weld towards the base material (BM), welded with the experimental filler. The welded zone has lower hardness dispersion than the HAZ and BM. The HAZ hardness change can be attributed to the multipass welding (melting and solidification) of the filler metal, which affects the BM microstructure [48]. Figure 5.19 shows boxplots of the average microhardness on the lower line of the weld with the experimental filler. This graph demonstrates how at a depth of 2 mm, the hardness in the weld and in the HAZ remains uniform. Also, small changes in the HAZ hardness are apparent, while the BM has the highest hardness.

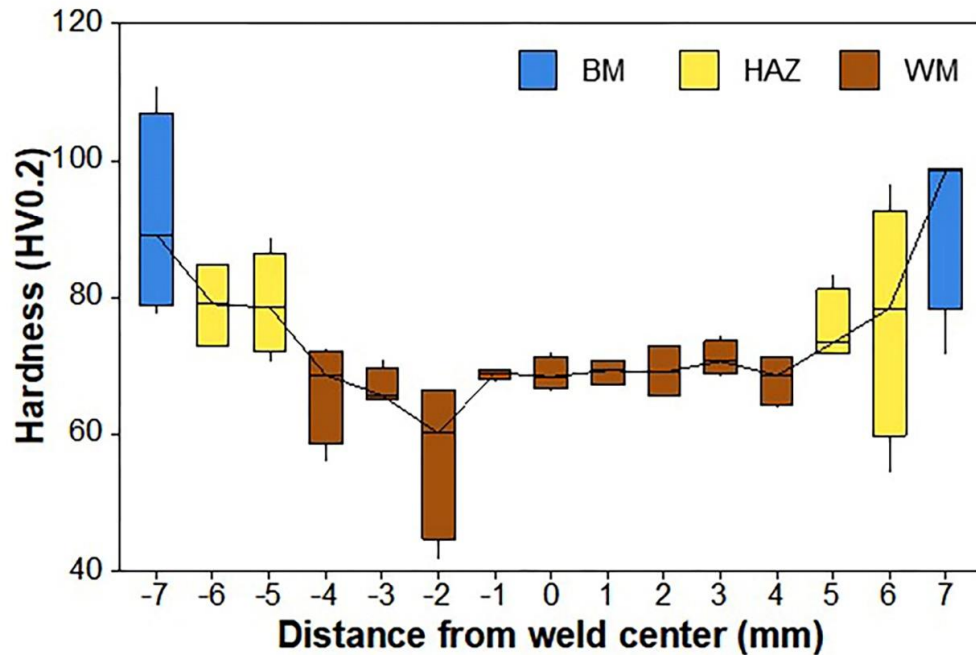


Figure 5.18 Boxplots of average HV0.2 hardness on the upper line of the weld with the experimental filler. Base metal (BM), heat affected zone (HAZ) and weld metal (WM).

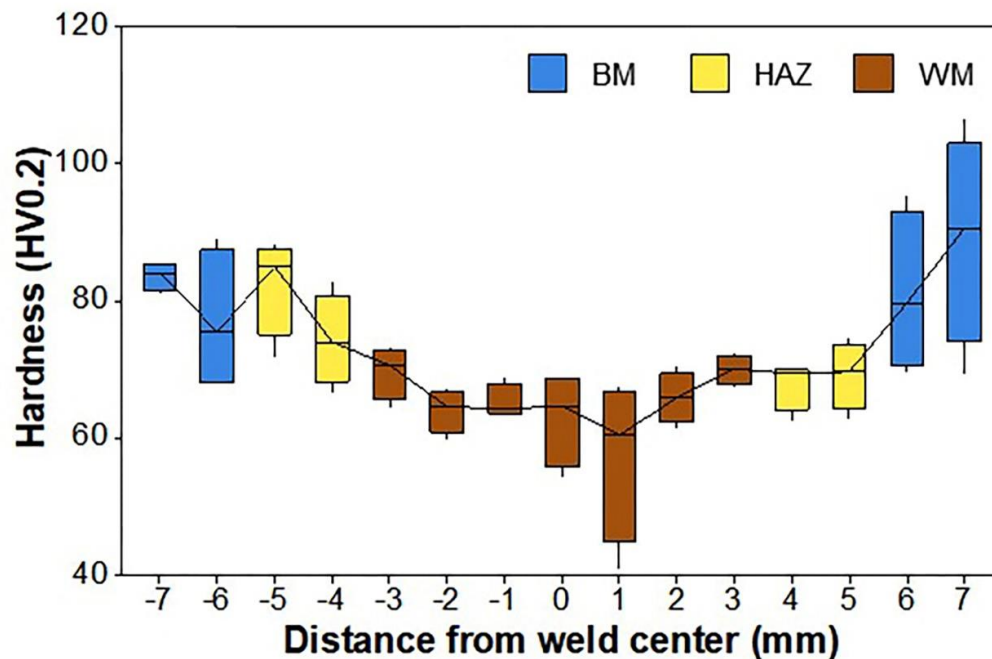


Figure 5. 19 Boxplots of average HV0.2 hardness on the lower line of the weld with the experimental filler. Base metal (BM), heat affected zone (HAZ) and weld metal (WM).

In aluminum alloys with similar chemical compositions (as in many metallic systems), there is a strong correlation between hardness and tensile strength [z3]. Respectively, study the effect of heat input in the welding process by means of microhardness provides us with valuable information of the HAZ strength [51]. Figure 5.20 shows boxplots of the average microhardness values on the upper line of the weld with 5356. This graph proves the lack of homogeneity of the microhardness profile in the weld and the HAZ. Moreover, one can appreciate hardness from 40 MPa to 80 MPa in the commercial material.

On the other hand, better results were obtained in the welded zone with the experimental filler, where more consistent hardness values fell between 63 MPa and 83 MPa. However, in both fillers the melting zone have lower hardness than that of the base metal. This phenomenon is attributed to the loss of magnesium by evaporation upon welding of the filler as a consequence of the high temperature created by the plasma arc [27]. Figure 5.21 shows similar results. At this depth, as one moves away from the centerline of the weld, the microhardness increases. This is due to the presence of finer grains attained by the short solidification time [51].

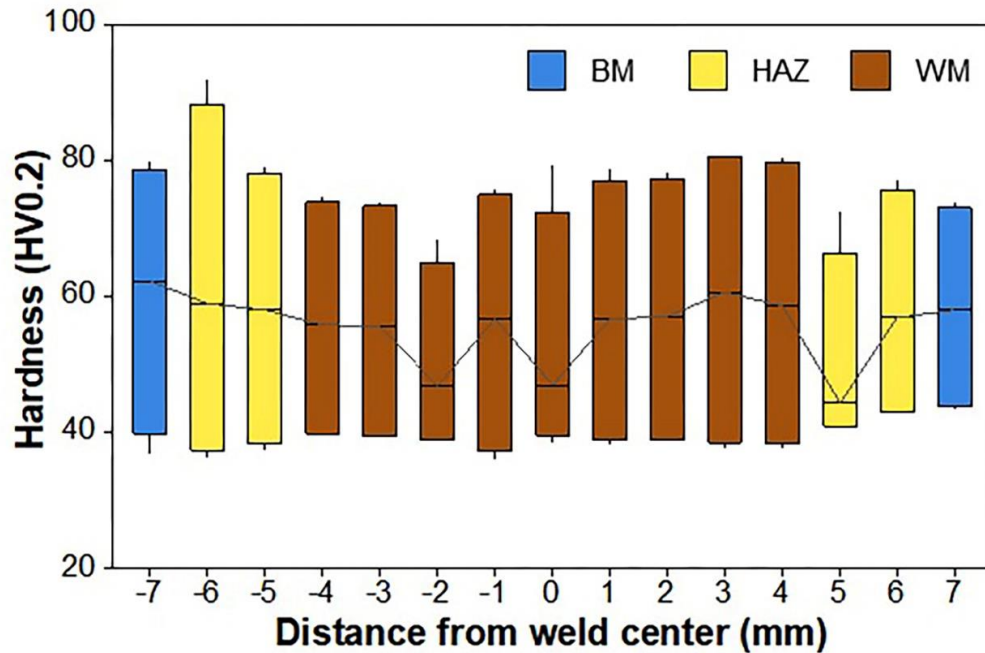


Figure 5.20 Boxplots of average HV0.2 hardness on the top line of the 5356 filler, Base Metal (BM), Heat Affected Zone (HAZ) and Weld Metal (WM).

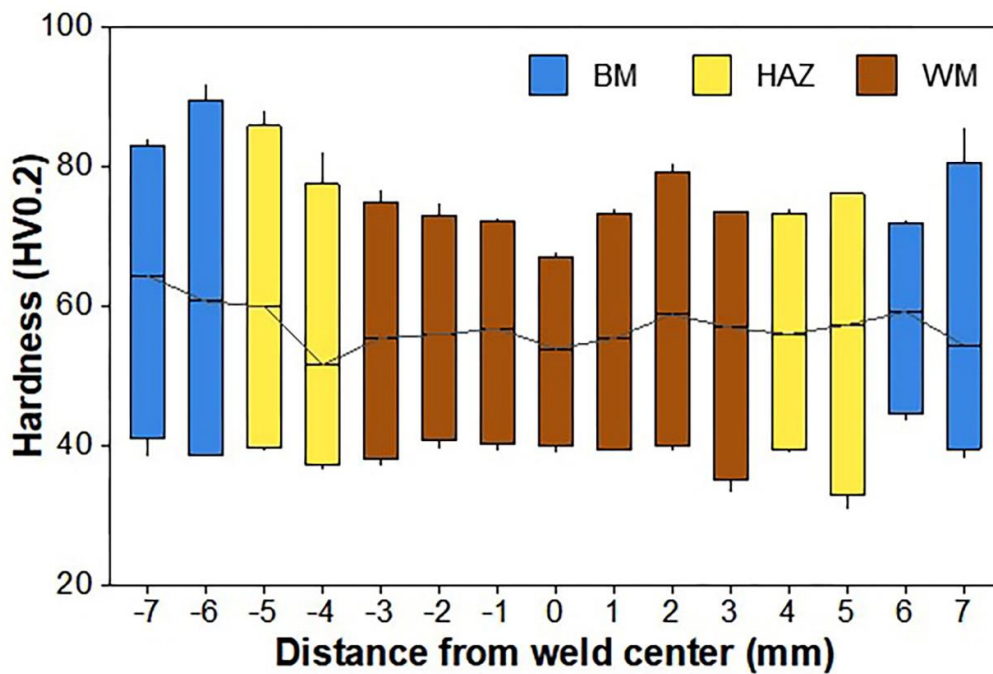


Figure 5.21 Boxplots of average HV0.2 hardness on the bottom line of the 5356 filler, Base Metal (BM), Heat Affected Zone (HAZ) and Weld Metal (WM).

5.2.3 Some prospective applications and markets

The new filler can help fulfill a critical need to shorten the time-to-usage for infrastructure deployment in geographically inaccessible combat zones. One important operational benefit is that no new TIG welding methods need to be developed, as the fillers are designed to be interchangeable with competing commercial ones. Thus, this welding material can raise the standards of quality tools and infrastructure.

In 2013, the welded products market was valued at \$17.47 billion. According to a report by Transparency Market Research, the said market is expected to reach \$23.78 billion in 2020. As the defense industry will accompany that growth, one could expect a steep demand of welded aluminum products and structures. Within that enriching context and to satisfy such a demand, our new welding filler increases weld quality, while lowering the process cost, without modifying current TIG technology. Further, the proposed product will expand the product life cycle while heightening the weld strength. Thus, potential customers include the defense, as well as the transportation and aerospace industries.

There are a number of potential industrial partners, such as Hobart Brothers Company, which is one of the biggest companies manufacturing consumables for the welding industry. Additionally, for potential use in lightweight construction, the US Army Corps of Engineers, Engineering Research & Development Center could become a resourceful partner in this endeavor.

5.2.4 Conclusions

This chapter discussed different characterization stages related to the experimental and commercial fillers.

- ♦ The tests of Bonett and Levene to evaluate the variances in both fillers revealed that the treatments did not yield equal variances.
- ♦ In the welds, we obtained a mean hardness of 798.3 MPa in the filler with 2% NbB₂, i.e. higher than in the commercial one with 792.3 MPa. However, this difference was not found significant by the Mann-Whitney test verified the equality of the medians between the experimental filler and the commercial filler; the p-value, i.e. 0.9676, demonstrates that the medians of the two fillings might be equal.
- ♦ In addition, the experimental filler hardness had a smaller standard deviation (33.2 MPa) than the commercial one (16.2 MPa), i.e. twice as much. This is indicative of a better welding performance that leads to consistent hardness on the weld surface.
- ♦ Bonett's and Levene's tests showed that there is a statistically significant difference in variances between the responses of the two fillers.
- ♦ During the microhardness studies of the transverse area of the weld, a lower hardness dispersion results were obtained in the welding zone and in the heat affected zone when the NbB₂ nanoparticle filler was used. This filler yields a more uniform welding than the commercial material.
- ♦ Similarly, the heat-affected zone was less affected by the heat evolution, while hardness properties were maintained closer to the base material.

VI. CHAPTER

6. General Conclusions and Recommendations

The present thesis explored first the parameters and factors that affect the manufacturing of NbB₂ nanoparticle-reinforced aluminum welding filler. As a result, in a preliminary stage, we concluded that:

- ♦ The NbB₂ filler presented such lack of uniformity in the weld. In addition, the weld had very low UTS and hardness compared to the material base and the AA 5356 filler.
- ♦ The resulting weld porosity was too high for the quality requirements and directly affected the weld strength.
- ♦ To overcome these problems, we utilized an agglomeration breakdown process to improve the uniform dispersion of the NbB₂ nanoparticles contained in the composite pellets and set up a stir casting technique to manufacture the filler bearing the said nanoparticles.
- ♦ Stir casting allowed for a better distribution of the NbB₂ nanoparticles in the filler, as reflected by the uniform hardness results of the welded workpieces.

In the second stage of this research, the methodology for the design experiment enabled the optimization of the manufacturing process. After a thorough analysis of the results, one could conclude the following:

- ♦ A full factorial experiment allowed assessing the effect of stir casting factors, namely melt stirrer speed and stirring time. We discovered that the *stirring speed * stirring time* interaction was the most significant, whereas the mixing time was the main factor.

- ♦ The response surface analysis displayed concentric ellipses in a Minimax system. For this system, the saddle point was calculated at 12.2 s of stirring time and a stirring speed of 710 RPM, which rendered a 101.2 MPa strength level.
- ♦ A central composite design estimated a second-degree polynomial model that described the conditions for a better quality and wettability between the NbB₂ and the aluminum matrix to achieve a homogeneous filler.
- ♦ The optimal levels to achieve best welding with our novel filler are 2% of NbB₂, at 750 RPM of stirring speed and a stirring time of 35.292 seconds, which would yield a Brinell hardness of 687.413 MPa, and a 3.9% porosity.

A comparative analysis of *NbB₂-Treated Filler to Commercial 5356 Filler* was the final part of this research and led us to conclude that:

- ♦ The hardness of the HAZ joint was the same as that of the weld metal and base material. However, the hardness of the weld zone, in average, was lower than the weld reinforced with NbB₂. One can also conclude that the NbB₂ particles were beneficial for the hardness of the HAZ.
- ♦ The thermomechanical analysis showed that the quality of the filler reinforced with nanoparticles is comparable to the commercial one.

Finally, Appendix D summarizes the properties studied in the research of the experimental filler and commercial 5356 filler. The use of an experimental design helped optimize the manufacturing process and improved the quality of the weld when nanoparticles are added. This helped improve the mechanical properties of the weld too.

Therefore, users are presented with a new alternative to develop innovative welding technology.

6.1 Future Work

Part of the future work is to study new weld mechanical properties to increase the amount of reinforcement in the Al-Mg-NbB₂ filler. The effect of other alloying elements, such as manganese, copper and silicon [ASM 6A] should be included in future experimentations. This could expand the range of application of these novel fillers in structural purposes. During the manufacturing process we should have other factors and considerations, such as the use of a protective atmosphere in the melting process in order to reduce casting defects and porosity, solidification process in the casting and cooling rates. In addition, there is an opportunity experimental variability analysis within the optimization process.

Further, an important aspect in the construction industry is the inherent costs associated with their projects. A cost analysis of the experimental filler per kilogram would be the next step to evaluate the feasibility of using the filler in different types of projects.

VII. CHAPTER

7. Reference

- [1] M. Nagaral, V. Auradi, and M. K. Ravishankar, "MECHANICAL BEHAVIOUR OF ALUMINIUM 6061 ALLOY REINFORCED WITH Al_2O_3 & GRAPHITE PARTICULATE HYBRID METAL MATRIX COMPOSITES," vol. 1, no. 2, pp. 193–198, 2013.
- [2] H. Lin, L. Ying, L. Jun, and L. Binghong, "Microstructure and Mechanical Properties for TIG Welding Joint of High Boron Fe-Ti-B Alloy," *Rare Met. Mater. Eng.*, vol. 43, no. 2, pp. 283–286, 2014.
- [3] J. J. Wang, T. Lin, and S. B. Chen, "Obtaining weld pool vision information during aluminium alloy TIG welding," *Int. J. Adv. Manuf. Technol.*, vol. 26, no. 3, pp. 219–227, 2005.
- [4] W. Xi-he, N. Ji-tai, G. Shao-kang, W. Le-jun, and C. Dong-feng, "Investigation on TIG welding of SiCp-reinforced aluminum-matrix composite using mixed shielding gas and Al-Si filler," *Mater. Sci. Eng. A*, vol. 499, no. 1–2, pp. 106–110, 2009.
- [5] B. Ashok Kumar and N. Murugan, "Metallurgical and mechanical characterization of stir cast AA6061-T6-AlNp composite," *Mater. Des.*, vol. 40, pp. 52–58, 2012.
- [6] Y. Zhao, L. Zhou, Q. Wang, K. Yan, and J. Zou, "Defects and tensile properties of 6013 aluminum alloy T-joints by friction stir welding," *Mater. Des.*, vol. 57, pp. 146–155, 2014.
- [7] Y. Cho, W. Li, and S. J. Hu, "Design of experiment analysis and weld lobe estimation for aluminum resistance spot welding," *Weld. J.*, vol. 85, no. 3, p. 45s–51s, 2006.

- [8] a. Kumar and S. Sundarrajan, "Optimization of pulsed TIG welding process parameters on mechanical properties of AA 5456 Aluminum alloy weldments," *Mater. Des.*, vol. 30, no. 4, pp. 1288–1297, 2009.
- [9] D. Florián-Algarín, A. Padilla, N. N. López, and O. M. Suárez, "Fabrication of aluminum wires treated with nanocomposite pellets," *Sci. Eng. Compos. Mater.*, 2014.
- [10] J. Wang, D. Yi, X. Su, F. Yin, and H. Li, "Properties of submicron AlN particulate reinforced aluminum matrix composite," *Mater. Des.*, vol. 30, no. 1, pp. 78–81, 2009.
- [11] J. Hashim, L. Looney, and M. S. J. Hashmi, "Particle distribution in cast metal matrix composites—Part II," *J. Mater. Process. Technol.*, vol. 123, no. 2, pp. 258–263, 2002.
- [12] W. Speer and O. S. Es-Said, "Applications of an aluminum-beryllium composite for structural aerospace components," *Eng. Fail. Anal.*, vol. 11, no. 6, pp. 895–902, 2004.
- [13] M. Fattahi, a. R. Gholami, a. Eynalvandpour, E. Ahmadi, Y. Fattahi, and S. Akhavan, "Improved microstructure and mechanical properties in gas tungsten arc welded aluminum joints by using graphene nanosheets/aluminum composite filler wires," *Micron*, vol. 64, pp. 20–27, 2014.
- [14] M. Fattahi, N. Nabhani, E. Rashidkhani, Y. Fattahi, S. Akhavan, and N. Arabian, "A new technique for the strengthening of aluminum tungsten inert gas weld metals: Using carbon nanotube/aluminum composite as a filler metal," *Micron*, vol. 54–55, pp. 28–35, 2013.

- [15] N. K. Babu, M. K. Talari, D. Pan, and J. Wei, "High-temperature mechanical properties investigation of Al-6.5 % Cu gas tungsten arc welds made with scandium modified 2319 filler," *Int. J. Adv. Manuf. Technol.*, vol. 65, no. 9–12, pp. 1757–1767, 2013.
- [16] J. a. Al-Jarrah, S. Swalha, T. A. Mansour, M. Ibrahim, M. Al-Rashdan, and D. a. Al-Qahsi, "Welding equality and mechanical properties of aluminum alloys joints prepared by friction stir welding," *Mater. Des.*, vol. 56, pp. 929–936, 2014.
- [17] D. S. Nagesh and G. L. Datta, "Genetic algorithm for optimization of welding variables for height to width ratio and application of ANN for prediction of bead geometry for TIG welding process," *Appl. Soft Comput. J.*, vol. 10, no. 3, pp. 897–907, 2010.
- [18] P. Kumar, "Process Parameters Optimization of an Aluminium Alloy with Pulsed Gas Tungsten Arc Welding (GTAW) Using Gas Mixtures," *Mater. Sci. Appl.*, vol. 2, no. 4, pp. 251–257, 2011.
- [19] K. Kalaiselvan, N. Murugan, and S. Parameswaran, "Production and characterization of AA6061-B4C stir cast composite," *Mater. Des.*, vol. 32, no. 7, pp. 4004–4009, 2011.
- [20] M. Science-poland, "Influence of cenospheres of fly ash on the mechanical properties and wear of permanent moulded eutectic Al – Si alloys," vol. 28, no. 1, 2010.
- [21] a. Mazahery, H. Abdizadeh, and H. R. Baharvandi, "Development of high-performance A356/nano-Al₂O₃ composites," *Mater. Sci. Eng. A*, vol. 518, no. 1–2, pp. 61–64, 2009.

- [22] S. Tahamtan, a. Halvae, M. Emamy, and M. S. Zabihi, "Fabrication of Al/A206-Al₂O₃ nano/micro composite by combining ball milling and stir casting technology," *Mater. Des.*, vol. 49, pp. 347–359, 2013.
- [23] D. R. S. J and R. S. D. S. D. I, "Synthesis and characterization of Al6061-Fly Ash p-SiC p composites by stir casting and compocasting methods," *Energy Procedia*, vol. 34, pp. 637–646, 2013.
- [24] S. Amirkhanlou and B. Niroumand, "Synthesis and characterization of 356-SiCp composites by stir casting and compocasting methods," *Trans. Nonferrous Met. Soc. China (English Ed.)*, vol. 20, no. SUPPL. 3, pp. s788–s793, 2010.
- [25] S. Sankaranarayanan, S. Jayalakshmi, and M. Gupta, "Hybridizing micro-Ti with nano-B₄C particulates to improve the microstructural and mechanical characteristics of Mg–Ti composite," *J. Magnes. Alloy.*, vol. 2, no. 1, pp. 13–19, 2014.
- [26] D. P. B., *ASM Handbook Volume 6: Welding, Brazing, and Soldering*, vol. 6. ASM International, 1993.
- [27] V. L. Lienert, Thomas J.; Babu, Sudarsanam Suresh; Siewert, Thomas A.; Acoff, *ASM Handbook, Volume 06A - Welding Fundamentals and Processes*, vol. 06A. ASM International, 2011.
- [28] M. Balasubramanian, *Composite Materials and Processing*, Illustrate. Taylor & Francis, 2013.
- [29] K. U. Kainer, *Metal Matrix Composites: Custom-made Materials for Automotive and Aerospace Engineering*. John Wiley & Sons, 2006.
- [30] P. V. B. Pulickel M. Ajayan, Linda S. Schadler, *Nanocomposite Science and*

Technology. John Wiley & Sons, 2006.

- [31] C. Suryanarayana, *Mechanical Alloying and Milling*. Marcel Dekker., 2004.
- [32] A. I. H. Committee, *ASM Handbook: Casting. Volume 15*, 10th ed., vol. 15. ASM International, 2008.
- [33] A. I. H. C. Nikki D. DiMatteo, *Fatigue and Fracture Volume 19 of ASM handbook*, Illustrate. ASM International, 1996.
- [34] C. L. De Castro and B. S. Mitchell, "Nanoparticles from Mechanical Attrition," pp. 1–15, 2002.
- [35] W. C. Guaglianoni, A. Energia, and E. S. U. A. Caracterização, "SYNTHESIS OF WC-12wt % Co NANOCOMPOSITES BY HIGH ENERGY BALL MILLING AND THEIR," pp. 211–215, 2015.
- [36] S. R. S. Bernard Dennis Cullity, *Elements of X-ray diffraction, 3rd edition*, 3, illustrated. Prentice Hall, 2001.
- [37] L. R.-R. O. Marcelo Suárez, José Vazquez, "Synthesis and Characterization of Mechanically Alloyed Al/Al_xMg_{1-x}B₂ Composites," *Sci. Eng. Compos. Mater.*, vol. 16, no. 4, 2009.
- [38] D. C. Montgomery, *Design and Analysis of Experiments*, 8th Editio. John Wiley & Sons, Incorporated, 2012.
- [39] C. Suryanarayana, *Mechanical alloying and milling suryanaraya*, vol. 46. 2001.
- [40] M. Raei, M. Panjepour, and M. Meratian, "Effect of stirring speed and time on microstructure and mechanical properties of Cast Al–Ti–Zr–B₄C composite produced by stir casting," *Russ. J. Non-Ferrous Met.*, vol. 57, no. 4, pp. 347–360, 2016.

- [41] Y. Li, Q. Li, W. Liu, and G. Shu, "Effect of Ti content and stirring time on microstructure and mechanical behavior of Al-B₄C composites," *J. Alloys Compd.*, vol. 684, pp. 496–503, 2016.
- [42] S. B. Prabu, L. Karunamoorthy, S. Kathiresan, and B. Mohan, "Influence of stirring speed and stirring time on distribution of particles in cast metal matrix composite," *J. Mater. Process. Technol.*, vol. 171, no. 2, pp. 268–273, 2006.
- [43] C. M. A.-C. Raymond H. Myers, Douglas C. Montgomery, *Response Surface Methodology: Process and Product Optimization Using Designed Experiments*, 3rd ed., no. 1. John Wiley & Sons, 2011, 2011.
- [44] J. J. MOSES, I. DINAHARAN, and S. J. SEKHAR, "Prediction of influence of process parameters on tensile strength of AA6061/TiC aluminum matrix composites produced using stir casting," *Trans. Nonferrous Met. Soc. China (English Ed.)*, vol. 26, no. 6, pp. 1498–1511, 2016.
- [45] U. K. Annigeri and G. B. Veeresh Kumar, "Method of stir casting of Aluminum metal matrix Composites: A review," *Mater. Today Proc.*, vol. 4, no. 2, pp. 1140–1146, 2017.
- [46] R. V. Muralidhar, R. R. Chirumamila, R. Marchant, and P. Nigam, "A response surface approach for the comparison of lipase production by *Candida cylindracea* using two different carbon sources," *Biochem. Eng. J.*, vol. 9, no. 1, pp. 17–23, 2001.
- [47] R. Singh, S. Chauhan, and P. C. Gope, "ScienceDirect Influence of notch radius and strain rate on the mechanical properties and fracture behavior of TIG-welded 6061 aluminum alloy," *Arch. Civ. Mech. Eng.*, vol. 16, no. 3, pp. 513–523, 2016.

- [48] S. Kannan, S. S. Kumaran, and L. A. Kumaraswamidhas, "An investigation on compression strength analysis of commercial aluminium tube to aluminium 2025 tube plate by using TIG welding process," *J. Alloys Compd.*, 2016.
- [49] O. E. C. Ñ, "Estimation of welded joint strength using genetic algorithm approach," vol. 47, pp. 1249–1261, 2005.
- [50] T. Analysis, "Thermomechanical Analysis (TMA) Principles of TMA," pp. 172–182.
- [51] P. Kumar, K. P. Kolhe, S. H. Mankar, and S. Kumar, "Prediction of Heat Affected Zone and Effect of Heat Input in GTA Welded Al Alloy 6061," *Int. J. Eng. Sci. Innov. Technol.*, vol. 4, no. 6, pp. 130–137, 2015.

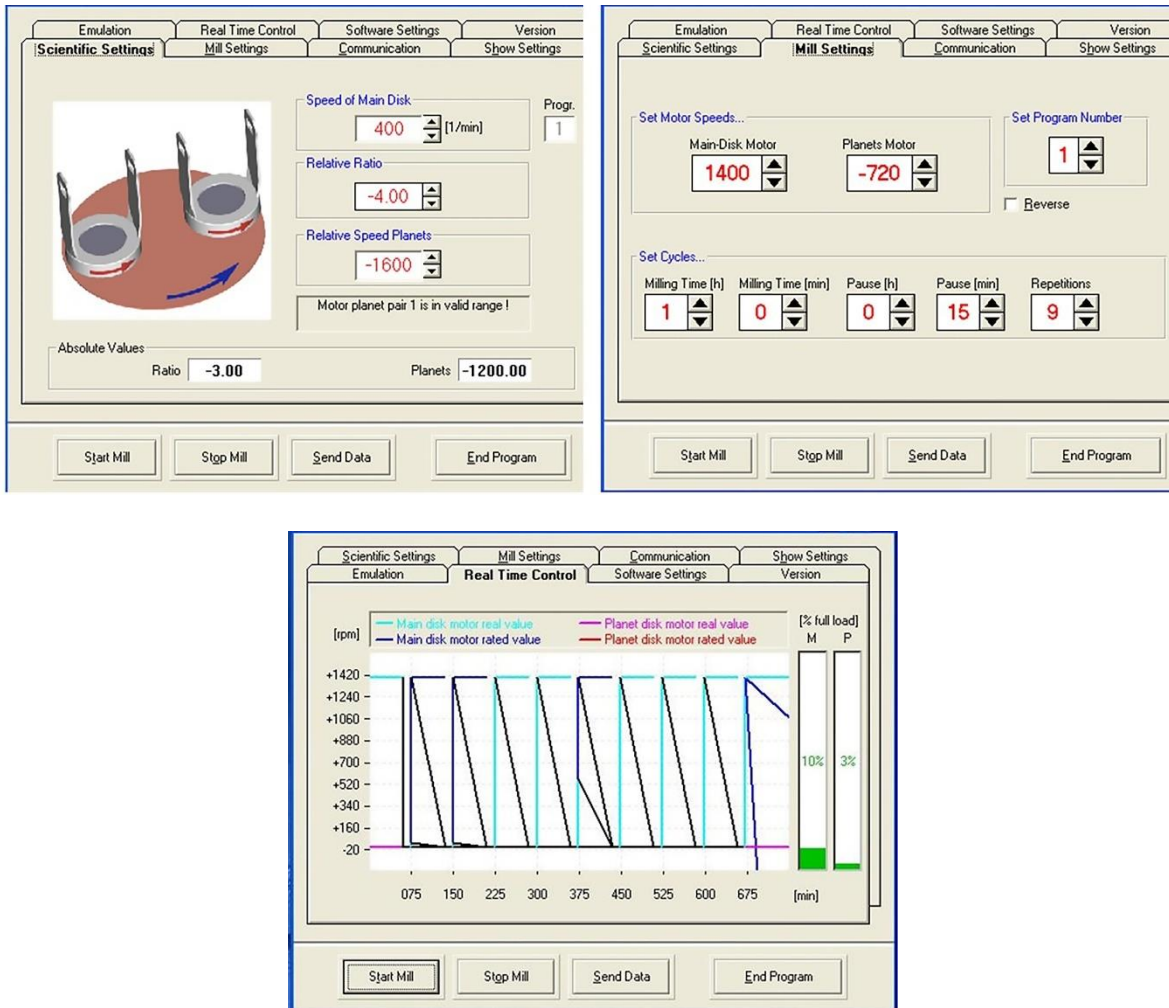
VIII. CHAPTER

8. Appendices

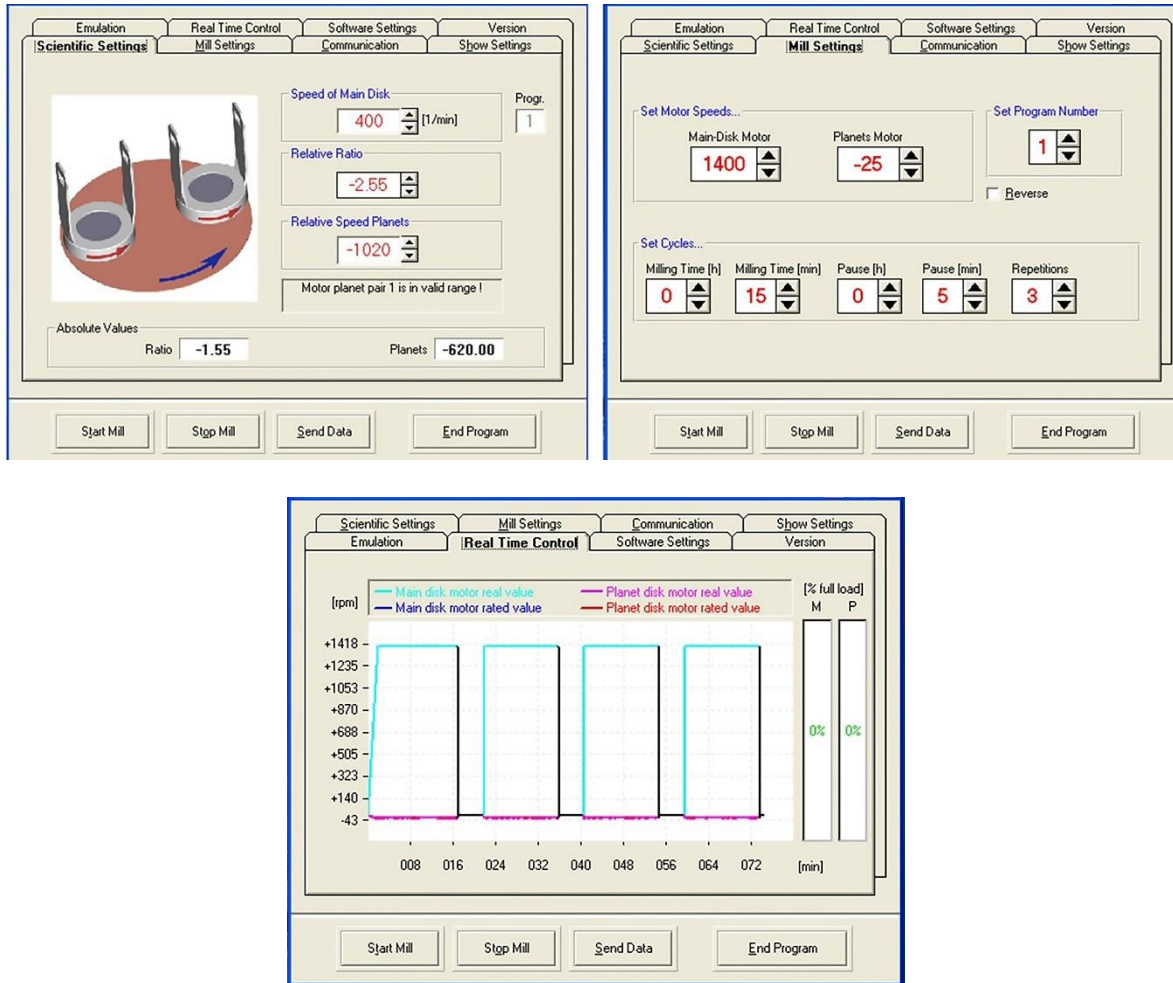
8.1 Appendix A

A.1 The grinding settings and result for 10hr, 1600 RPM

Vario-Planetary Ball Milling Pulverisette 4 Fritsch™ Software settings



A.2 The cold welding settings and result for 1hr, 1020 RPM



8.2 Appendix B

B.1 Full factorial design matrix

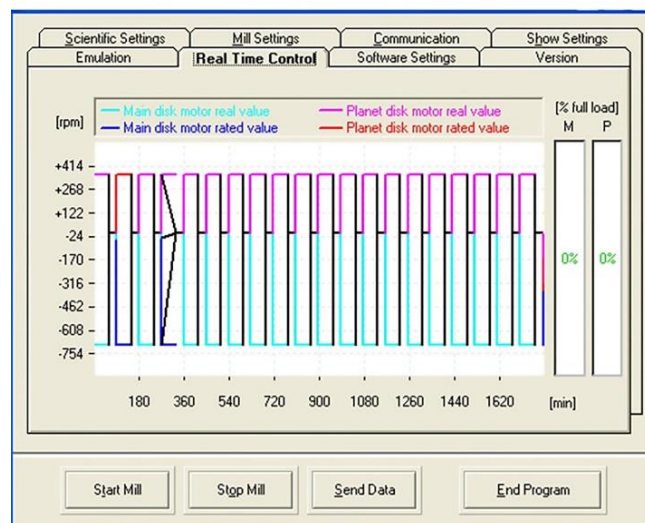
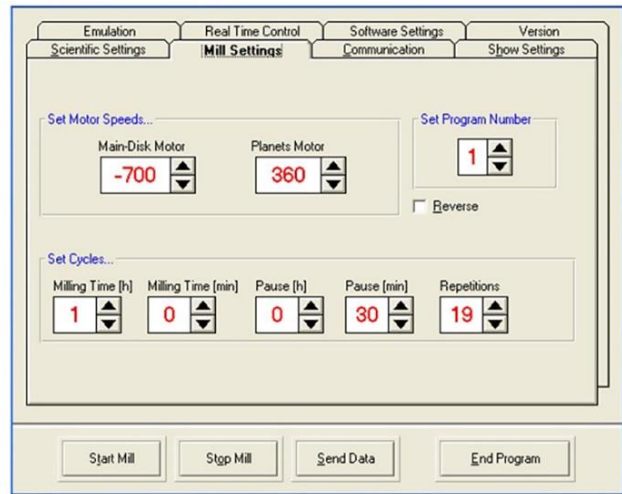
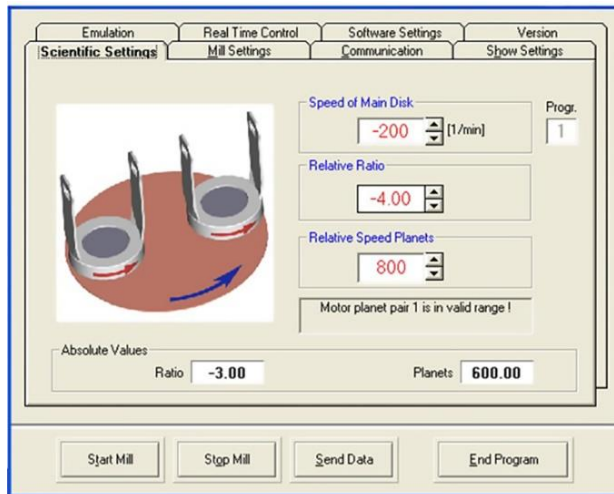
StdOrder	RunOrder	CenterPt	Blocks	Stirring Speed	Stirring Time	Label	Ultimate tensile strength (Y)
1	6	1	1	-1	-1	-1	121.0116
2	2	1	1	1	-1	a	126.12669
3	1	1	1	-1	1	b	117.13294
4	7	1	1	1	1	ab	88.023816
5	9	1	1	-1	-1	-1	127.20712
6	5	1	1	1	-1	a	113.36905
7	3	1	1	-1	1	b	105.28087
8	10	1	1	1	1	ab	108.00853
9	4	0	1	0	0		94.240535
10	8	0	1	0	0		91.066412

B.2 Central composite design matrix for Brinell hardness

StdOrder	RunOrder	CenterPt	Blocks	% Niobium diboride	Stirring Speed	Stirring Time	Labels	Brinell hardness				
1	13	1	1	-1	-1	-1	-1	586.7	536.7	573.4	579.4	603.1
2	8	1	1	1	-1	-1	a	582.0	603.5	603.5	585.8	602.2
3	6	1	1	-1	1	-1	b	551.1	553.4	543.3	554.5	563.8
4	17	1	1	1	1	-1	ab	623.3	620.8	624.5	627.5	623.2
5	19	1	1	-1	-1	1	c	545.6	534.6	526.0	524.9	526.0
6	14	1	1	1	-1	1	ac	536.7	532.4	558.0	553.5	560.5
7	11	1	1	-1	1	1	bc	569.7	582.9	557.2	545.6	546.7
8	1	1	1	1	1	1	abc	662.6	651.6	650.3	662.0	659.0
9	18	1	1	-1	-1	-1	-1	512.5	529.1	533.6	536.6	534.6
10	2	1	1	1	-1	-1	a	619.3	627.8	647.3	634.5	641.6
11	5	1	1	-1	1	-1	b	591.6	588.1	607.3	601.9	585.5
12	12	1	1	1	1	-1	ab	619.4	624.5	623.2	629.4	623.3
13	15	1	1	-1	-1	1	c	522.8	531.4	510.9	605.1	569.7
14	7	1	1	1	-1	1	ac	651.6	580.8	582.0	591.9	583.2
15	10	1	1	-1	1	1	bc	572.1	585.4	560.3	547.8	568.6
16	20	1	1	1	1	1	abc	572.3	575.9	579.5	590.7	575.9
17	9	0	1	0	0	0		535.7	529.1	543.3	534.6	547.7
18	3	0	1	0	0	0		596.8	584.2	607.1	588.0	574.4
19	4	0	1	0	0	0		544.3	563.3	568.4	565.0	568.6
20	16	0	1	0	0	0		632.8	596.7	624.4	639.6	632.7
21	22	-1	2	-2	0	0		490.9	513.5	517.6	500.5	542.2
22	25	-1	2	2	0	0		663.0	636.9	624.4	623.0	626.8
23	21	-1	2	0	-2	0		590.4	605.0	601.0	603.7	605.7
24	23	-1	2	0	2	0		638.5	636.9	636.8	634.1	636.9
25	26	-1	2	0	0	-2		590.0	592.4	592.1	589.1	592.1
26	24	-1	2	0	0	2		507.1	505.8	555.8	513.5	580.6

B.3 The grinding settings and result for 20hr, 1600 RPM

Vario-Planetary Ball Milling Pulverisette 4 Fritsch™ Software settings



B.4 Central composite design matrix for Porosity

StdOrder	RunOrder	CenterPt	Blocks	% Niobium diboride	Stirring Speed	Stirring Time	Labels	Porosity				
1	13	1	1	-1	-1	-1	-1	2.2	2.3	2.1	2.5	2.4
2	8	1	1	1	-1	-1	a	0.7	0.2	0.2	0.3	0.3
3	6	1	1	-1	1	-1	b	1.0	1.0	1.0	1.0	1.0
4	17	1	1	1	1	-1	ab	1.4	1.6	1.5	1.5	1.5
5	19	1	1	-1	-1	1	c	1.2	1.1	1.3	1.4	1.5
6	14	1	1	1	-1	1	ac	0.2	0.6	0.4	0.3	0.2
7	11	1	1	-1	1	1	bc	2.1	2.6	1.4	2.4	1.4
8	1	1	1	1	1	1	abc	1.6	1.5	1.5	1.5	1.3
9	18	1	1	-1	-1	-1	-1	2.3	2.0	2.2	2.2	2.1
10	2	1	1	1	-1	-1	a	0.3	0.2	0.9	0.3	0.1
11	5	1	1	-1	1	-1	b	1.0	1.0	1.1	1.1	1.1
12	12	1	1	1	1	-1	ab	1.8	1.6	1.8	1.1	1.2
13	15	1	1	-1	-1	1	c	1.6	1.6	1.7	1.8	1.9
14	7	1	1	1	-1	1	ac	0.2	0.9	1.2	1.0	0.8
15	10	1	1	-1	1	1	bc	2.0	1.7	1.7	1.5	1.6
16	20	1	1	1	1	1	abc	2.7	1.9	1.8	2.1	1.7
17	9	0	1	0	0	0		1.9	1.7	1.4	1.0	2.0
18	3	0	1	0	0	0		0.4	0.8	0.5	0.1	0.8
19	4	0	1	0	0	0		1.7	1.0	1.1	1.3	1.0
20	16	0	1	0	0	0		0.1	0.2	0.4	0.5	0.9
21	22	-1	2	-2	0	0		2.7	2.2	2.3	2.3	2.3
22	25	-1	2	2	0	0		1.6	1.9	1.1	1.4	1.8
23	21	-1	2	0	-2	0		2.6	2.5	1.1	2.1	1.3
24	23	-1	2	0	2	0		2.6	2.5	2.4	2.2	2.6
25	26	-1	2	0	0	-2		2.6	2.6	2.1	2.3	2.2
26	24	-1	2	0	0	2		2.4	2.7	2.6	2.4	2.8

8.3 Appendix C

C.1 Full factorial design matrix of thermal expansion coefficient

StdOrder	RunOrder	CenterPt	Blocks	Filler Alloys	Temperature	Label	CTE
1	5	1	1	1	-1	-1	23.2
2	12	1	1	-1	-1	a	24.7
3	13	1	1	1	1	b	26.5
4	8	1	1	-1	1	ab	26.7
5	16	1	1	1	-1	-1	21.1
6	7	1	1	-1	-1	a	24.9
7	2	1	1	1	1	b	25.9
8	11	1	1	-1	1	ab	26.5
9	14	1	1	1	-1	-1	26.4
10	3	1	1	-1	-1	a	24.8
11	10	1	1	1	1	b	27.1
12	4	1	1	-1	1	ab	26.3
13	9	1	1	1	-1	-1	25.7
14	15	1	1	-1	-1	a	24.8
15	6	1	1	1	1	b	27.6
16	1	1	1	-1	1	ab	26.9

8.4 Appendix D

Table 5.7 Summary of the properties of the experimental filler and commercial filler 5356.

	CTE	CTE	Brinell hardness	Porosity	HV0.2 hardness		
	150 °C ⁻¹	300 °C ⁻¹	3.175 mm ball, 15 kgf	Area %	WM	HAZ	BM
Al-Mg- NbB₂ 1%	24.7	26.8	572.7 MPa	3.93%	*	*	*
Al-Mg- NbB₂ 2%	*	*	798.3 MPa	2.72%	69.3	80.8	87.7
5356	24.8	26.6	792.3 MPa	2.59%	63.7	79.1	86.3